ABSTRACT

Title of dissertation: CONTROL-ORIENTED REDUCED ORDER MODELING OF DIPTERAN FLAPPING FLIGHT

Imraan Faruque, Doctor of Philosophy, 2011

Dissertation directed by: Professor J Sean Humbert
Department of Aerospace Engineering

Flying insects achieve flight stabilization and control in a manner that requires only small, specialized neural structures to perform the essential components of sensing and feedback, achieving unparalleled levels of robust aerobatic flight on limited computational resources. An engineering mechanism to replicate these control strategies could provide a dramatic increase in the mobility of small scale aerial robotics, but a formal investigation has not yet yielded tools that both quantitatively and intuitively explain flapping wing flight as an "input-output" relationship. This work uses experimental and simulated measurements of insect flight to create reduced order flight dynamics models. The framework presented here creates models that are relevant for the study of control properties. The work begins with automated measurement of insect wing motions in free flight, which are then used to calculate flight forces via an empirically-derived aerodynamics model. When paired with rigid body dynamics and experimentally measured state feedback, both the bare airframe and closed loop systems may be analyzed using frequency domain

system identification. Flight dynamics models describing maneuvering about hover and cruise conditions are presented for example fruit flies (*Drosophila melanogaster*) and blowflies (*Calliphorids*). The results show that biologically measured feedback paths are appropriate for flight stabilization and sexual dimorphism is only a minor factor in flight dynamics. A method of ranking kinematic control inputs to maximize maneuverability is also presented, showing that the volume of reachable configurations in state space can be dramatically increased due to appropriate choice of kinematic inputs.

CONTROL-ORIENTED REDUCED ORDER MODELING OF DIPTERAN FLAPPING FLIGHT

by

Imraan Faruque

Dissertation submitted to the Faculty of the Graduate School of the
University of Maryland, College Park in partial fulfillment
of the requirements for the degree of
Doctor of Philosophy
2011

Advisory Committee:
Professor J Sean Humbert, Chair
Professor Sarah Bergbreiter
Professor Roberto Celi
Professor Inderjit Chopra
Professor Gerald Wilkinson

Acknowledgments

I owe my gratitude to all the people who made these discoveries possible.

I thank my advisor Dr Sean Humbert, for the engaging problems and resources he has provided me, and for his apparently limitless enthusiasm. I'm surprised I ended up studying bugs for this long, and I am sure part of that is due to his curiosity, excitement, and ideas.

I am quite grateful for my committee members' contributions as well. Dr Celi's expertise with system identification and all things rotorcraft was invaluable, even if he refuses to fly on them. Dr Sanner's wealth of control theoretic knowledge allowed him issue an un-matched academic challenge and present incredibly focused questions. I'm thankful for Dr Chopra, who became an aerodynamics reference, and Dr Bergbreiter, who introduced me to a microscopic world of robots, as well as Dr Wilkinson, who introduced me to antlike bugs with eyes on the ends of stalks like aliens.

Many in the AVL contributed to this research, most particularly through Dr Jason Vance's biological expertise, Nick Kostreski's experimental work with insects, and Mac MacFarlane's computational work. I thank the rest of the AVL for their patience with my late work hours, and persistently inquisitive nature, both academic and philosophical.

Several agencies contributed financially, particularly the Army, Office of Naval Research, and Air Force Research Lab. I'm especially thankful to the Army Research Lab for hosting me during a portion of my graduate tenure.

I am thankful for the insects who proved that controlling flight at this scale was possible, and to the God who made them.

Most of all, I'm grateful for my family, who made this possible. For my father, who challenged me to think and who inspired all of my academic pursuits, especially this one. I'm perpetually grateful for your sacrifice and, as ridiculously long as this document is, it's not long enough to express your effect on me. For my mother, who humored and even encouraged my investigative hobby that eventually grew into a full time job. For Ruel, who always believed I was smart enough to do anything. For Anya, who always believed I could work hard enough to achieve anything. And for Orion, who always believed I was brave enough to throw myself into anything.

Table of Contents

List of Tables

List of Figures

Nomenclature

α	Wing angle of attack	rad
α_g	Geometric angle of attack	rad
α_{add}	Angle of attack perturbation	rad
α_{ud}	Wing pitch upstroke/downstroke input	rad
β	Stroke plane angle	rad
γ	Coherence	nondim.
η	Wing pitch angle	rad
θ	Body pitch angle	rad
λ_i	Eigenvalue i	
μ	Advance ratio	nondim.
ξ	Body hovering angle	rad
ρ	Fluid (air) density	$\mathtt{kg/m^3}$
ϕ	Stroke angle	rad
ϕ	Fore/aft wingstroke angle bias	rad
Φ	Stroke amplitude	rad
Ψ	Controllability operator	
$\boldsymbol{\omega}^B$	Body angular velocity	rad/s
A	System dynamics matrix	
AR	Wing aspect ratio	nondim.
b_0, b_1, b_2	Planar wing fit coefficients	
B	Control input matrix	
$\bar{c}$	Geometric mean chord	m
C_L	Wing lift coefficient	nondim.
C_D	Wing drag coefficient	nondim.
$L(t)$	Instantaneous lift force	N
d_x, d_z	Components of $\boldsymbol{r}_{G/t}$ in $\mathcal{S}$ coordinates	m
$D(t)$	Instantaneous drag force	N
f	Flap frequency	Hz
g	Gravitational acceleration	$9.8\ \mathtt{m/s^2}$
$G_{xx}(\omega)$	Autospectral density	
$G_{xy}(\omega)$	Cross-spectral density	
$I_{[\ ]}$	Vehicle moments of inertia	$\mathtt{kg\,m^2}$
k, K	Gain, Gain matrix	
m	Vehicle mass	kg
p, q, r	Body angular rates $\boldsymbol{\omega}^B$ in $\mathcal{S}$ coordinates	rad/s
$\{\hat{p}_x, \hat{p}_y, \hat{p}_z\}$	Stroke plane axes $\mathcal{P}$	
r	Spanwise distance outboard along a wing	m
$\hat{r}_2$	Second moment of wing area squared	nondim.
r_a	Spanwise moment arm of lift force	m
$\boldsymbol{r}_{G/p}$	Vector from center of mass G to point P	m
$\boldsymbol{r}_{G/t}$	Vector from center of mass G to thorax center	m
$\{\hat{r}_x, \hat{r}_y, \hat{r}_z\}$	Right wing axes $\mathcal{R}$	
R	Wing length	m

R^2	Coefficient of determination	
R_{RS}	Rotation matrix from $\mathcal{S}$ to $\mathcal{R}$	
$\{\hat{s}_x, \hat{s}_y, \hat{s}_z\}$	Stability frame axes $\mathcal{S}$	
S	Wing area	$\mathtt{m}^2$
t	Time	$\mathtt{sec}$
T	Flap period $T = 1/f$	$\mathtt{sec}$
$u(t)$	Input vector	
$\hat{u}(t)$	Optimal input vector	
$\mathcal{U}$	Input space	
u, v, w	Body translational rates $\boldsymbol{v}^G$ in $\mathcal{S}$ coordinates	$\mathtt{m/s}$
u_r, v_r, w_r	Body translational rates $\boldsymbol{v}^G$ in $\mathcal{R}$ coordinates	$\mathtt{m/s}$
u_t	Wing tip velocity	$\mathtt{m/s}$
$\boldsymbol{v}$	Total flow velocity incident on wing	$\mathtt{m/s}$
v_x, v_y, v_x	Total flow velocity incident on wing $\boldsymbol{v}$ in $\mathcal{R}$ coordinates	$\mathtt{m/s}$
$\boldsymbol{v}_\phi$	Flow velocity on wing due to flapping	$\mathtt{m/s}$
$\boldsymbol{v}_\omega$	Flow velocity on wing due to body rotation $\boldsymbol{\omega}^B$	$\mathtt{rad/s}$
$\boldsymbol{v}^G$	Body velocity	$\mathtt{m/s}$
$x(t)$	State vector	
x_i	Points in state space, $i = 0, 1...$	
X, Y, Z	Stability frame forces in $\mathcal{S}$ coordinates	$\mathtt{N}$
X_c	Controllability Gramian	
$\mathcal{X}$	Configuration space	

Abbreviations

CFD	Computational Fluid Dynamics
GM	Gain Margin
IBINS	Immersed Boundary Incompressible Navier Stokes
MAV	Micro Air Vehicle
LTI	Linear Time Invariant
PM	Phase Margin

Chapter 1

Introduction

1.1 Motivation and Technical Challenges

Flying insects represent simultaneously the highest standard of performance in aerial mobility and the animals that achieve robust flight control with the smallest neurological structures. The prospect of agile control performance that requires small, specialized, computational structures is very attractive from the perspective of micro air vehicle (MAV) design. An understanding of the dynamic properties that insect flight leverages to achieve aerial mobility on a limited computational budget would provide insight into the flapping wing MAV control problem.

Measurements of insect sensory systems has revealed that insects stabilize flight by sensing composite states measured along highly non orthogonal axes, then fusing those inputs into a control law. The directionality of such measurements, as seen in Fig 1.1, is in opposition to traditional engineering measurement of vehicle states. A popular hypothesis has been that the particular combinations insects measure are more important for flight stabilization than traditional isolated, orthogonal measurements like roll or pitch rate (Taylor and Krapp, 2007). If this is the case, then dynamic models should show that insect sensing is most responsive to motions (or directions) that have the highest feedback requirements. Dynamic models are necessary to determine the feedback requirements along different axes, which

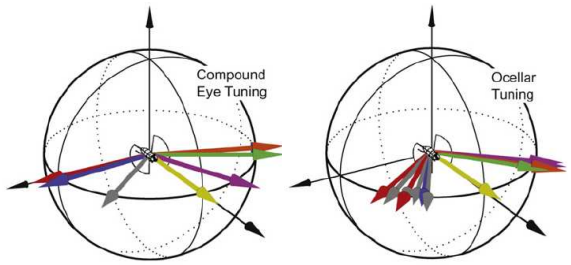

Figure 1.1: Directions in which insect compound eyes and ocelli (rudimentary eyes) are most sensitive (Parsons et al., 2010) may correspond to dynamic properties of the airframe.

would allow researchers to determine if the sensor outputs correspond to characteristic flight modes that require feedback. While full-scale aircraft actuators often excite along orthogonal axes, insects do not necessarily do so and actuation along non-orthogonal axes is equally possible. The insect sensory systems may be tuned not only to the motions requiring stabilization feedback, but also to the effects of its non-orthogonal actuation capabilities, such that the insect's sensors provide it with feedback on the effects of its actuation. An insect with access to measurements describing the directions resulting from its actuation would be exceptionally able to regulate this actuation. Again, testing this hypothesis requires a dynamic model that describes the motion resulting from each actuator, in order to evaluate whether the sensory systems are tuned to the results of non-orthogonal actuation.

A concise dynamic model would allow researchers to evaluate whether insect sensory systems are specifically tuned to dynamic properties such as insect flight modes or actuator results. Despite the need for a concise model, previous investigations have shown that the flight regime is complicated by complex aerodynamic effects, nonlinear wing kinematics and body dynamics, and small perturbations in-

tegrated over many wingstrokes, as well as adaptive sensing and feedback. Detailed modeling and simulation of the aerodynamic effects alone is an involved process that typically requires several weeks for each simulated case. The need for tractable insect flight dynamics modeling leads directly to the problem statement of this dissertation:

> **Problem Statement:** *Find reduced-order dynamics models for small-scale dipteran flapping flight, and determine a path for creating models useful for estimating sensing and feedback requirements. The derived models should be appropriate for control analysis, in particular, answer questions of stability, rates of convergence or instability, modal participation, and feedback requirements, as well as quantify actuation results (eg, maneuverability).*

1.2 Background

In recent years, researchers have made much progress into the task of understanding the aerodynamic basis for and the control architecture involved in insect flight, in particular the fruit fly *Drosophila melanogaster*. Advances in the field of flapping wing aerodynamics have largely relied on the ability of researchers to make detailed observations of the insects' flapping behavior. Early observations of tethered *Drosophila* by Vogel (1967) began to observe variations in certain "stroke parameters" defining wing kinematic patterns and variations in wing contour. Several years later, Weis-Fogh (1972) used Vogel's observations in the development of

the "quasi-steady" form first introduced by Osborne (1951). Briefly, this approach uses curve fits to experimental data to allow the instantaneous lift and drag forces of an insect to be represented by drawing analogy to a similar wing translating at the same angle of attack and the same (steady) velocity. The quasi-steady references found in insect aerodynamics literature are in contrast to the aero-elastic concept, which refers to ignoring unsteady effects by retaining only terms dependent steady quantities and does not employ curve fits to experimental data. Because of this, we consider the aerodynamic modeling presented in insect flight literature an experimental aerodynamics model *presented in quasi-steady form.*

The quasi-steady form has been extensively used as a foundation by researchers beginning with Ellington and Dickinson (Ellington, 1984a) to develop the aerodynamic theory used in contemporary understanding and prediction of insect flight. A major use of the theory is in the prediction of baseline forces in order to elucidate the contributions of additional aerodynamic mechanisms, predominantly unsteady effects (Dickinson and Gotz, 1999). The concept has been applied to determine aerodynamic contributions by mechanisms such as "clap and fling" movements (Spedding and Maxworthy, 1986) and dynamic stall (Dickinson et al., 1999). Even so, the chief contribution of the quasi-steady form to the field of insect flight understanding has been as a means to reduce kinematic and force data taken from both tethered and in-flight recordings of wing kinematics, allowing reduction of in-flight data to nondimensional coefficients that may be interpreted from the perspective of more traditional aerodynamic mechanisms (Fry et al., 2003).

The computational workload an insect must perform to support flapping wing

flight is still an active area of research. Experimental evidence has indicated physiological components involved in flight stabilization, such as tangential cells and descending neurons that translate optic flow estimates to flight motor commands. Despite the measurements made on the sensing and control components, the flight stabilization demands that these structures must support are unknown, but must be addressed via an analysis of the plant they are responsible for controlling (ie, the insect dynamics). Recently, Taylor and Thomas (2003a,b) used measurements of tethered locusts to estimate the stability and control properties associated with dipteran insect flapping flight, while Hesselberg and Lehmann (2007) and Hedrick et al. (2009) addressed the yaw dynamics of flapping flight. Aerodynamics investigations using computational fluid dynamics (CFD) (Sun and Xiong, 2005) have also addressed the longitudinal (motion in the insect's plane of symmetry) flapping flight. A concise understanding of how the control inputs available to a dipteran insect (in the form of kinematic variables) affect the long term motion of the insect (flight control) is expected to provide insight into why insects tend to use particular control inputs more readily than others and indicate how coupled control inputs can lead to particular motions. A large body of knowledge exists to provide control analysis on state-space dynamics models (Ogata, 2002), meaning that a process that simplifies the relatively complex nonlinear dynamics of dipteran flapping wing insect flight is desirable. State-space models and the process to generate them are goals of this study. The simplified linear time invariant dynamics models may then be used to evaluate controllability and design control laws for hovering micro-air-vehicles near hover.

Despite the widespread usage of the experimental aerodynamics model and the information that it can provide regarding insect aerodynamics, the theory is normally applied as a model operating at a single point. Placing the model in the context of perturbations from that operating point provides insight into the fundamental dynamic behavior, which can then be used to understand the sensing and feedback requirements for stable flight. These are precisely the goals of this research.

This research examines the implication of passive aerodynamic stability mechanisms associated with flapping flight. Euler rigid body dynamics are paired with quasi steady aerodynamcs modeling that includes effects of perturbations from the hover equilibrium. Results are based on analysis of the analytical equations as well as frequency-based system identification of the non-linear simulation. The goal is a set of linearized state-space models valid for small motions about hover that may be used to understand sensing and feedback requirements (and directly provide modal insight as in Taylor and Thomas (2003c); Sun and Xiong (2005)). Such models are derived under the fundamental assumption that it is the averaged forces and moments over the wingstroke that are important up to timescales of the rigid body dynamics, an assumption which is examined by direct comparison to a simulator includes the effects of force and moment changes throughout a winstroke. Other key assumptions are the use of rigid (planar) wings that do not deform, rigid insect bodies (fixed abdomen and leg angles). Additionally, aerodynamic effects such as reverse flow and spanwise flow are ignored as a side effect of the experimental aerodynamics model used (the effect of this assumption is examined in Chapter 5).

Results from fruit flies (*Drosophila*) and blowflies (*Calliphoridae*) are presented in this dissertation. Wing kinematics and aerodynamics measurements are available for fruit flies, while sensory system measurements are available for blowflies. From the perspective of understanding sensing and feedback requirements of insect flight, these measurements are essential. Though the example insects used in the simulation use fruit fly and blowfly parameters, the theoretical approach is derived for a general insect exhibiting a timescale separation in hover and the qualitative results are applicable to the translational effects of dipteran flapping wing flight.

1.3 Previous Modeling Work

Previous research has attempted to generate models appropriate for estimating the dynamic properties and feedback requirements of dipteran flight. Experimental work includes Taylor and Thomas (2003c,a,b), who used measurements taken of tethered locusts in forced airflow to quantify the locusts' response to body pitch angle and velocity perturbations, and more recent work by Hesselberg and Lehmann (2007) identifying body drag as a dominant effect, as well as the experimental identification of yaw damping by Dickson et al. (2010). High fidelity aerodynamic modeling has been applied for perturbations about trim to quantify the system dynamics of several diptera (craneflies, droneflies, and hawkmoths in hovering flight) through linear modeling (Sun et al., 2010; Sun and Xiong, 2005; Gao et al., 2009). Models that may be developed without intensive computational solvers or experimental modeling are now of interest, as exemplified by recent analytic modeling efforts

(Cheng et al., 2010).

1.4 Approach

This research approaches the flight dynamics problem by quantifying the following:

1. **Wing Kinematics:** Automated reconstruction of an insect filmed under high speed videography is used to measure wing motions of freely-flying insects, and stereotyped wing kinematics patterns determined.

2. **Reduced Order Aerodynamics:** Aerodynamics at the insect scale are a subject of active research. Rather than explicitly solve the Navier Stokes equations, an experimentally derived reduced order aerodynamic model is posed in the context of insect egomotion (body translation and rotation).

3. **Rigid Body Dynamics:** The frequency separation between the insect body modes and high frequency excitation is exploited to allow classical Euler rigid body dynamics to be applied.

4. **System Identification:** The inputs and outputs of a nonlinear insect flight simulation built using the above components is analyzed in the frequency domain to assess linearity and measure experimental transfer functions. Beginning with analytical guesses, state space models are then fitted to derive reduced order models.

5. **High Fidelity Aerodynamics:** The reduced order models are directly com-

pared to the result of a high fidelity numerical solution to the Navier Stokes aerodynamics equations.

1.5 Dissertation Contributions

This dissertation presents the following contributions to insect flight:

- The first detailed measurement of trim and maneuvering wing kinematics for *Calliphorid* flies.
- Implementation of planar wing fitting and body exclusion rules to automated wing motion digitization.
- The first quantification of full path measurement error in automated wing motion digitization routines.
- A definition of biologically inspired control inputs that can be used for flight control.
- A method of placing the contemporary insect aerodynamics models in the context of insect body translation and rotation
- Transfer functions for longitudinal and lateral-directional hovering flight dynamics of *Drosophila*.
- The indication that linear time invariant modeling is sufficient to describe *Drosophila* flight dynamics about hover.

- State space dynamics models representing *Drosophila* flight dynamics about hover.
- The use of a biologically inspired feedback path to determine that sensing of insect body angular rates is sufficient for flight stabilization.
- An investigation of how *Drosophila* hovering flight dynamics are affected by rate feedback and morphological changes.
- Longitudinal and lateral-directional transfer functions for *Calliphorid* flies maneuvering about forward (cruise) flight.
- Application of control theory to determine all reachable states for bounded inputs to wing kinematics programs.
- A method of ranking wing kinematic input programs in terms of maneuverability.

1.6 Dissertation Organization

The organization of this dissertation is as follows. Chapter 2 presents an experimental method of determining the wing motions for dipteran (two-winged) insects. The method is an automated method that uses high speed videography of insects in free flight to generate time histories of the wing orientations. The digitization method is validated against at scale manufactured reference models, and the results are used to identify stereotypical kinematics for insect cruise and maneuvering flight. Digitized results are presented for *Calliphorid* flies.

Chapter 3 defines biologically inspired control inputs for the measured wing kinematics, and applies these to published *Drosophila* kinematics. These inputs are paired with an experimentally derived hovering aerodynamics model placed in the context of insect egomotion. The aerodynamics are paired with rigid body dynamics and system identification performed to determine a longitudinal flight dynamics model for an example *Drosophila*-like insect maneuvering about hover. Uncertainty estimates and dynamic properties for the model are determined, as well as the effect of mechanosensory feedback measured in previous work. Chapter 4 presents a similar study, but this time for the lateral-directional dynamics of the insect about hover. In both cases, the system is found to contain both stable subsidence modes and an unstable oscillatory mode that may be stabilized under the addition of mechanosensory feedback.

Chapter 5 examines the effect of additional un-modeled aerodynamic mechanisms via comparison to a numerical solution of the Navier Stokes equations of motion. The dynamic properties show qualitative agreement (with translational agreement much better than rotational), but the unmodeled aerodynamics increase the speed of response, in both convergence and divergence.

Chapter 6 further examines the effects of feedback on both the reduced order model and the full aerodynamic solution, and studies how the sexual dimorphism prevalent in many species affect the dynamic properties of the reduced order flight dynamics model. Feedback in the reduced order model shows a smooth progression from bare airframe unstable to feedback stabilized, while the full aerodynamic solution shows that the unmodeled dynamics increase the feedback required for an

equivalent performance specification. Finally, the flight dynamics of the female and male contain the same dynamic modes, with small changes in the actual magnitudes, suggesting that flight stabilization requirements for the two sexes is not significantly different.

Chapter 7 is an application of the reduced order model to compute and maximize the maneuverability of a micro aerial vehicle. Control theory is applied to determine the reachable states under a given set of inputs, and a method of ranking kinematic programs in terms of maneuverability is presented. The ranking is applied to the hovering fruit fly model developed in Chapter 3, showing dramatic differences in the size of reachable space. The method is applicable to micro air vehicle design studies, where the reduction of actuation count and effort is an important consideration

Finally, Chapter 8 extends the reduced order modeling method developed for diptera in hover to forward flight, using the *Calliphorid* kinematics presented in Chapter 2.

Chapter 2

Wing Kinematics Measurement

An essential component of a quantitative insect flight mechanics analysis is a detailed description of the wing motions an insect uses to effect motion throughout its environment. This chapter is concerned with measuring and parameterizing motion throughout an insect's wingstroke. The goal of the parameterization is to define intuitive control terms that may later be used as inputs for the insect flight control problem.

2.1 Previous Work

Previous research into recording kinematics began with Vogel (1967), who began to record gross stroke parameter variations in tethered *Drosophila*, such as stroke plane angle or amplitude. Both Ellington (1984b) and Zanker and Gotz (1990) continued this work for several insects, using high speed photography with a single camera and a side view to record the wingtip trajectory as projected in the longitudinal frame. Later work by Gotz (1987) introduced a wingbeat analyzer, the working principle of which was a photodiode measuring light levels underneath the insect's wings to infer both amplitude and frequency. Single camera analysis predominated kinematics recording for some time, such as Ennos (1989) work with dipterans (two-winged insects). Such an approach allows estimation of wingbeat

frequency, the amplitude of the wingstroke (as measured peak-to-peak), and the orientation of the plane[1] in which the insect flaps (not necessarily simultaneously). Digitization was primarily a manual and tedious process, though attempts were eventually made to use software to digitize wing markers and record wing steering muscle inputs as well (Balint and Dickinson, 2004; Sherman and Dickinson, 2003). Much of the work focused on tethered insects for ease of filming, though in some cases the motion of the tether was prescribed to determine the kinematic response to such motion (Sherman and Dickinson, 2003, 2004).

Eventually, multiple cameras were used to allow determination of the wing orientation (assumed rigid) in three dimensional space (Fry et al., 2003). Detailed kinematic measurements enabled replay through robotic apparatus (Balint and Dickinson, 2004). Once the robotic apparatus was equipped to record forces and moments generated by the motions, the first basis of an aerodynamics model could be generated. The manual three-camera setup became the standard method of recording kinematics, though modeling was limited to either the gross stroke parameters as above or directly replaying the measured kinematics through a robotic apparatus or simulator (Altshuler et al., 2005; Vance et al., 2005; Vance and Humbert, 2010; Vance et al., 2010). The next major upgrade was to apply an automated method to digitizing *Drosophila* kinematics (Ristroph et al., 2009; Fontaine et al., 2009; Ristroph et al., 2010).

[1]The actual flap pattern is rarely a plane, but a plane is typically defined, using either the peak-to-peak wing positions or a linear regression to the wingstroke points.

2.2 Insect Subjects and Experimental Apparatus

Fruit fly (*Drosophila*) kinematics are available from previous literature (due to their ubiquitous presence in genetic research labs) (Dickinson et al., 1999), but detailed free flight kinematics for *Calliphorid* flies had not yet been recorded. Though fruit fly wing kinematics and aerodynamics have previously been characterized, their visual and mechanical sensing capabilities are not yet well known, which would be necessary to understand the flight dynamics model developed in the context of insect sensing. In contrast, sensory feedback measurements for blowflies (*Calliphoridae*) are readily available, but kinematic and aerodynamic data are not.

An experimental test rig shown in Fig 2.1 was constructed to allow detailed measurements of free flight maneuvering in *Calliphorid* species. The experimental apparatus consists of three Vision Research Phantom V710 high speed video cameras and lighting array, orthogonally-mounted about a 10in x 10in x 8in Plexi-Glass test section into which insects are introduced. A calibrated low speed wind tunnel has been constructed around the test section in order to allow steady wind conditions to be applied, and a regulated supply of compressed air allows repeatable gusts to be introduced through a port in the chamber as well. *Calliphorid* insects captured at the University of Maryland horse farm were allowed to freely fly within the chamber, and a trigger mechanism was built to automatically record sequences when an insect flew within the focal volume. Images were recorded at a resolution of 1280 x 800 pixels with a 30 μs exposure and 7002 Hz framerate.

A library of *Calliphorid* flight sequences incorporating maneuvering free flight

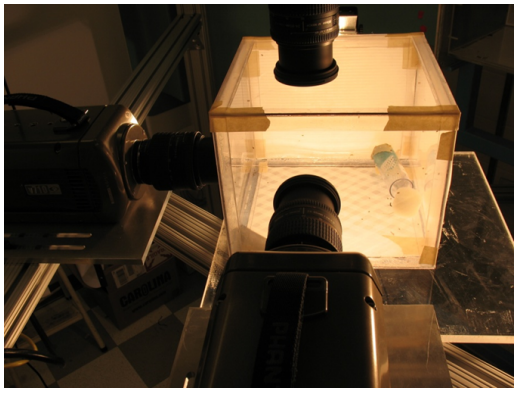

Figure 2.1: Experimental test rig and free flight chamber.

behavior in both quiescent air and gusting conditions has been collected. Digitization is traditionally accomplished by manually aligning a wireframe model of the insect to each of the three views, a labor-intensive task that can take weeks or months for a single sequence. Research on *Drosophila* flight at Cornell University has demonstrated success using automated tracking techniques such as Hull Reconstruction Motion Tracking (HRMT) (Ristroph et al., 2009), and this study used a modified version of the *Drosophila* tracking code.

2.3 Kinematics Digitization

2.3.1 Coordinate Definitions

The description of the insect flapping motion requires a family of axes centered at the insect wing hinge. Approximating the wings as rigid bodies, measured insect kinematics exhibit a roughly planar flap motion which is represented using 2-3-2 Euler angles. Define by reference to Fig. 2.2a a set of stability axes $\mathcal{S} = \{\hat{s}_x, \hat{s}_y, \hat{s}_z\}$ passing through the insect center of mass G, the stroke plane angle β as the angle

about the pitch axis to an idealized planar stroke motion, and a coordinate axes set aligned with this plane the stroke plane axes $\mathcal{P} = \{\hat{p}_x, \hat{p}_y, \hat{p}_z\}$. Define $\mathcal{R} = \{\hat{r}_x, \hat{r}_y, \hat{r}_z\}$ a set of axes that move along with the right wing, with $\hat{r}_z = \hat{p}_z$ and $\hat{r}_y$ to extend toward the wing tip as in Fig. 2.2b. Similarly, define $\mathbf{L} = \left\{\hat{l}_x, \hat{l}_y, \hat{l}_z\right\}$ for the left wing, with $\hat{l}_y$ extending inboard along the left wing spanline. The additional definition of the geometric angle with respect to the stroke plane as wing pitch angle η provides the notation necessary to describe the orientation of two rigid wings at an instant in time.

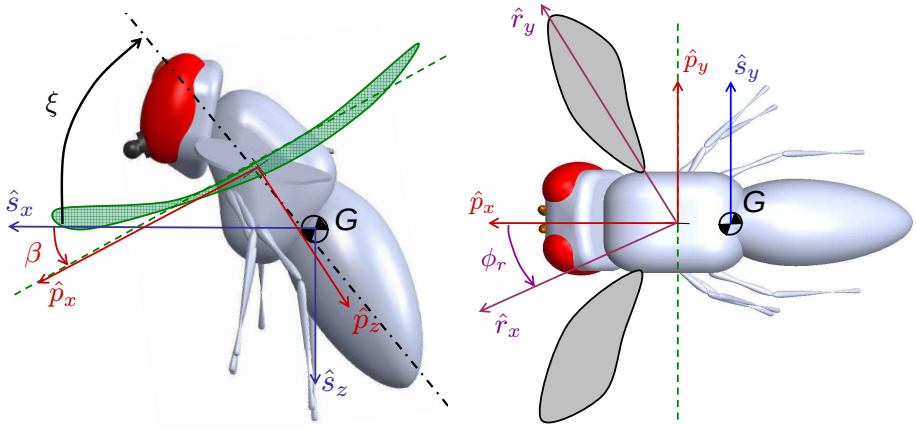

(a) Stroke plane axes/angle β, body hovering angle ξ

(b) Stroke angle ϕ_r and $\mathcal{R}$ axes

Figure 2.2: Axes and angle definitions.

2.3.2 Digitization Algorithm

Once a flight sequence has been captured, kinematics digitization consists of three major components: image processing, volume pixel (voxel) extraction, and feature identification/model fitting.

In the image processing stage, the fly is isolated from the background and

noise in a cropped version of the image (400 by 400). The techniques used in this are background subtraction and masking by a thresholded version of the image. Each of the images is then corrected for alignment and magnification errors to create orthogonal profiles of the animal.

In the voxel identification stage, a search space is identified for the insect, and the pixels in each camera are compared to determine the three dimensional volume obscured by the fly in the capture volume. Mathematically, this approach is analogous to a computer-aided-drawing program taking the intersection of each of the animal's orthogonal profiles to reconstruct its volume.

In the model fitting stage, the voxels are grouped into head, body, and wing groups by an iterative distance-minimizing approach. The head and body groups are combined and the centroid of the group used to estimate the body center of mass location. The body orientation is determined by the identified semi-minor and semi-major axes of a principal component analysis conducted on the body voxels. The wing orientations are estimated by first isolating the wings from their hinges, then conducting principal component analysis and a planar fit to the outboard section of the wing voxels.

The above three steps begin with three-view images like those shown in Fig 2.3(a-c) and generate as output volume reconstructions like those shown in Fig 2.3(d-f) and Fig 2.4.

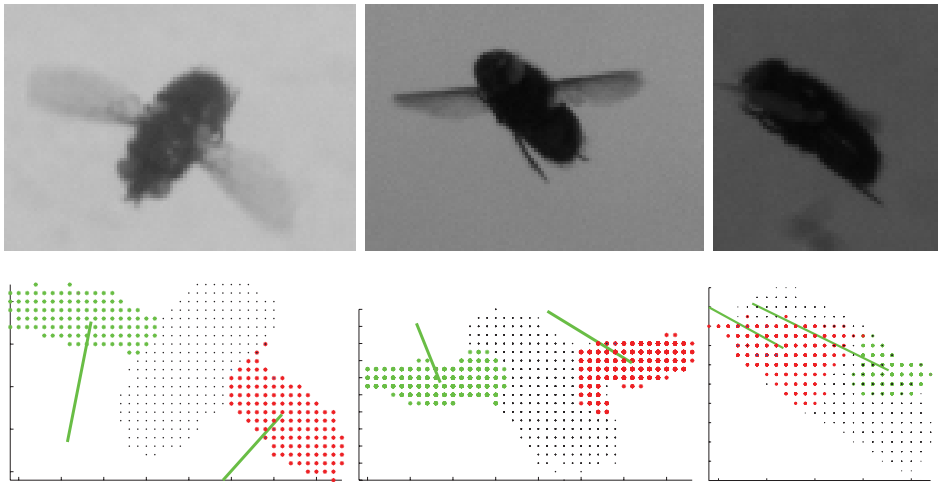

(d) top (e) front (f) side

Figure 2.3: Example images versus voxel reconstructions.

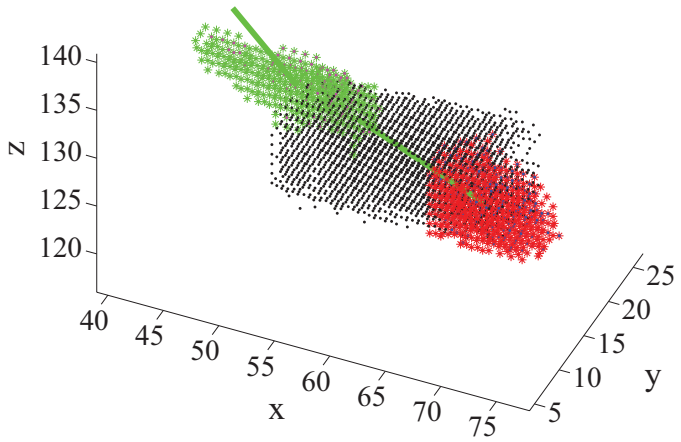

Figure 2.4: Visual hull reconstruction.

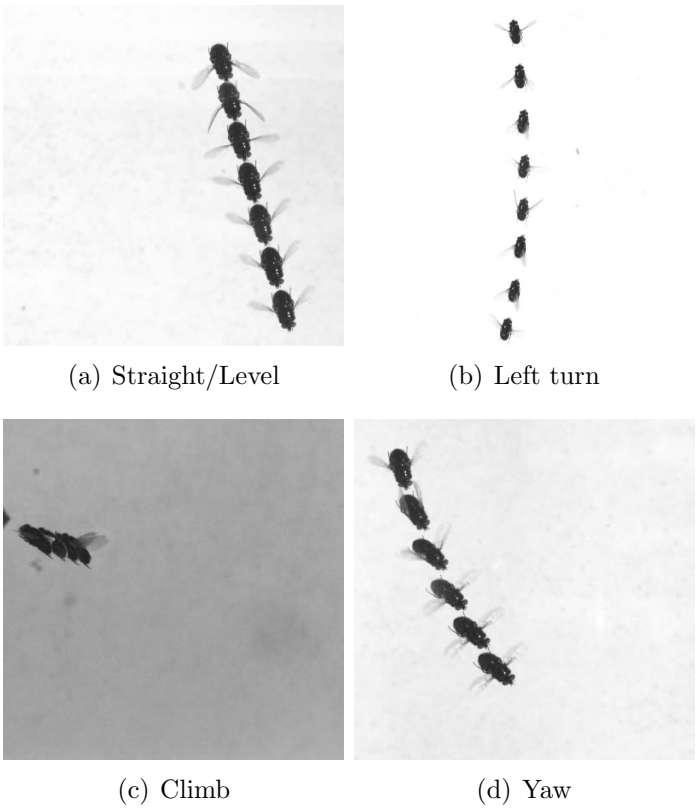

(a) Straight/Level (b) Left turn

(c) Climb (d) Yaw

Figure 2.5: Digitized flight sequences include a (a) straight and level sequence, (b) level left turn, (c) climb initiation (d) yaw motion (sideslip). All images are top views shown at 70Hz except for (c), which is a side view shown at 140Hz.

2.3.3 Digitization Results

Digitization was conducted for flight sequences including straight and level flight, a level left turn, initiation of climbing flight, and a yaw motion (saccade) (Bender and Dickinson, 2006b), as seen in Fig 2.5. All of the flight sequences start in forward flight and are in quiescent air.

Principal component analysis works quite well for stroke and deviation angle identification, shown in Fig 2.6. A number of modifications were necessary to the automated HRMT approach in order to yield accurate results for *Calliphorid* wing pitch angles. Previously, wing pitch angle was unreliable, due to body voxels that

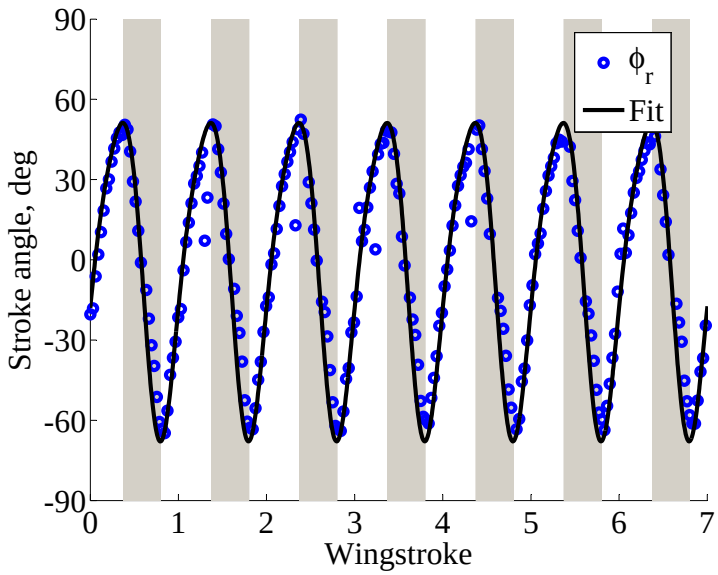

Figure 2.6: Stroke angle is well detected by principal component analysis, and multiple wingstrokes in straight and level flight provide ample measurement of the nominal kinematic pattern.

were assigned to the wing grouping and errors in the method of determining a chord vector.

A spherical body exclusion rule dramatically reduced the body pixels incorrectly assigned to wings, as seen in Fig 2.7. The wing angle detection method was also revised. Wing angle estimation previously estimated the wing chord vector from points having the most distance to each other. Instead, each wing is now modeled as a plane and the algorithm computes a least-squares best fit to the function

$$x = b_0 + b_1 y + b_2 z. \tag{2.1}$$

Both modifications markedly improved the wing angle detection, as seen in Fig 2.8.

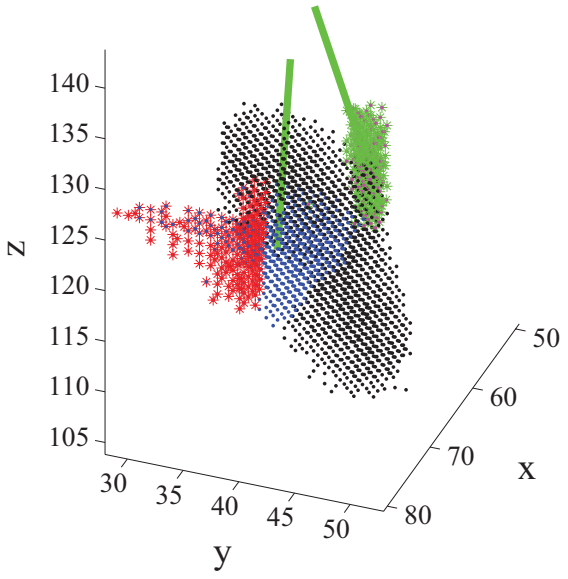

Figure 2.7: A spherical exclusion rule dramatically reduces the number of body voxels incorrectly assigned to the wings. Blue indicates body voxels that were previously detected as wing voxels.

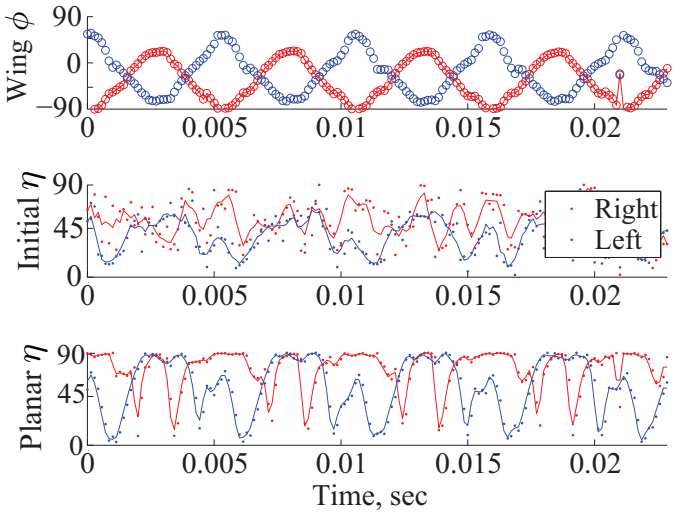

Figure 2.8: Modifications to the wing angle detection algorithm improved the results dramatically.

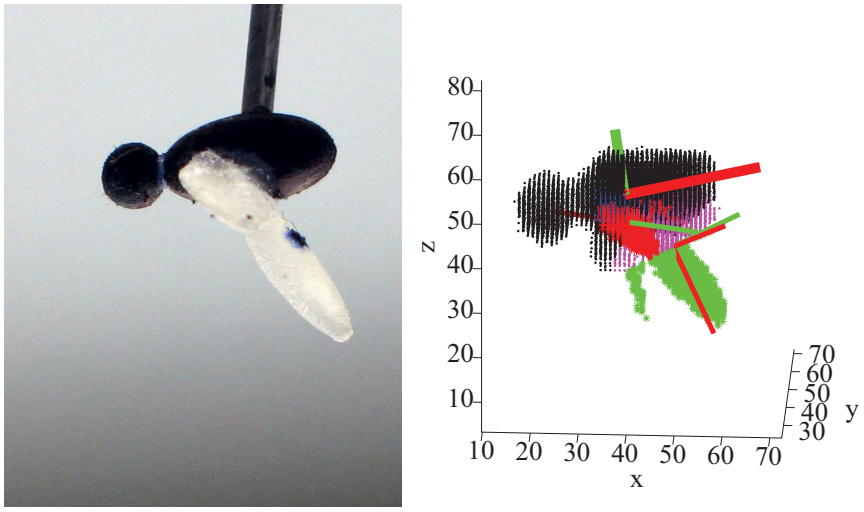

Figure 2.9: A reconstruction of the 45° insect model reconstruction shows an occlusal defect on the left wing.

2.3.4 Digitization Accuracy

Previous work has estimated accuracy of a digitizing method using synthetic views of a computer graphics insect (Ristroph et al., 2009). A series of rapid-prototype insect models with wings in known positions were manufactured and accuracy of the technique estimated by placing the model in the capture volume and digitizing the resulting images. The advantage of such a technique over a typical calibration with synthetic images is that it provides a very realistic estimate of the error in the entire measurement system, including imaging errors, lens distortion, camera misalignment. These effects are not quantified with a synthetic image calibration, which provides an error estimate that only includes the digitization method. A calibration sequence showing an occlusion (a portion of space obscured in all three cameras) is shown in Fig 2.8. The occlusal defect on the left wing raises the error in the wing angles from a mean of 7° to a mean of 8.3°.

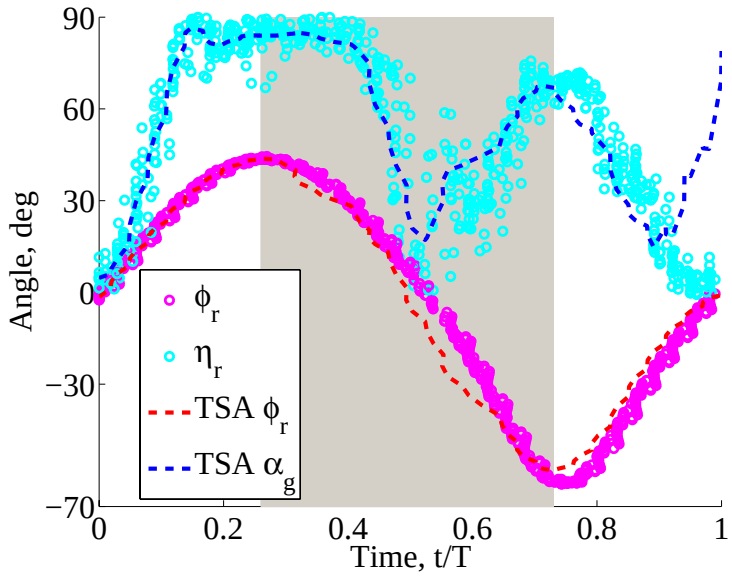

Figure 2.10: Time synchronous averaging is used to identify a nominal stroke pattern associated with a reference condition (straight and level flight shown).

2.4 Kinematics Reduction

2.4.1 Time Synchronous Averaging

For insects in an established flight condition, repeated wingstrokes (see Fig 2.6) offer a method of improving the wing kinematics angle estimation by offering multiple measurements of the nominal wingstroke. This improvement was realized through time synchronous averaging, a method (often used for geartrain diagnosis) which aligns each waveform of a periodic signal and averages each wingstroke at each point during the wingstroke (Dalpiaz et al., 2000). Time synchronous averaging allowed curve fits to be applied to a single stereotypical curve fit with a standard error of less than 2°, as seen in Fig 2.10.

2.4.2 Curve Fitting

Previous *Drosophila* kinematics work had assumed a planar stroke, sinusoidal wing motion in ϕ, and a smoothed square wave for η_g. The assumption of planar stroke was retained for *Calliphora*, but both stroke angle and wing angle showed deviations from this pattern, as seen in Fig 2.10, and sinusoidal curve fits often resulted in a fit with an unacceptably low coefficient of determination R^2. Adding a "stretch parameter" d to the ϕ sinusoid as

$$\phi(t) = \Phi \cos(2\pi f t + \psi_1)(d \cos(\pi f t + \psi_2)^2 + 1) + \phi_{\text{off}} \tag{2.2}$$

and modeling η as a combination of a sinusoid and smoothed square wave

$$\begin{aligned} \eta(t) = \; & A_1[.5 \tanh(b_1 \sin[2\pi f t + e]) + .48] \sin(2\pi f t + \pi + e)^2 \\ & + A_2[.5 \tanh(b_2 \sin[2\pi f t + c]) + .48] \tanh(3 \sin(2\pi f t + c)) + d \end{aligned} \tag{2.3}$$

improved fit quality to yield $R^2 > 0.9$. Wing stroke angle and wing pitch angle fits are shown in Fig 2.6 and 2.11.

2.5 Summary

In this chapter, an automated approach was used to extract kinematics from high speed videography. A body exclusion rule and planar wing fitting was added to improve the quality of the wing orientation estimates. The method was validated using manufactured reference models, representing the first published uncertainty data

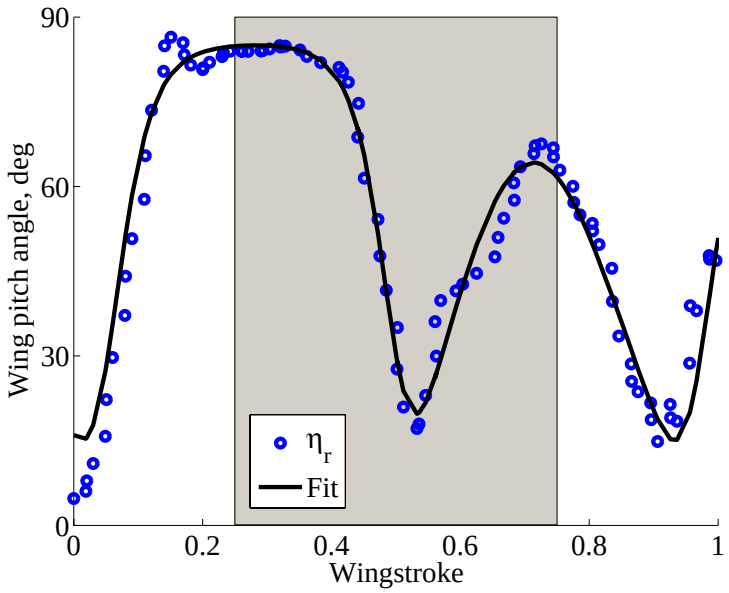

Figure 2.11: Wing pitch angle in forward flight is more complex than a smoothed square wave.

for three-camera insect wing orientation measurement to include the full extraction path. Trim (stabilized forward flight) and maneuvering kinematics were identified for *Calliphorid* flies, a genus for which detailed kinematic data was previously unavailable. Time synchronous averaging was used to determine stereotyped reference kinematics, and curve fits were populated with biologically inspired kinematic parameters which are used as inputs to a reduced order flapping flight dynamics model developed in the remainder of this dissertation.

Chapter 3

Longitudinal Hover Dynamics

3.1 Introduction and Background

We first analyze longitudinal flapping flight mechanics about hover, using as an example *Drosophila melanogaster*, or the common fruit fly. Fruit flies are abundant in research settings, owing to their rapid lifecycle that allows tractable genetic studies. Correspondingly, they have one of the most well-understood genetic structure amongst insects. For the goal of flight dynamics research, they are easy to keep and induce to fly, so that both hovering kinematics and experimental aerodynamic measurements may be found in published literature (Dickinson et al., 1999). Additionally, there is a large phenotypic variation amongst differing communities and for differing sexes. This variation will enable the study of the effects of large morphological variations in Chapter 6.

This section presents the hovering *Drosophila* wing kinematics used in simulation, a review of the experimental aerodynamics model, and other governing equations used for analysis and simulation.

3.1.1 Wing Kinematics

Section 2.3.1 defined wing stroke plane inclination β, stroke angle ϕ, and a wing pitch angle α_g for each wing, and introduced the coordinate frames used in

this study, and Fig 3.1 is repeated here for clarity. For a flapping *Drosophila* in or

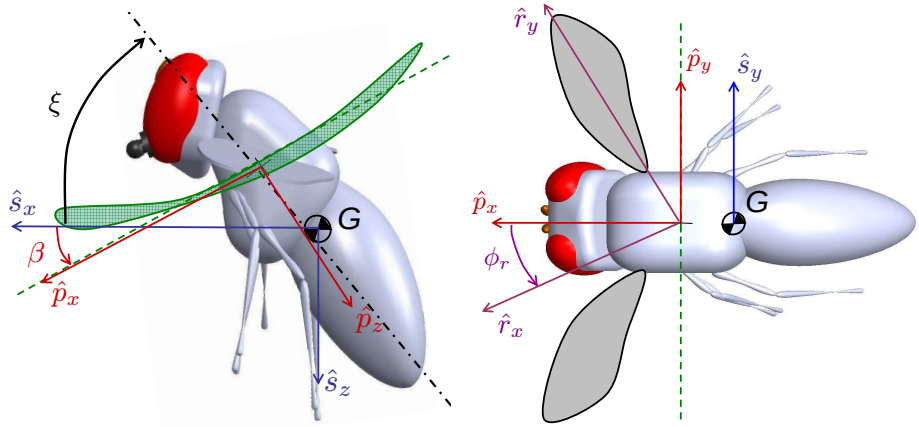

(a) Stroke plane axes/angle β, body hovering angle ξ

(b) Stroke angle ϕ_r and $\mathcal{R}$ axes

Figure 3.1: Axes and angle definitions.

near hover, the flap angle ϕ_r undergoes a harmonic motion sufficiently represented as a sinusoid (Dickinson et al., 1999)

$$\phi_r(t) = -\Phi_r \cos(2\pi f_r t) + \phi_{\text{off,r}} \ , \tag{3.1}$$

where Φ_r gives the amplitude of each wingstroke, $\phi_{\text{off,r}}$ the deviation of the point about which the wing oscillates, and f_r the right wing flap frequency. The geometric angle of attack α_g exhibits a harmonic motion roughly resembling a modified square wave, which allows the advancing and retreating strokes to both share a positive angle of attack.

3.1.2 Control Parameters

As postulated by Vogel (1967) and later quantified experimentally by Fry et al. (2003), insects modulate the time forces and moments applied to wingstrokes by modification of several wingstroke parameters. The control inputs considered in this chapter are the biologically-motivated choice of flap frequency f in Hz, the flap amplitude Φ as defined in section 3.1.1, stroke plane angle β, and the mean position (center) of wing oscillation ϕ_{off}. In addition to the mathematical definitions in section 3.1.1, several control parameters may be seen graphically in Fig. 3.2. Right and left wing variables may be interpreted as longitudinal and lateral control inputs using the transformation

$$\begin{bmatrix} \Phi_c \\ \Phi_d \\ \beta_c \\ \beta_d \end{bmatrix} = \begin{bmatrix} 0.5 & 0.5 & 0 & 0 \\ 0.5 & -0.5 & 0 & 0 \\ 0 & 0 & 0.5 & 0.5 \\ 0 & 0 & 0.5 & -0.5 \end{bmatrix} \begin{bmatrix} \Phi_r \\ \Phi_l \\ \beta_r \\ \beta_l \end{bmatrix}, \tag{3.2}$$

where $[\,]_c$ represents a collective (symmetric) input and $[\,]_d$ represents a differential (lateral-directional) input. Parameter variations are generally small, and the variations remain remarkably small even for aggressive maneuvers such as fast 90° collision avoidance maneuvers known as saccades (Fry et al., 2003), but are nonetheless fundamental for the control of the insect. As an example, Table 3.1 and 3.2 shows nominal and maneuvering parameters for *Calliphorid* flies maneuvering throughout the sequences in Fig 2.5. Since this chapter addresses longitudinal motion, we de-

Sequence	(β_r, β_l)	(β_c, β_d)
S+L	$(19.5, 21.4)$	$(20.5, -0.9)$
Turn	$(15.3, 24.0)$	$(19.7, -4.4)$

Table 3.1: Stroke plane inclination in a turning *Calliphorid* shows differential stroke plane inclination perturbation and constant collective stroke plane inclination

.

Parameter	Collective	Differential
Frequency	211-215 Hz	0 Hz
Amplitude	107-112°	0.8-21°
Offset	0.3-6°	16-17°

Table 3.2: Range of parameter variation observed in *Calliphorid* flies throughout maneuvering flight.

scribe the behavior of the right wing and assume symmetry in the left wing frame and the subscripts [ ] may be suppressed until Chapter 4.

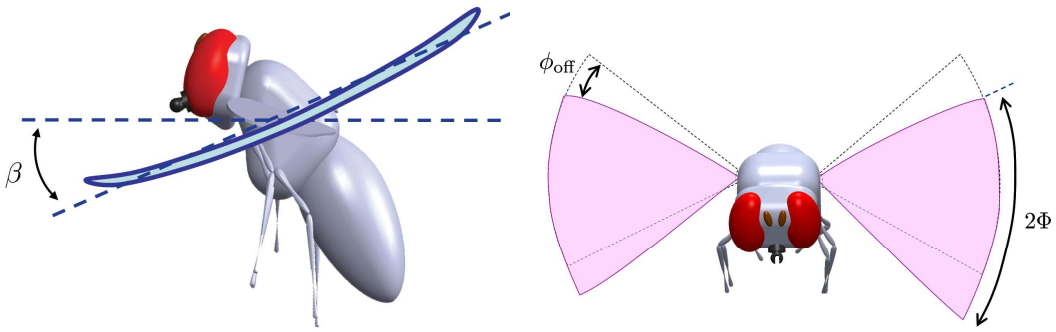

(a) Stroke plane angle input β (b) Stroke offset ϕ_{off} and amplitude Φ

Figure 3.2: Insect flapping kinematics parameters are used as control inputs to model.

3.1.3 Aerodynamics

A variety of effects, predominantly unsteady, are known to be active during an insect's flight. A thorough treatment of these effects is outside the scope of this section and may be found in Ansari et al. (2006); Sane (2003). Instead, this

treatment reviews the largest contribution to in-flight insect forces: "translational" lift and drag.

3.1.3.1 Translational Lift and Drag

Wing "translational lift" is the largest component (approximately 65-85%) of an insect's lift production in hover and the most straightforward of the lift mechanisms known to be active, but includes a number of unsteady effects via experimental coefficients. The translational component of insect lift can be represented using (Ellington, 1984a)

$$L(t) = \frac{1}{2}\rho S|u_t(t)|^2 \hat{r}_2^2 C_L[\alpha(t)], \tag{3.3}$$

where the instantaneous lift force L is written as a function of the air density ρ, the wing area S, tip velocity u_t, nondimensional second moment of area $\hat{r}_2^2$, and an experimentally-determined lift curve slope (Sane and Dickinson, 2002)

$$C_L[\alpha(t)] = 0.225 + 1.58\sin(2.13\alpha_g - 7.2). \tag{3.4}$$

The second moment of area $\hat{r}_2^2$ may be defined in terms of the normalized chord $\hat{c} = 1/2\text{Æ}R\, c/R$ and normalized radius $\hat{r} = r/R$ as $\hat{r}_2^2 = \int_0^1 \hat{c}\,\hat{r}^2\, d\hat{r}$ (Ellington, 1984c).

This model is referred to in the insect flight community as "quasi-steady" because the only time dependent variables in this equation form are the kinematic variables $u_t(t)$ and $\alpha(t)$, yet we know that insect aerodynamics are intrinsically unsteady (Dickinson and Gotz, 1999). Consequently, the nondimensional $C_L[\alpha(t)]$

is a curve fit to experimental data that hides a number of unsteady effects, such as the effect of starting and stopping vortices (Wagner effect) (Dickinson, 1996) and the mechanism of delayed stall. Though these are unsteady effects, the $C_L[\alpha]$ curve fit is considered to be a function purely of the instantaneous angle of attack, hence the equations appear in the same form as an aeroelastic analysis that neglects such effects. Because of this, an aerodynamic model presented in quasi-steady form may either neglect unsteady effects or treat them via modification of the $C_L[\alpha(t)]$ as done in this dissertation. The other nondimensional term, $\hat{r}_2^2$, addresses the nonuniform spanwise lift distribution and is a function of the wing's shape (Ellington, 1984c). A key feature of the aerodynamic model is the reduction of forces by the dynamic pressure $\frac{1}{2}\rho u_t^2$, where the tip velocity $u_t = \dot{\phi}R$ is a function of the wing flap angle derivative $\dot{\phi}$ and the wing length R.

Translational drag is the component of force production acting opposite the direction of wing motion (in the stroke plane) and has a parallel representation to the translational lift described above. Introducing the experimentally-determined nondimensional coefficient $C_D[\alpha]$ to describe this force, one may model translational drag as (Dickinson et al., 1999)

$$D(t) = \frac{1}{2}\rho S|u_t(t)|^2\hat{r}_2^2 C_D[\alpha(t)], \tag{3.5}$$

$$C_D[\alpha(t)] = 1.92 - 1.55\cos\left(2.04\alpha_g - 9.82\right). \tag{3.6}$$

3.1.4 Wingstroke-Averaged Forces and Moments

Flight dynamics often involves a system (airframe) forced by high frequency forces, creating small high frequency motions (vibration) which are typically ignored and gross translation/rotation (the flight path). The solution of interest is the flight path, or asymptotic solution, the speed of which is limited by the airframe inertia. By reference to results from "two-timing" averaging theory (Cole, 1968), one can represent the asymptotic solution of a system whose response is on slow timescales with periodic excitation on fast timescales as the effect of the excitation averaged over the fast timescale, subject to specific constraints on the system (Kevorkian, 1966; Cole, 1968), an approach that works well for systems with body dynamics slower than 1/10th the dynamics of the forcing function (Deng et al., 2006a). Deng et al. applied this concept to the design of flight control for a mechanical flapper (Deng et al., 2006b; Schenato, 2004) by viewing the averaging process as a nonlinear map from wrench efforts to state outputs. In this study, we investigate the details of creating a map from kinematic input parameters (controls) to state outputs and the dynamic properties of the resulting system, determining the modal (asymptotic) airframe response time scales via computed frequency responses.

Under the assumption that the aerodynamic timescales are an order of magnitude faster than the body dynamics, the wing aerodynamic forces are averaged over one wingstroke to determine the motion of the insect body. Moreover, finding the effective force over each wingstroke provides a mathematically straightforward means to impose the constraint of the control variables being fixed over each wingstroke.

Such a constraint is useful because insects, unlike larger animals such as birds or flying mammals, do not posses the computational bandwidth to control wing motions more than once per wingstroke (Autrum, 1958).

The effective, or mean, lift force over one wingstroke is

$$L_{\text{avg}}(t) = \frac{1}{T}\int_0^T L(t)dt, \tag{3.7}$$

where T is the period of the wingstroke given by $T = 1/f$. An analytic solution to this lift integral would provide an algebraic expression for the effective lift force acting over a wingstroke, dependent on: the wing geometry (size and shape), the environment (density), the wing aerodynamic performance (via lift curve slope), the longitudinal state variables, and a subset of the control inputs. The general integration is a numerical task due to the numerous "nested" trigonometric functions. Restricted solutions to the integral may be found by recognition that the linearization performed later does not require a global solution to this integral, but rather the exact solution at a point and its functional dependence on the state and wing flap coordinates (partial derivatives). The drag equation must similarly be averaged over one wingstroke.

3.2 Derivation of Linearized Flight Dynamics about Hover

In this section, the experimental aerodynamics model is extended to include perturbation velocities and the local and instantaneous forces are approximated by wingstroke-averaged forces to provide estimates of the vehicle stability and control

derivatives.

3.2.1 Governing Equations

Assuming a rigid insect body B, the motion of the body-fixed stability frame $\mathcal{S}$ is a function of the applied forces and moments and can be written as a system of ordinary differential equations (Nelson, 1989). The longitudinal portion of these equations are

$$X = m\left(\dot{u} + qw - rv\right) + mg\sin(\theta) \tag{3.8a}$$

$$Z = m\left(\dot{w} + pv - qu\right) - mg\cos(\theta)\cos(\phi) \tag{3.8b}$$

$$M = I_{yy}\dot{q} - I_{xz}(\dot{r} + pq) - \left(I_{yy} - I_{zz}\right)qr, \tag{3.8c}$$

where X, Z, and M are the aerodynamics forces and moment, $\boldsymbol{\omega}^B = p\hat{s}_x + q\hat{s}_y + r\hat{s}_z$ the rotation rate of frame $\mathcal{S}$, and $\boldsymbol{v}^G = u\hat{s}_x + v\hat{s}_y + w\hat{s}_z$ the inertial velocity of the center of mass G as seen in Fig. 3.3.

3.2.2 Hover Equilibrium Trim Solutions

Using the wingstroke averaged forces and moments, under the assumption of longitudinal motion ($p_0 = 0$, $r_0 = 0$,$v_0 = 0$,$\phi_0 = 0$), and writing each variable as a nominal condition (notated as $[\,\cdot\,]_0$ and a small perturbation $\Delta[\,\cdot\,]$, the general equation for motion along the s_x axis may be written for hover (where the nominal

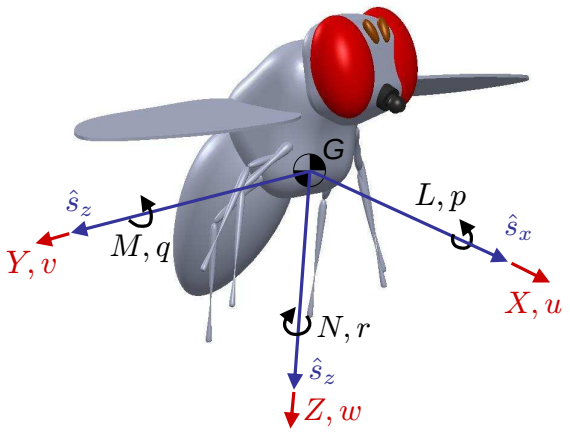

Figure 3.3: Definitions of stability frame velocities $\boldsymbol{v}^G = u\hat{s}_x + v\hat{s}_y + w\hat{s}_z$, rotation rates $\boldsymbol{\omega}^B = p\hat{s}_x + q\hat{s}_y + r\hat{s}_z$, forces $\boldsymbol{F} = X\hat{s}_x + Y\hat{s}_y + Z\hat{s}_z$, and moments $\boldsymbol{M} = L\hat{s}_x + M\hat{s}_y + N\hat{s}_z$.

$w_0 = 0$ and $q_0 = 0$) as

$$X_0 + \Delta X - mg\left[\sin(\theta_0) + \cos(\theta_0)\sin(\Delta\theta)\right] = m\left[\Delta\dot{u}\right]. \tag{3.9}$$

At the trim condition, the small perturbation terms $\Delta[\,\cdot\,] = 0$, so eqn (3.9) becomes

$$X_0 = mg\sin(\theta_0). \tag{3.10}$$

Calculation of a trim condition requires specification of a nominal hovering trim angle θ_0. Without restriction, we can define the stability axes such that $\theta_0 = 0$. To do so, define the pitch angle through which the body axes (aligned with the insects longitudinal morphological axis) must be pitched through in order to become coincident with the stability axes as the "body hovering angle" ξ (shown in Fig. 3.1), then project the moment of inertia tensor through the single axis rotation, and define the distance from G to thorax as $\boldsymbol{r}_{G/t} = d_x\hat{\boldsymbol{s}}_x + d_z\hat{\boldsymbol{s}}_z$, where a symmetrically-located

mass center is chosen to preserve longitudinal motion.

The hover condition along $\hat{s}_x$ reduces to $X_0 = 0$. A similar derivation of the hover condition along $\hat{s}_z$ and about $\hat{s}_y$ gives $Z_0 = mg$ and $M_0 = 0$.

Hover equilibrium now reveals multiple solutions for trim inputs. In unaccelerated hover with a level stroke plane, vertical force equilibrium requires that $Z_0 = 2L_{\text{avg}}(t) = mg$, which may be trimmed via either flap frequency or stroke amplitude inputs. Moment equilibrium reveals that an insect similarly has redundant control inputs via stroke plane angle, stroke angle offset, or a coupled input of both. For a given stroke plane angle input β_0, the insect may enforce pitch axis trim via

$$\phi_{\text{off},0} = \sin^{-1}\left(\frac{\sin\beta_0\, d_z - \cos\beta_0\, d_x}{r_a \cos(2\beta_0)}\right), \tag{3.11}$$

where r_a is the spanwise distance outboard to the point at which the lift and drag forces may be considered to act. Eqn (3.11) demonstrates that a solution can only exist for $\beta_0 \neq \pm\frac{(2\,n-1)\pi}{4}$, $n = 1, 2, 3....$ The dependence on body hovering angle ξ may be seen in Fig. 3.4.

A detailed estimation of the distance r_a, which is involved only in the pitch dynamics, may be addressed via computational fluid dynamics studies and is outside the scope of this investigation. The point has been shown experimentally to be roughly constant with respect to changes in angle of attack (Dickson et al., 2008). Initially, the centroid may seem a wise choice, but since lift forces are proportional to the square of the local velocity, the actual location of this point is more subtle. Application of blade element theory with a fixed spanwise blade pitch yields $r_a =$

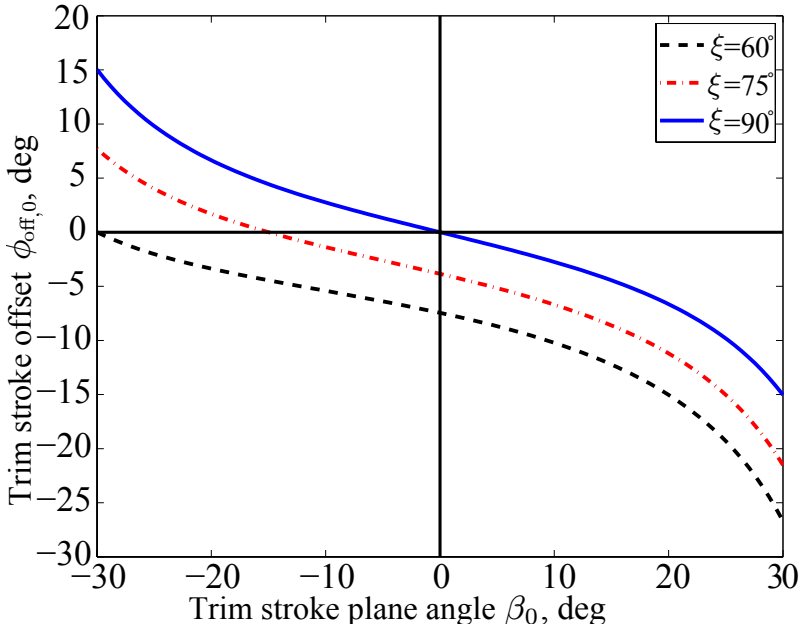

Figure 3.4: Trim inputs β_0 and $\phi_{\text{off},0}$ as functions of body hovering angle ξ.

$3/4R$, a value commonly used in helicopter results (and the reason why the twist of a linearly twisted helicopter blade is specified at this point), which has been used as a first approximation for this point.

3.2.3 Inclusion of Perturbation States in the Quasi-Steady Form

The current practice of posing the aerodynamics model without any state dependency is useful from a data reduction standpoint but does not provide insight into how perturbations of each of the state variables from the operating point affect the aerodynamic forces and moments produced on the vehicle. The recent discovery of "flapping counter-torque" (Hedrick et al., 2009) as a means to arrest a turning maneuver is a result of the consideration of perturbation velocities for yaw rotation, which is now examined for the general longitudinal case.

We consider inclusion of the perturbation velocities $\boldsymbol{v}^G = u\hat{s}_x + v\hat{s}_y + w\hat{s}_z$,

and rotation $\boldsymbol{\omega}^B = p\hat{s}_x + q\hat{s}_y + r\hat{s}_z$. Intuitively, one would expect no aerodynamic dependency on inertial position or orientation.[1] Both $\boldsymbol{v}^G$ and $\boldsymbol{\omega}^B$ have two major effects on the wing lift and drag production: (a) they change the local velocity (and hence dynamic pressure) at an airfoil section, and (b) they also change the local angle of attack at each airfoil section.

3.2.4 Velocity Components

In order to determine the incremental lift and drag acting on an elemental wing section, one must consider the total velocity incident that wing, defined as $\boldsymbol{v} = \boldsymbol{v}_\phi + \boldsymbol{v}^G + \boldsymbol{v}_\omega$, where $\boldsymbol{v}_\phi$, $\boldsymbol{v}^G$, and $\boldsymbol{v}_\omega$ are the velocity components due to flapping, body translational rate, and body rotational rate, respectively. To facilitate numerical simulation, the components are resolved in the wing frame as $\boldsymbol{v} = v_x\hat{r}_x + v_y\hat{r}_y + v_z\hat{r}_z$.

3.2.4.1 Local Velocity Component due to Flapping

The component of velocity due to wing flapping at a distance r along the wing spanline is $\dot{\phi}r$ acting along the $\hat{r}_x$ axis or $\boldsymbol{v}_\phi = \dot{\phi}\, r\, \hat{r}_x$. The original model evaluates this function only at the wing tip for $u_t = \dot{\phi}R$.

[1] Note that aircraft are occasionally modeled (in reduced order models used for control design) with a dependency on roll angle ϕ that arises due to the sideslip velocity v ensuing from such an angle, as a ϕ estimate is often more readily available from an instrumentation system and is then used to effectively estimate v. Theoretically, a formulation including v is well-posed.

3.2.4.2 Local Velocity Component due to Body Velocity

In the rotating right wing frame $\mathcal{R}$, the body translation velocity $\boldsymbol{v}^G$ has the components $\left[\boldsymbol{v}^G\right]_{\mathcal{R}} = u_r\hat{r}_x + v_r\hat{r}_y + w_r\hat{r}_z$, related by the rotation matrix R_{RS} defined in eqn (3.13).

$$\left[\boldsymbol{v}^G\right]_{\mathcal{R}} = R_{RS}\left[\boldsymbol{v}^G\right]_{\mathcal{S}} \tag{3.12}$$

$$R_{RS} = \begin{bmatrix} c_{\phi_r}c_\beta & -s_{\phi_r} & c_{\phi_r}s_\beta \\ s_{\phi_r}c_\beta & c_\phi & s_{\phi_r}s_\beta \\ -s_\beta & 0 & c_\beta \end{bmatrix} \tag{3.13}$$

Similarly, the velocities seen on the left wing are given by R_{LS}, the compliment of R_{RS}. Though a function of the flap angle ϕ_r and stroke plane angle β, $\left[\boldsymbol{v}^G\right]_{\mathcal{R}}$ is constant with respect to wing spanwise distance.

3.2.4.3 Local Velocity Component due to Rotation Rates

The body rotation rate $\boldsymbol{\omega}^B$ enters in a slightly more complicated fashion. The velocity of a point P due to rotation rate $\boldsymbol{\omega}^B$ about the center of mass G can be expressed as $\boldsymbol{v}_\omega = \boldsymbol{\omega}^B \times \boldsymbol{r}_{G/p}$, where $\boldsymbol{r}_{G/p}$ is the vector from G to P. Unlike the velocity components due to body translation, the velocity components due to body rotation are functions of the distance r outboard. The choice of stability axes as a basis for $\boldsymbol{\omega}$ requires a transformation R_{RS} to express it in the wing frame for numerical computation.

3.2.5 Effects of Modified Velocity

The original aerodynamics model (Sane and Dickinson, 2002) made the assumption that $\boldsymbol{v}^G$ and $\boldsymbol{v}_\omega$ were both negligible in comparison to the flapping velocity $\boldsymbol{v}_\phi$, The inclusion of the additional components formulated as a modification of the wing's 2D angle of attack and local wing frame velocity forms the basis for the dipteran flapping wing dynamics analysis.

3.2.5.1 Angle of Attack Modification

The local velocity components have a marked effect on the local angle of attack on each wing's airfoil section. The change in the 2D angle of attack may be written as

$$\alpha_{\text{add}} = \arctan\left(\frac{v_z}{v_x}\right). \tag{3.14}$$

The effect of the angle of attack modification is shown graphically in Fig. 3.5a and 3.5b, which demonstrates that an imposed (positive) heave velocity (descent) in 3.5b corresponds to an increase in angle of attack of the wings and corresponding increase in lift acting to oppose the motion, while the converse is also true. Then, heave velocity damping is found by consideration of the perturbation velocities, in much the same manner as flapping countertorque provides yaw damping via differential velocities.

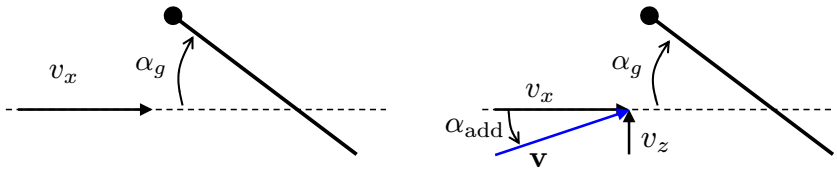

(a) Hover (b) Descent

Figure 3.5: Wing angle of attack is increased in a descent perturbation and reduced in a climb perturbation, so a flapping wing system in axial climb/descent exhibits damping in heave velocity w.

3.2.5.2 Effect on Dynamic Pressure

Modification of velocity components also affect the dynamic pressure $\frac{1}{2}\rho \boldsymbol{v}^2$ at each location. For example, any forward speed u results in an increase in dynamic pressure during the advancing stroke and a movement outboard of the location of zero dynamic pressure during the retreating stroke. Moreover, the wing component velocities are functions of both r and ϕ and consequently this spanwise location shifts throughout the wingstroke.

The total dynamic pressure under addition of velocity components is

$$q_{\text{total}} = \frac{1}{2}\rho \left(v_x^2 + v_y^2 + v_z^2\right). \tag{3.15}$$

For the flight conditions of many dipteran insects (Vogel, 1967), the dynamic pressure in eqn (3.15) is dramatically affected, up to several times the nominal dynamic pressure calculated using the wing kinematics, while the angle of attack as calculated by eqn (3.14) is affected by several degrees.

3.2.6 Perturbation Equations

Having found trim conditions, one may subtract eqn (3.10) from eqn (3.9) and solve for $\Delta\dot{u}$ to obtain

$$\Delta\dot{u} = \frac{\Delta X}{m} - g\cos(\theta_0)\Delta\theta, \tag{3.16}$$

where ΔX has the physical interpretation of being the perturbation force due to state or control perturbations from equilibrium (trim) values.

For traditional linearized analysis, a control model is developed by separating out the linear effects of each of the longitudinal variables u, w, θ, q, as

$$\frac{\Delta X}{m} = X_u\Delta u + X_w\Delta w + X_\theta\Delta\theta + X_q\Delta_q + \frac{X_c}{m}, \tag{3.17}$$

where $X_{[\cdot]}$ is defined to be $X_{[\cdot]} = \frac{1}{m}\frac{\partial X}{\partial[\cdot]}$. Similarly, the control term X_c may be expressed in terms of each of the input controls as

$$\frac{\Delta X_c}{m} = X_f\Delta f + X_\beta\Delta\beta + X_{\phi_{\text{off}}}\Delta\phi_{\text{off}}\ . \tag{3.18}$$

By expressing the perturbation forces in the form, a (time-invariant) linear system can now be written in standard state space form $\dot{\boldsymbol{x}} = A\boldsymbol{x} + B\boldsymbol{u}$ where $\boldsymbol{x} =$

$[\ \Delta u \quad \Delta w \quad \Delta q \quad \Delta\theta\ ]^T$, $\boldsymbol{u} = [\ \Delta f \quad \Delta\Phi \quad \Delta\beta \quad \Delta\phi_{\text{off}}\ ]^T$, and

$$A = \begin{bmatrix} X_u & 0 & 0 & -g \\ Z_u & Z_w & 0 & 0 \\ M_u & M_w & M_q & 0 \\ 0 & 0 & 1 & 0 \end{bmatrix}, \quad B = \begin{bmatrix} 0 & 0 & X_\beta & X_{\phi,\text{off}} \\ Z_f & Z_\Phi & 0 & 0 \\ 0 & 0 & M_\beta & M_{\phi,\text{off}} \\ 0 & 0 & 0 & 0 \end{bmatrix}. \tag{3.19}$$

3.2.7 Homogeneous System Dynamics (the A matrix)

Basic dynamics analysis begins with the unforced differential equation $\dot{\boldsymbol{x}} = A\boldsymbol{x}$. Without consideration of the perturbation velocities, differentiation with respect to u, w, and q of the effective X term yields that the stability terms X_u, X_w, and X_q are identically zero for any flight configuration because the wing's lift and drag components are functions of the kinematics, wing shape, and environment, not the state variables. All higher derivatives also do not contain any dependence on the state variables so the conclusion is not limited to a linear analysis. The experimental aerodynamics model in absence of perturbation velocities suggests that some form of feedback is necessary for an insect to possess stability, which would significantly increase the computational workload the insect must support.

3.2.8 Control Derivatives (the B matrix)

The insect aerodynamic forces and moments at hover equilibrium depend explicitly on the wing kinematic functions, so the control derivative estimates may

be found analytically. Intuitively, for perturbations about the nominal hover case $\theta_0 = 0$, the magnitude of the lift vector (via Δf or $\Delta\Phi$) does not affect the X force while a change in direction of the lift vector via $\Delta\beta$ does. Mathematically: as the X aerodynamic force contains a $\sin\beta_0$ term and $\beta_0 = 0$ for the hovering insect, the $\dot{u}$ equation has a nonzero X_β term shown in eqn (3.20), which evaluates to g because Z force equilibrium for the trim condition has already specified that the nominal value of the lift vector must be $Z = -W = -mgc_{\theta_0}$, and $X_\beta = \frac{1}{m}\frac{\partial X}{\partial \beta}$, where $c_{\theta_0} = \cos\theta$ and $s_{\theta_0} = \sin\theta$.

$$\begin{aligned} X_\beta &= \frac{1}{m}\frac{\partial}{\partial\beta}\left[2\pi^2\rho(\hat{r}_2^2 SR^2)(f^2\Phi^2\sin\beta)C_{L,avg}\right] \\ &= \frac{2\pi^2\rho(\hat{r}_2^2 SR^2)(f_0^2\Phi_0^2)C_{L,avg}}{m} = gc_{\theta_0} \end{aligned} \tag{3.20}$$

3.2.8.1 Heave and Pitch Dynamics

The derivation has focused on the $\hat{s}_x$ axis, but the heave $\hat{s}_z$ and pitch θ dynamics parallel the $\hat{s}_x$ results. The control input matrix B found by this method is shown in eqn (3.21), where the nominal integral lift L_0 has been defined in eqn (3.22).

$$B = \begin{bmatrix} 2g\frac{c_{\theta_0}}{f_0}\tan(\beta_0) & 2g\frac{c_{\theta_0}}{\Phi_0}\tan(\beta_0) & gc_{\theta_0} & 0 \\ -2g\frac{c_{\theta_0}}{f_0} & -2g\frac{c_{\theta_0}}{\Phi_0} & gc_{\theta_0}\tan(\beta_0) & 0 \\ 0 & 0 & \frac{2}{I_{yy}}L_0\, d_z & \frac{2}{I_{yy}}L_0\cos\left[\sin^{-1}(\frac{-d_x}{r_a})\right] \\ 0 & 0 & 0 & 0 \end{bmatrix} \tag{3.21}$$

$$L_0 = \pi^2(\hat{r}_2^2 SR^2)(f_0^2\Phi_0^2)C_l \tag{3.22}$$

For the biologically-motivated choice of a level stroke plane angle $\beta_0 = 0$ and hovering at $\theta_0 = 0$, eqn (3.21) can be simplifed to

$$B = \begin{bmatrix} 0 & 0 & g & 0 \\ \frac{-2g}{f_0} & \frac{-2g}{\Phi_0} & 0 & 0 \\ 0 & 0 & \frac{2}{I_{yy}} L_0 d_z & \frac{2}{I_{yy}} L_0 \cos\left[\sin^{-1}(\frac{-d_x}{r_a})\right] \\ 0 & 0 & 0 & 0 \end{bmatrix}. \tag{3.23}$$

3.2.8.2 Significance of the Control Matrix B

The control matrix B provides direct insight into the physics of how control inputs affect insect flight motion. In particular, the control matrix exhibits a decoupling which both suggests a means of control and is consistent with the biological intuition formed by dipteran insect observations.

The first row implies that an insect in hover uses its stroke plane angle to modulate its fore/aft movements, necessitating a coupled adjustment in the input ϕ_{off} to maintain equilibrium. This coupled behavior is exactly as observed in free flight insects (Taylor, 2001). Moreover, by appropriate choice of wing length, the insect may lose the use of the input ϕ_{off}. Initially it appears that extending/trimming an insect's wings (to affect r_a) could force an insect to hover at a differing pitch angle and that the insect would lose the ability to generate pitch moments at a particular wing length. However, since r_a is normally several times larger than d_x, the insect's wings would have to be drastically shortened to achieve the $d_x = r_a$ condition and the lift generated by the trimmed wings would be severely impaired before the

capability to generate pitch moments is destroyed.

Forward Velocity u: The control affecting the forward velocity u is the inclination of the stroke plane angle, suggesting a "helicopter-like" mode of regulating forward velocity is physically reasonable. The X_β term reflects inclination of the lift vector–the g term is related to the trim input solution for equilibrium in hover. Note there is some cross-coupling into the pitch rate via nonzero M_β.

Heave velocity w: A hovering insect has at least two means of controlling its vertical velocity w, both of which are related to changing the magnitude of the lift vector: wingbeat frequency f and flap amplitude Φ. Both of these terms enter in a complementary fashion, and show the expected effect: an increase in frequency or amplitude causes the insect to rise.

Pitch angle θ: No direct control over the pitch axis is provided; instead control of the pitch is through integration of the pitch rate, as a direct consequence of Eulerian mechanics.

Pitch Rate q: Pitch rate is primarily controlled by the offset (mean) term in the harmonic flap function. As expected, deflecting the mean position of the wings forward results in a positive (nose-up) pitch rate. Moreover, the strength of the term is related to the ratio of the distance along the $\hat{\boldsymbol{s}}_x$ from thorax to the center of mass as compared to the wing length R. Among other things, this provides a means to immediately estimate via a photograph the pitch control authority a particular insect has, much like a fixed-wing aircraft's wing loading gives an immediate means to estimate its velocity. The simple insect pitch control estimate is particularly useful for small insects where characterizing the insect's pitch inertia is difficult. Pitch

rate is also secondarily controlled by the stroke plane angle term which primarily generates a response in the forward velocity, so the offset term is an appropriate choice for controlling pitch rate and is a trend observed in nature (Taylor, 2001).

3.3 Simulation and System Identification

In this section, a simulator is created using the perturbation velocities aerodynamics model developed in Section 3.2 and a frequency-based model parameter identification approach for a simulated insect parameters described.

3.3.1 Simulation

A simulation environment seen in Fig. 3.6 has been created including the aerodynamics model developed in Section 3.2 and the 6 degree-of-freedom rigid body equations of motion (the longitudinal portions of which are seen in eqn (3.8a) to eqn (3.8c)) in order to capture the most essential rigid body motion of the insect forced by translational lift dynamics. The aerodynamic model was derived using *Drosophila* data, so the simulator is populated with parameters from this species. Wing mass is an order of magnitude smaller than body mass, and research by Sun and Xiong (2005) and Taylor and Thomas (2003c) has indicated that the effects of high-frequency wing mass oscillations are small. Accordingly, the simulator represents the inertial properties of the overall insect by the insects body mass and inertia tensor matrix, and body forces with a constant gravitational field and traditional aerodynamics modeling (Full and Koehl, 1992).

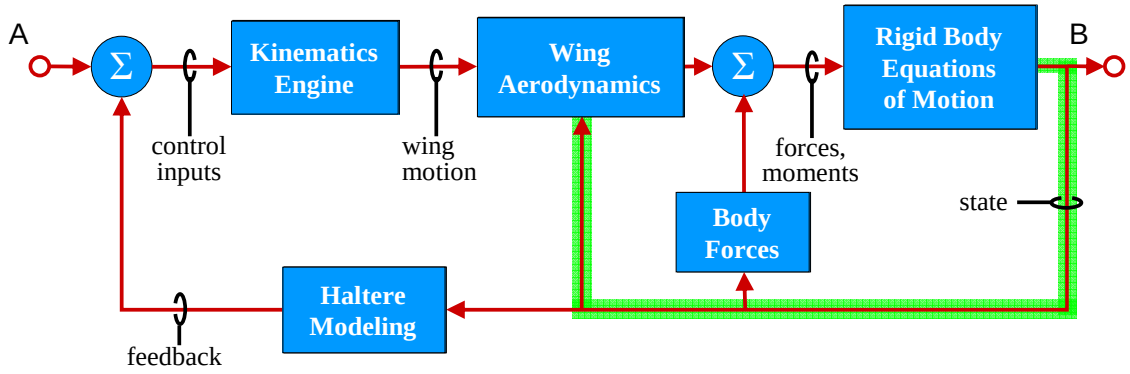

Figure 3.6: Simulator used for haltere-on and bare-airframe input/output studies, showing (highlighted path) the critical modification: consideration of rigid body state in wing aerodynamics functions.

The simulation includes synthesis of physically realistic wing kinematics trajectories, using the bio-inspired analytic expressions presented earlier to solve for the position of a wing at simulation time. The kinematics engine's bio-inspired parameters are then viewed as the control inputs and used to drive the insect motion as desired.

The wing used in the simulation is a symmetric planar wing with a planform characterized nondimensionally via a second-order shape model. The use of such a wing is justified analytically and by reference to experimental data and high-speed imagery (Fry et al., 2003). (Flexibility effects in the species studied are an active area of research and not included in the simulation at this time but will be included when significant results appear.)

3.3.1.1 Haltere Modeling

Experimental evidence has repeatedly demonstrated that components of the insect's control system, particularly the portions concerning vision, do not have

bandwidths that would allow them to actively stabilize high-frequency behavior arising from the wing. Instead, the higher frequency angular rate loops have been closed using haltere-based rate feedback. Halteres are a pair of oscillating aerodynamically-ineffective "hind wings" that have been shown to be theoretically (Thompson et al., 2008) and experimentally (Derham, 1714; G Nalbach, 1993) capable of acting as a biological rate gyro (Nalbach, 1994). Previous work has characterized the haltere frequency response patterns in both equilibrium (Sherman and Dickinson, 2003) and aggressive flight motions known as saccades (Bender and Dickinson, 2006a) and shown that they can be modeled as bandpass filters with their outputs summed with visual feedback (Sherman and Dickinson, 2004; Bender and Dickinson, 2006b). In the simulation, simple bandpass filters on the angular rates are used in a feedback loop to model the haltere angular rate feedback

3.3.2 System identification method

We would like to characterize the rigid body motions about hover in a model amenable to control analysis and design tools. In this section, we present a frequency-based linear system identification that was conducted on the simulation using Comprehensive Identification from FrEquency Responses (CIFER) (developed by NASA-Ames (Tischler, 1992)). Frequency-based system identification identifies a system model only over a range of frequencies so care must be taken to select the frequencies that are relevant for the desired application. The desired application is understanding sensing and feedback requirements for flight control design, so capturing the

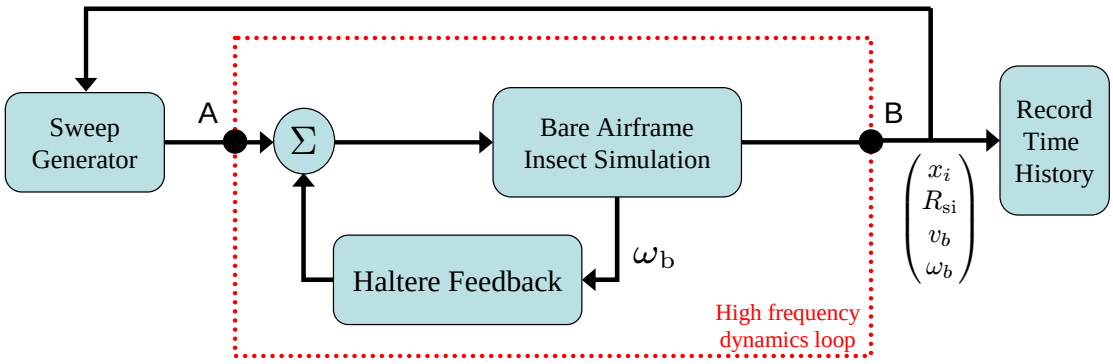

Figure 3.7: This study considered the haltere-stabilized insect mapping inputs at point A to outputs at point B. A low gain controller was included that modified the frequency sweep inputs to keep the system near hover.

basic rigid body motions (i.e., up to ∼20Hz) is desired. The haltere-on airframe motion was the primary system to be identified, or the high frequency system in Fig. 3.7 (shown in a dashed box) with inputs taken at point A and outputs taken at point B. The identification procedure for the haltere-on system via simulations conducted with the controller and mechanosensory feedback running was designed by considering the haltere feedback as a stability augmentation system (SAS). By considering the halteres as a SAS system, procedures for bare-airframe identification from SAS-on flight tests (Tischler and Cauffman, 1999) could be used. In most simulated flight test cases, open loop design of the frequency sweeps was sufficient to keep the insect near hover, but a low-gain external feedback loop was used primarily for haltere-off (bare airframe) identifications, where the controller-modified frequency sweeps were considered as the input.

With a flap frequency of approximately 200 Hz (1256 rad/s), *Drosophila* have dynamic motions at such frequencies. Obviously, wing motion predominates at this frequency, but in a simulation with little or no viscous damping effects on the

body, small body motions can be observed, relating to the force dependence on this flap frequency. In particular, the flap frequency and potentially higher order harmonics of it (2/flap, 3/flap, and so on) appear in the state history output. The movement of the center of pressure fore and aft generates a pitching moment that leads to oscillatory behavior. The addition of rotational damping could partially mitigate this effect, but the smaller oscillatory motions observed at these frequencies elicit haltere responses since the vision-based control system response trails off at high angular rates. Significant statistical correlations from input to output was not observed above approximately 30 Hz (188rad/s) and frequency responses above 90 Hz were discarded. Limiting the frequencies identified has the advantage of removing the high frequency noise and numerical artifacts during the identification process.

Low frequency identification is limited by the length of the time history presented. In theory, the lowest frequency that could be identified in a time history of length $T_{\max}$ is $f_{\min} = 1/(2T_{\max})$. In practice, accurate identification requires several cycles of the longest mode. All expected or observed frequencies were faster than the lowest possible frequency in the 14 second (2800 wingbeat) trials used in this study: $f_{\min} = 0.04$Hz (0.22 rad/s). Instead, based on observed modes and numerical capability, the search for a model was restricted to above 0.1 Hz (0.6 rad/s).

3.3.3 Model structure

In consideration of linearized longitudinal dynamics about hover, a traditional flight dynamics model takes the form $\dot{\boldsymbol{x}} = A\boldsymbol{x} + B\boldsymbol{u}$ (Franklin, 2002), where A and

B are most generally defined as in eqn (3.19). Applied to a helicopter or fixed-wing airplane, several of the terms in the A matrix are zero. For example, the term M_w may usually be discarded in hover. In forward flight, linearization of the disc angle of attack shows that M_w is related to the body angle of attack via the forward velocity u_0 and may not be discarded.

3.4 Discussion

3.4.1 Non-Parametric Handling Qualities Identification

One way to characterize the control requirements of the haltere-on airframe dynamics is from the perspective of a human tasked with piloting the vehicle, since determing the computational capabilities of the insect not yet established. Several metrics pertinent to human-piloted rotorcraft small-perturbation handling qualities analysis have been quantified and evaluated from calculated frequency responses shown in Fig 3.8-3.11 without the need for a state-space model. Table 3.3 shows the properties important for control and handling qualities evaluation, from which it is clear that the pitch and heave dynamics have higher bandwidths than the fore/aft dynamics. As specified in ADS-33 (US Handling Qualities Requirements for Rotorcraft), a gain margin of 6dB and phase margin of 45° was used to calculate the bandwidths (Aviation Engineering Directorate, 2000). Care must be exercised in interpreting the gain and phase margins as the calculation of several of these items involves frequencies beyond the range of good coherence.

ADS 33 specifies a number of maneuvers known as mission task elements

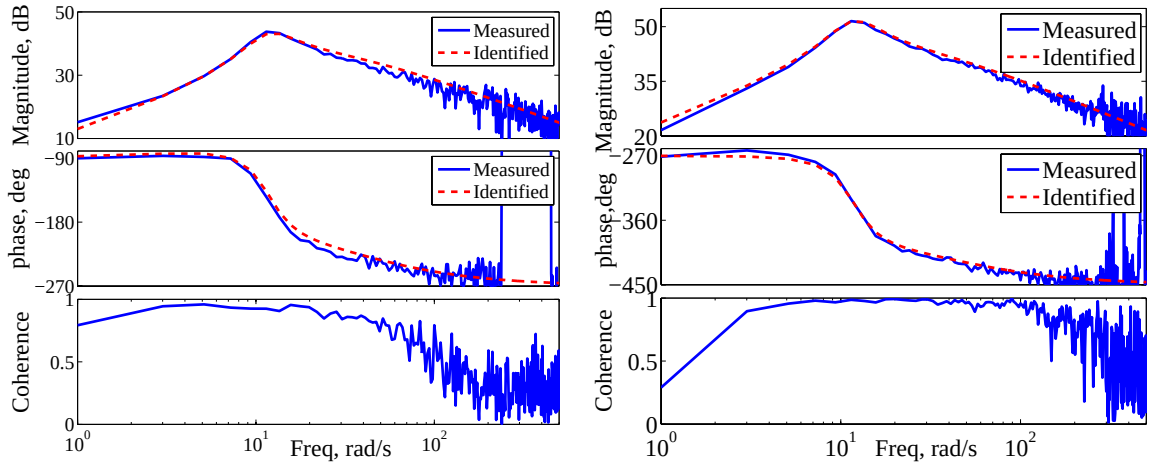

(a) Stroke plane angle β to q

(b) Stroke offset ϕ_{off} to q

Figure 3.8: Identified transfer functions to pitch rate q.

(MTEs) for which the helicopter is evaluated. With respect to pitch control, the relatively high bandwidth (compared with full scale rotorcraft) of the system means ADS-33 meets Level 1 handling qualities requirements for the hover and low speed small amplitude pitch-related MTEs, including target acquisition and tracking. However, were the insect airframe to be humanly piloted, the indeterminate gain bandwidth values are a cause for concern because they indicate a susceptibility to pilot-induced-oscillation. With respect to forward motion, recall that β was recommended as fore/aft control. In general, forward speed regulation is shown to be the slower bandwidth output, which is likely related to the fact that fore/aft motion is primarily accomplished by tilting the insect's thrust vector, followed by its body. Such a behavior is analogous to a helicopter tilting its rotor disc, followed by its fuselage, and is slower than other dynamics modes.

Experimental evidence indicates that an insect's neural structure responds with a small time delay, about 3-4ms (Autrum, 1958), and a detailed model of wing

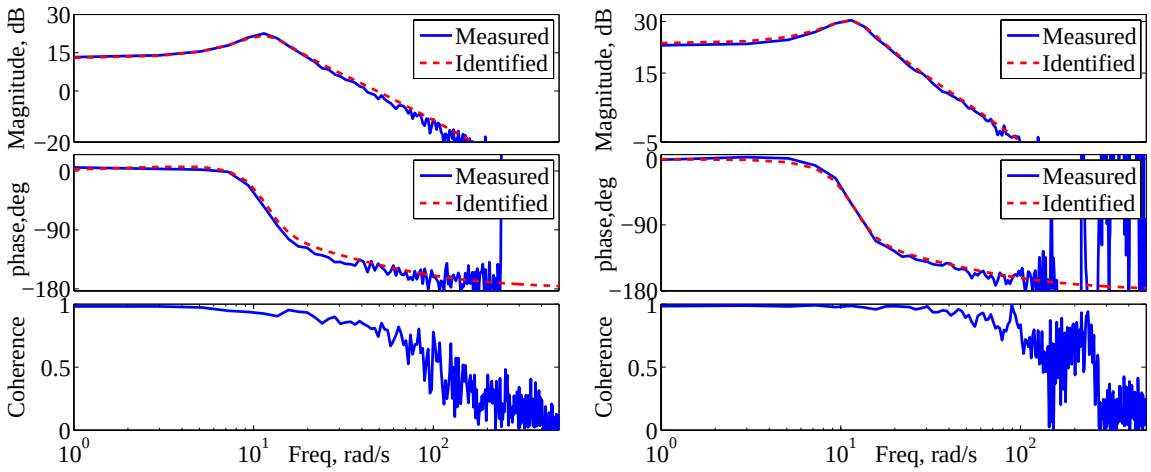

(a) Stroke plane angle β to θ

(b) Stroke offset ϕ_{off} to θ

Figure 3.9: Identified transfer functions to pitch angle θ.

structural dynamics could add an additional delay. While the low phase margin in the primary β to u transfer function suggests that introducing a time delay on the order of 5-10ms could affect the stability of the system, the coherence in this frequency range is degraded and further investigation is necessary.

Function	GM	PM	Gain BW	Phase BW	Delay
β to θ	∞	37°	∞	6.2Hz	0
ϕ_{off} to θ	∞	23°	∞	4.5Hz	0
Φ to w	∞	106°	∞	∞	0
β to u	5dB	4°	3.5Hz	2.2Hz	n/a
ϕ_{off} to u	∞	36°	2.2Hz	2.2Hz	18 ms

Table 3.3: Control and handling qualities properties used to evaluate the system in reference to rotorcraft handling qualities requirements. GM and PM represent gain and phase margins, resctively.

3.4.2 Heave Dynamics

By observation that axial flight testing is decoupled from the other inputs, the system was modeled as a 1D system representing the heave dynamics and a system

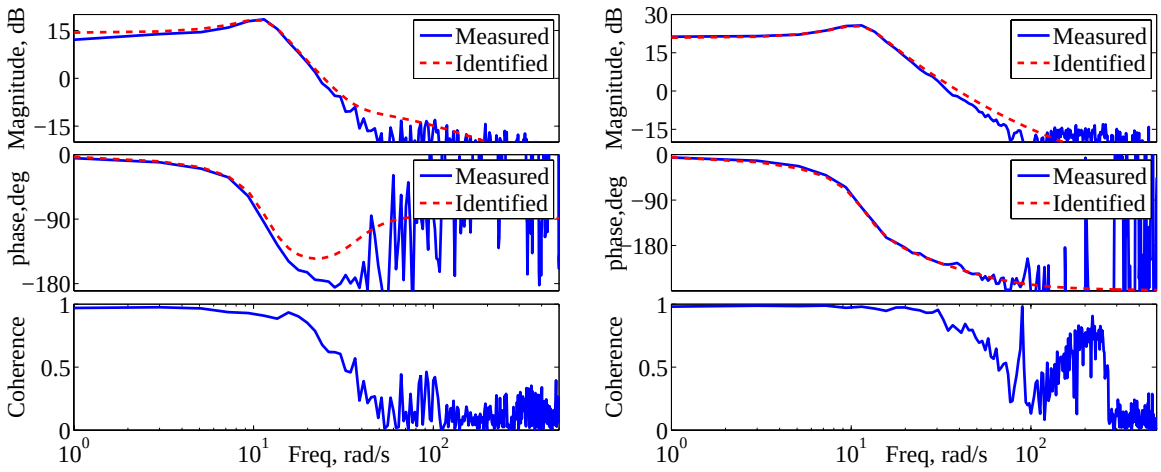

(a) Stroke plane angle β to u

(b) Stroke offsetϕ_{off} to u

Figure 3.10: Identified transfer functions to forward velocity u.

in $\mathbb{R}^3$ and the heave dynamics identified first in standalone axial simulations. For an insect in hover at some pitch angle θ_0, with an equilibrium stroke plane angle of β_0, vertical force equilibrium provided a means to solve for vertical trim and a corresponding heave model of the form

$$\dot{w} = Z_w w + Z_f(f - f_0) + Z_\Phi(\Phi - \Phi_0) + Z_\beta(\beta - \beta_0) + Z_{\phi_{\text{off}}}(\phi_{\text{off}} - \phi_{\text{off},0}). \quad (3.24)$$

Analytic linearization of the quasi-steady form yielded an expression for the terms in the B matrix,

$$B = \begin{bmatrix} \frac{-2g\cos\theta_0}{f_0} & \frac{-2g\cos\theta_0}{\Phi_0} & g\tan\beta_0\cos\theta_0 & 0 \end{bmatrix}. \quad (3.25)$$

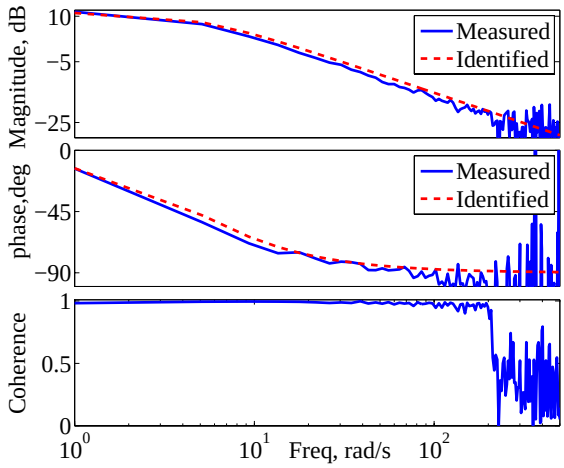

Figure 3.11: Identified transfer function from stroke amplitude Φ to heave velocity w.

For the example *Drosophila*-like insect, the numerical evaluation of the B matrix using the trim parameters shown in Table (3.4) yields

$$B = \begin{bmatrix} -0.098 & -14.584 & 0 & 0 \end{bmatrix}. \tag{3.26}$$

control input	value
f_0	200 Hz
Φ_0	77.08°
β_0	0°
ξ	90°
r_a	1.6mm

Table 3.4: Nominal input parameters used in evaluating B for the hover linearization.

Frequency-based system identification of the heave dynamics under excitation via modulating the flapping amplitude Φ by 1 degree about the nominal (trim) value Φ yields

$$\dot{w} = [-4.862]w + [-17.1941]\Delta\Phi. \tag{3.27}$$

Visible in eqn (3.27) is an aerodynamic damping term Z_w which is of aerodynamic origin and was predicted due to the modified angle of attack due to the perturbation velocities. (See Fig (3.5) for a physical explanation of this effect.) A simulation without consideration of perturbation velocities does not exhibit positive Z_w damping, indicating the effect is due to the modification.

3.4.2.1 Effect of Flap Amplitude

The identified system in eqn (3.27) includes a control term reflecting the fact that heave control in hover is achieved through direct modulation of the aerodynamic thrust. Experimental evidence indicates that insects do have the capability to measure angular rates and they respond to a mechanical disturbance in pitch rate with a change in stroke plane amplitude $\Delta\Phi$ and stroke offset ϕ_{off} that is nearly linear (Thompson et al., 2008). It is theorized that at high angular rates the amplitude response falls off, but physical limitations mean measurements have not yet been conducted involving a disturbance faster than approximately 800°/s to verify this conclusion. For this reason, the nonlinear simulation models a high frequency cutoff on hatere rate feedback.

3.4.2.2 Effect of Flap Frequency

In contrast to flap amplitude, an insect's flap frequency response to a pitch rate is not a linear relationship and there is dispute over how insects use flap frequency as an input. In the linear analysis presented earlier, flap frequency enters in the

same functional manner as flap amplitude, but insects often choose to modulate wingbeat frequency independently of the wingbeat amplitude, commonly varying it in conjunction with other control inputs (Dudley, 1995) (Altshuler et al., 2005) (Vance et al., 2005) . Experimental work has indicated that the dependence of lift on Φ is linear and nearly quadratic on f, but insects decrease flap frequency when approaching peak force outputs. The response exhibits a maximum near 200°/s, and *decreases* as the angular rate increases from that point (Sherman and Dickinson, 2003), which is presumed to be a physiological limitation (Taylor, 2001).

The frequency ranges appropriate for a linear system model are determined by reference to the coherence $\gamma \in [0, 1]$ of the input/output pair, which quantifies the degree to which an input-output pair are related by linear system dynamics. Coherence is defined via

$$\gamma(\omega) = \frac{|G_{xy}(\omega)|^2}{G_{xx}(\omega)G_{yy}(\omega)} , \tag{3.28}$$

where 1 indicates entirely linear system dynamics and 0 indicates an input/output pair with no linear correlation. For the stroke plane amplitude to heave relation, the frequency band of linearity covers much of the range of frequencies expected in an insect control problem. Conversely, the frequency range of acceptable coherence in the flap frequency to heave velocity relation is limited to the higher frequency regions shown in Fig. 3.13. The reduction in linear effectiveness for stroke plane amplitude modulation (indicated by the negative slope in the Bode magnitude plot) and the complementary increase in flap frequency modulation linear effectiveness (indicated by the coherence increase from 0 to near 1 and the positive slope in the

Bode magnitude plot) may explain why insects tend to use frequency and amplitude in a different manner. A complementary set of control inputs mirrors a paradigm observed in insect vision sensing, where visual and mechanical (haltere) feedback mechanisms cover differing portions of the frequency spectrum. Complementary actuation dynamics are often observed in nature, but this means that a transfer function fit that includes both control inputs is a compromise between accuracy of the two.

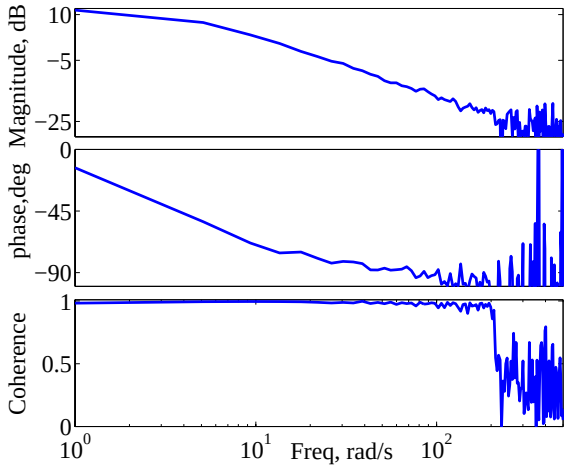

Figure 3.12: As noted in experimental observations of insects, stroke plane amplitude Φ shows a linear correlation to perturbations.

The input controls were chosen based on biological observations, but the limited flap frequency band of acceptable coherence restricts its linear application to relatively fast inputs. Any vehicle, including biological structures, must also be designed for optimal operation at or near a particular frequency, limiting the ability to use flap frequency as a control term. For these reasons, flap frequency is not recommended as a primary control term but is included in this study to illustrate its complementary control effect. Under the restriction of high frequency excitation,

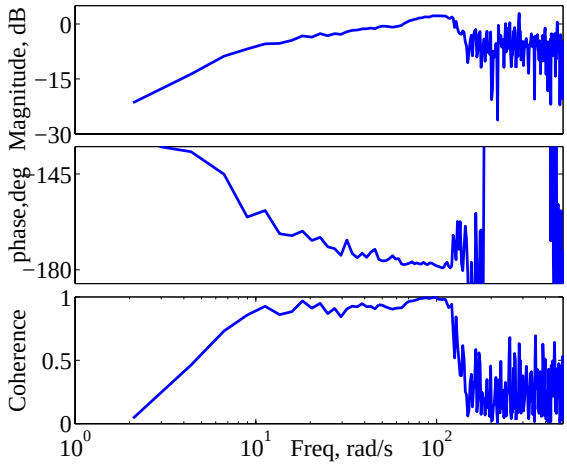

Figure 3.13: The use of flap frequency f as an input is correlated linearly over a smaller region than Φ.

the system can be re-identified including the effect of the control input f. During this identification, the Z_Φ term was fixed to the analytic result and the system was determined to be

$$\dot{w} = [-4.7888]\, w + \begin{bmatrix} -114.4228 & -14.584 \end{bmatrix} \begin{bmatrix} f \\ \\ \Phi \end{bmatrix}. \tag{3.29}$$

Such a system still shows acceptable fit from stroke amplitude to heave velocity, as seen in Fig. 3.14. A time domain comparison of the nonlinear and identified system appears later in Figure 3.15(b).

3.4.3 Longitudinal Dynamics

While the axial climb (heave) dynamics may be adequately described in isolation from the other state variables, an accurate description of the insect's motion along its $\hat{s}_x$ axis and pitch motion requires consideration of the coupled system. In

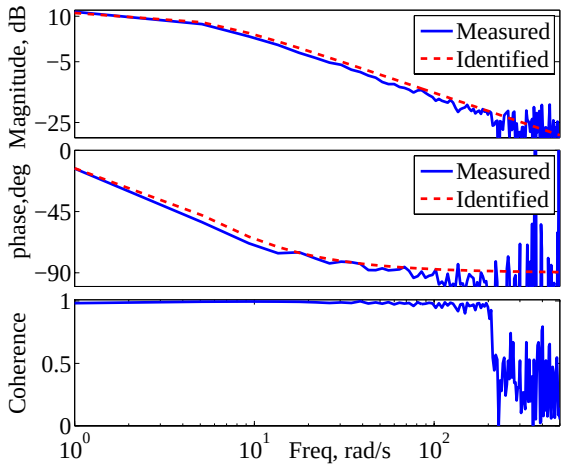

Figure 3.14: The identified system fits the stroke plane amplitude to heave velocity relation.

this section, system identification tools are used to reduce the nonlinear *Drosophila*-like dynamics in θ, u, and q to a linearized system (about hover) that may be directly applied to control design.

For the system identification, simulated flight tests were conducted including frequency sweeps applied to each of the channels in turn with off-axis controller portions turned off (or the entire controller off) to prevent cross-correlated inputs that can interfere with identification. Frequency as an input was discarded for the reasons discussed earlier.

The identified longitudinal system dynamics matrix for the haltere-on system

is identified to be

$$A_{\text{id}} = \begin{bmatrix} -12.33 & 0 & 0 & -9.810 \\ 0.0 & -4.651 & 0 & 0 \\ 547.0 & 0.0 & -33.26 & 0 \\ 0 & 0 & 1 & 0 \end{bmatrix}. \tag{3.30}$$

The system dynamics matrix A_{id} has the eigenvalues $\lambda_1 = -38.56$, $\lambda_{2,3} = -3.51 \pm 11.26i$, $\lambda_4 = -4.65$, and the eigenvectors seen in eqn (3.31), confirming the observation that the heave dynamics are uncoupled from the pitch/translational dynamics.

$$\nu_1 = \begin{bmatrix} -.0097 \\ 0 \\ .9996 \\ -.0259 \end{bmatrix}, \quad \nu_{2,3} = \begin{bmatrix} 0.0578 \angle \pm 0.3619 \\ 0 \\ 0.9948 \\ 0.0843 \angle \mp 1.8730 \end{bmatrix}, \quad \nu_4 = \begin{bmatrix} 0 \\ 1 \\ 0 \\ 0 \end{bmatrix} \tag{3.31}$$

The control input matrix is identified to be

$$B_{\text{id}} = \begin{bmatrix} 0 & 20.67 & 12.69 \\ -17.36 & 0 & 0 \\ 0 & -2826.0 & 6020.0 \\ 0 & 0 & 0 \end{bmatrix}. \tag{3.32}$$

Each of A_{id}'s diagonal elements (X_u, Z_w, and M_q) are negative, indicating

viscous damping along/about that axis. Thus, the experimentally-derived aerodynamics model applied to rigid body dynamics predicts viscous damping in the absence of body drag forces, i.e., as a fundamental part of flapping wing flight. Such a passive stabilization mechanism is highly advantageous for reducing the computational and energetic workload, and parallels the recent work characterizing "flapping counter-torque" (Hedrick et al., 2009), or damping about the $\hat{s}_z$ axis.

3.4.3.1 Pitch Dynamics

The most relevant stability derivatives for pitch dynamics are M_β, $M_{\phi_{\text{off}}}$, and M_q. A single axis pitch dynamics model involving these terms can help illustrate the role of the pitch stiffness and control terms. For the linear system, apply the principle of superposition to write the pitch rate output as the sum of two SISO systems with step inputs applied to β and ϕ_{off} such that

$$q(t) = (1 - e^{M_q t}) \left[\frac{-M_\beta}{M_q} \Delta\beta + \frac{-M_{\phi_{\text{off}}}}{M_q} \Delta\phi_{\text{off}} \right]. \tag{3.33}$$

Much of helicopter handling qualities analysis and control design is focused on increasing the magnitude of M_q, because M_q describes the rate at which a pitch rate reaches a steady-state value for a given step input, or the "quickness" of the vehicle's pitch response to a pilot input. A major advantage of a modern "hingeless" rotor design is the resulting larger bare airframe $|M_q|$, from about 0.5 for a UH-60 to 5-6 for an aerobatic Bo-105 (Heffley et al., 1979b). The addition of a flight control system increases $|M_q|$ and is desired for a UH-60 to maintain a reasonable

pilot workload. The estimation of $M_q = -33.3$ indicates that the insect pitch response is largely kinematic rather than dynamic. Such a finding implies that mechanosensory feedback mechanisms can markedly reduce the neural demands of insect flight control, which may help explain how insects are able to achieve high levels of maneuverability on a very small computational budget.

The control terms M_β and $M_{\phi_{\text{off}}}$ affect the magnitude of the steady-state pitch rate reached for a given input. A relative comparison of the two derivatives shows that a perturbation in the ϕ_{off} input is more than twice as effective at creating a pitch rate. This fact, coupled with the fact that the input β also leads to a forward speed response twice the size of a ϕ_{off} input, verifies the theoretical conclusion that ϕ_{off} is the appropriate primary control term for pitch dynamics. Direct comparison of analytic versus identified $M_{\phi_{\text{off}}}$ is complicated high sensitivity to parameter variations in the estimated term r_a, but M_β has the analytical estimate (using the r_a approximation) -4660, as compared to the identified value -2826.

The pitch response to forward speed defined by M_u is an important result, as it leads to a nose-up motion in the presence of a forward velocity, and hence a restoring force to resist the increase in speed. $M_u > 0$ is a criteria for static stability. In a helicopter, a positive M_u is created by rotor blade excursions from the disc plane, but the positive M_u result indicated here was reached without providing the wings the ability to move out of the stroke plane defined by the input.

3.4.3.2 Forward and Heave Velocity Dynamics

The forward velocity dynamics are represented by the identified X_u, $X_{\phi_{\text{off}}}$, X_β and an additional inertial term formed by inclination of the gravity vector that remains $-g$ throughout this analysis. X_u indicates that flapping wing kinematics provide static speed stability even in the absence of body drag forces. The X_β control effectiveness term was estimated analytically as g but identified to be 20.7. The X_β and $X_{\phi_{\text{off}}}$ terms were the derivatives identified with the most uncertainty, with insensitivities of 3 and 5.5%, respectively, indicating that additional dynamic effects not considered in this analysis may be relevant for the description of this degree of freedom.

3.4.4 Identified Longitudinal Dynamics Verification

To verify the model structure used, additional candidate dependencies not included in the analytic model were included, such as Z_u and M_w and delays in the input channels to allow for unmodeled states. In all cases, the added terms were identified to zero, small, or had only minor effects on the transfer function and simulated time histories.

The responses of the identified and nonlinear systems to a variety of inputs were compared. The identified system shows tracking during parallel simulations, and a test involving simultaneous actuation in all input controls is shown in Fig. 3.15.

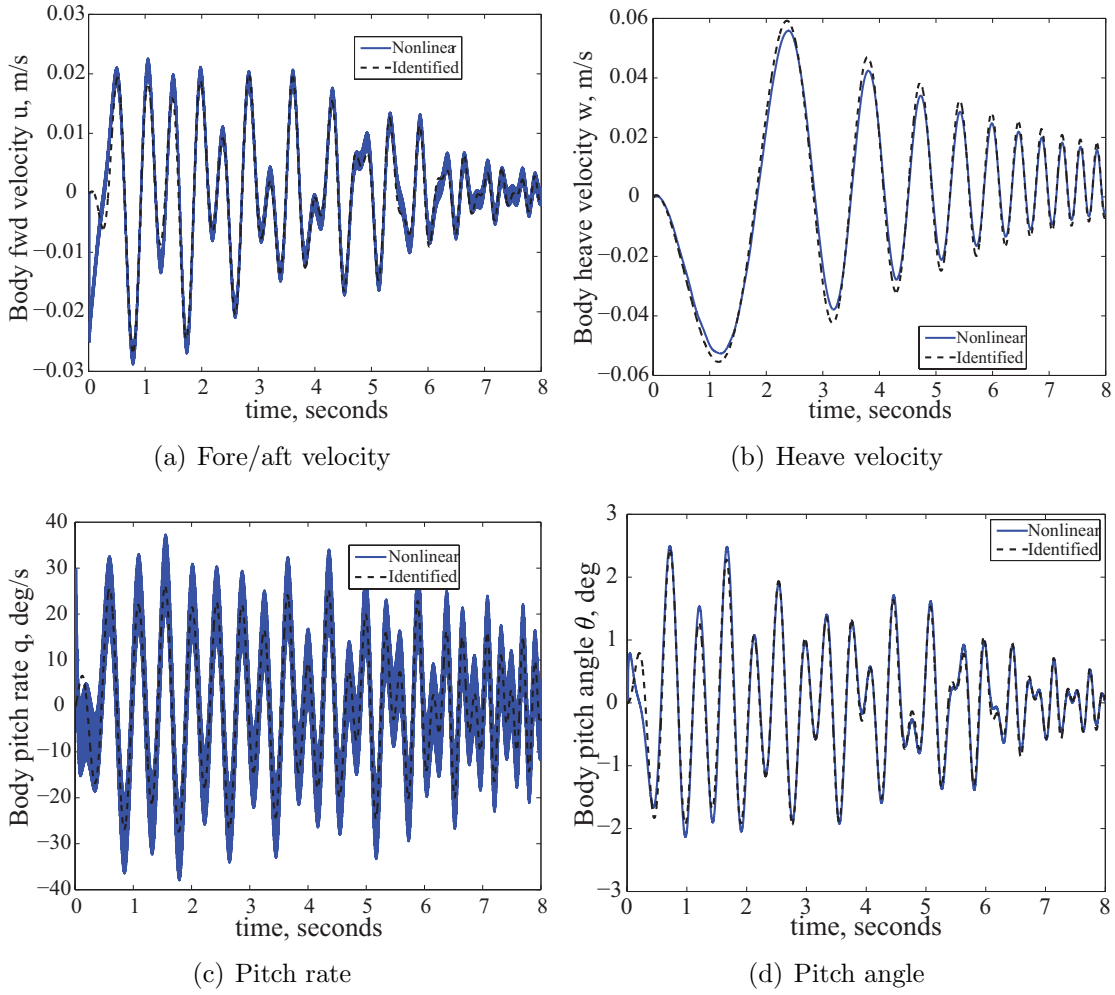

(a) Fore/aft velocity

(b) Heave velocity

(c) Pitch rate

(d) Pitch angle

Figure 3.15: Time domain comparison of the linear and nonlinear systems.

3.4.5 Accuracy of Identified Model

Besides evaluating the accuracy of the identified model via how well the identified and experimental transfer functions agree (see Figs 3.8-3.11) and through comparison of simulation results in section 3.4.4, the accuracy of the each of the parameters in the identified model may be estimated as part of the system identification procedure. One method for comparing the quality of identification of each parameter is via investigation of how variation in that parameter affects the global

Parameter	Value	Standard Dev. σ	Insensitivity
X_u	-12.3	4.0%	1.1%
Z_w	-4.7	9.1%	3.8%
M_u	547	3.6%	0.9%
M_q	-33.3	4.6%	1.1%
$X_{\phi_{\text{off}}}$	12.7	12.2%	5.9%
X_β	20.7	7.6%	3.0%
Z_Φ	-17.4	4.8%	2.0%
$M_{\phi_{\text{off}}}$	6028	3.6%	1.2%
M_β	-2826	3.8%	1.1%

Table 3.5: Uncertainty estimates for identified dynamics model.

cost function describing the difference of the transfer function fit and calculated frequency response, a relative estimate known as the "insensitivity." Values of insensitivity less that 10% are considered reasonable, and the identified values ranged from less than 1% for M_u to 5.9% for $X_{\phi_{\text{off}}}$. A good estimate of the standard deviation in each parameter to be expected in repeated flight tests and identification sequences may be determined through Cramer-Rao (CR) bounds. Table 3.5 shows uncertainty estimates for the estimated parameters, where the standard deviation upper bounds are derived from the lower bounds provided by CR bounds (Tischler and Cauffman, 1999). The uncertainty does not destroy the qualitatitive behavior of the eigenvalue map, shown in Fig. 3.16, which shows the presence of a fast and subsidence mode and an oscillatory pair. The slow subsidence mode associated with the smaller real root is the heave damping pole, while the other three reflect coupled motion of the pitch and fore/aft dynamics.

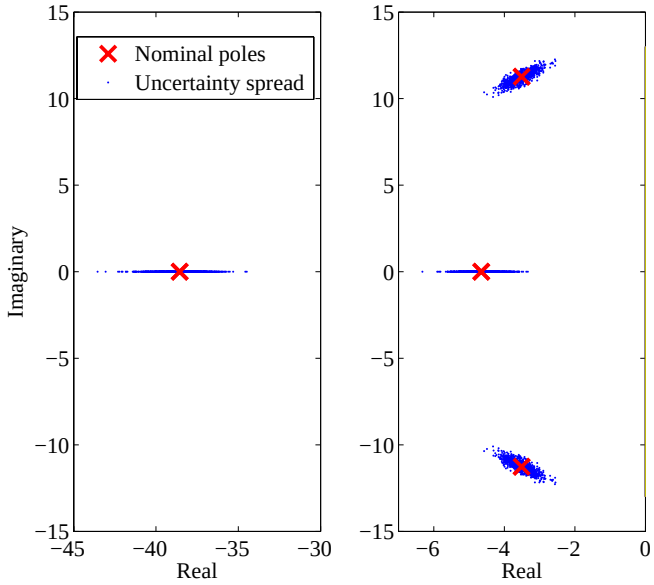

Figure 3.16: Map of haltere-on system poles with uncertainty perturbations as listed in Table (3.5) preserves the qualitative behavior.

3.4.6 Bare Airframe System Identification

An identification of the haltere-on system revealed a decoupled, stable system that indicated a control system would not need to provide stabilization feedback. Identification of the bare-airframe system may also be conducted, which reveals a decoupled heave pole, a fast subsidence mode, and an *unstable* oscillatory pair, as seen in Fig. 3.17. The finding that haltere-based rate damping is sufficient to stabilize the unstable oscillatory pair associated with pitch dynamics has experimental support (Fraenkel, 1939; Casas and Simpson, 2007). Since the oscillations are at approximately 2 Hz, the stability of the pair is important from the perspective of quantifying the control requirements–for example, an oscillatory instability at 2 Hz would be unacceptable for a human-piloted aircraft. The bare airframe pole structure seen in Fig. 3.17 is the most common pole structure associated with hovering

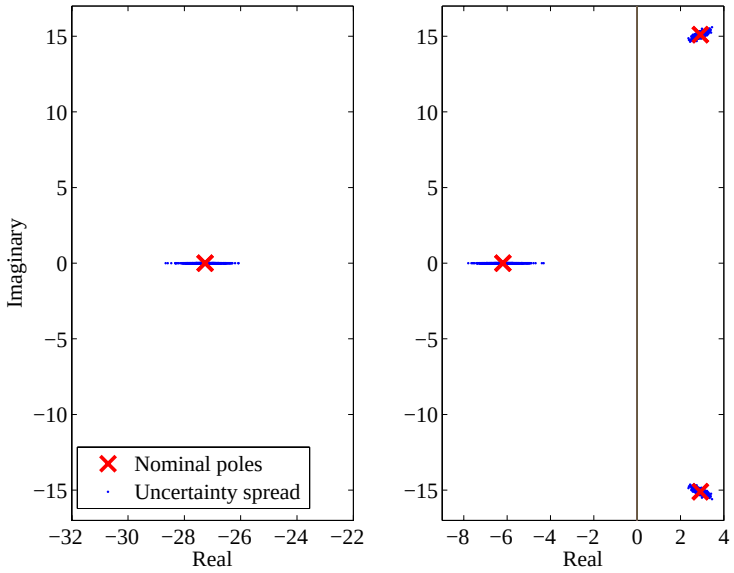

Figure 3.17: Map of haltere-off system (the bare-airframe) poles including uncertainty perturbations indicates the traditional VTOL modal structure (Sun and Xiong, 2005).

vertical takeoff and landing (VTOL) aircraft, including a hovering Harrier VTOL aircraft (Franklin, 2002), many helicopters which exhibit a lightly unstable Phugoid mode in hover (Heffley et al., 1979a,b), and the CFD-based analysis (Sun and Xiong, 2005) of a bumblebee. That the same pole structure results from complex computational fluid dynamics analysis and from a relatively simple application of curve-fitted aerodynamics to a rigid body simulation is significant, but the observation of the same pole structure across differing scales and vehicle configurations (rotorcraft, fixed wing VTOL, and dipteran flapping wing) is even more remarkable, because dynamic similarity of the two systems is not suggested by traditional scaling arguments such as Froude number comparison (Wolowicz et al., 1979). Instead, linear system analysis has been used in this study to reveal similar passive aerodynamic mechanisms on different scales.

3.5 Summary

In this chapter, the curve-fitted insect aerodynamics model (in quasi-steady form) was posed in the context of body translation and rotation by adding the concept of perturbation velocities to formulate the wing aerodynamics as functions of the insect (or vehicle) state. The resulting aerodynamic forces and moments were applied to 6 DOF rigid body equations of motion. The equations were first analyzed via a wingstroke-averaged force and linearization method in analytic form to give controllability term estimates. A numerical simulation of a dipteran insect was then constructed. Geometric, aerodynamic, and inertial properties of a *Drosophila*-like insect were used in the simulator to create time histories that were then analyzed in the frequency domain, and two linear systems identified from the frequency responses, showing that heave dynamics and fore/aft/pitch models are decoupled in the neighborhood of hover.

The perturbation velocity analysis indicates that, for the purpose of controlling velocity along the $\hat{s}_z$ axis, flap frequency and flap amplitude are complementary inputs, but that frequency has only a limited band of linear controllability and is more difficult to use in a linear controls context, while amplitude is much more readily used and is well captured by a linear first order model. It also indicates that an insect modulating the bio-inspired input parameters suggested may effect motion in each longitudinal state (excepting pitch angle, controlled via integration of pitch rate). The identified system indicates a dipteran insect of these dimensions and wing motions has ample control authority over its longitudinal motion, including

pitch dynamics control that significantly exceeds modern full scale helicopter results. Though the system is highly maneuverable, haltere-on pitch control is predicted to qualify for full scale Level 1 small perturbation analysis, indicating the insect is presented with a relatively low computational workload. The implication is that a flapping wing micro air vehicle design strategy may leverage inherent dynamic properties of the flapping wing aerodynamics to reduce size, weight, and power requirements.

Frequency based system identification of the haltere-on system revealed a stabilized system with a slow and fast subsidence mode, and a stable oscillatory mode. Identification of the haltere-off (bare airframe) system revealed a slow and fast subsidence mode, and an unstable oscillatory mode. In both cases, the slow subsidence mode was associated with the decoupled heave dynamics. While this is the first look at the haltere-on modal structure, the bare-airframe modal structure is consistent with the previous CFD estimate of a dipteran insect bare-airframe modal structure. The implication that rate damping due to halteres is sufficient to stabilize the unstable oscillatory pair significantly reduces the computational workload expected for flapping wing insects and provides insight into how insects achieve unparalleled maneuverability with limited neural processing.

Chapter 4

Lateral-Directional Hover Dynamics

4.1 Introduction

Chapter 3 analyzed the longitudinal dynamics of a flapping wing insect about hover using curve-fitted aerodynamics models (Dickinson, 1996) and Euler rigid body dynamics applied to fruit flies. The results indicated slow and fast subsidence modes, as well as an unstable oscillatory mode that could be stabilized via halteres providing pitch rate feedback. This chapter continues to examine the implication of passive aerodynamic stability mechanisms associated with flapping flight, again using hovering fruit flies, but characterizing instead lateral-directional motion. The goal is a simplified dynamics model of flapping flight lateral motion about hover, which may be readily interpreted via traditional full scale aircraft dynamics and linear control analysis techniques. The underlying mechanics are again posed as nonlinear Euler rigid body dynamics paired with quasi steady aerodynamics modeling that includes the effects of perturbations from the equilibrium. The results show that the insect aerodynamics model placed in context of state perturbations is able to predict dynamic behavior without the use of a more detailed and computationally intensive 3D CFD study such as (Ramamurti and Sandberg, 2002, 2007).

The organization of the chapter is as follows. Section 4.2 briefly reviews wing kinematics and aerodynamics with asymmetric inputs. Section 4.3 describes the sys-

tem identification procedure using a nonlinear simulation environment encoding the perturbation velocities concept. Section 4.4 shows how the perturbation velocities concept can be used to develop estimates of the stability and control derivatives, and Section 4.5 presents identified models and shows how these results suggest passive aerodynamic mechanisms that may reduce an insect's flight control requirements about hover.

4.2 Background

The insect aerodynamic theory and the governing equations for the analysis and simulation used for lateral dynamics analysis are analogous to Chapter 3 and reviewed only briefly here.

4.2.1 Wing Kinematics

As in Chapter 3, the right and left wing motion is quantified through a set of 2-3-2 Euler angles. Each wing stroke is planar, with β_r and β_l being the inclination of this plane on the right and left sides. The wing position within this plane is notated as ϕ_r and ϕ_l, and the inclination (twist) of each wing relative to this plane is the geometric angle of attack α_g. The right and left wing variables seen in Fig. 4.1 are interpreted as longitudinal and lateral control inputs $[\ ]_c$ and $[\ ]_d$ using the transformation in Section 3.1.1. Asymmetric inputs were zero for the symmetric motion analysis in Chapter 3 and the subscripts suppressed, but both collective and differential inputs are relevant for lateral-directional motion.

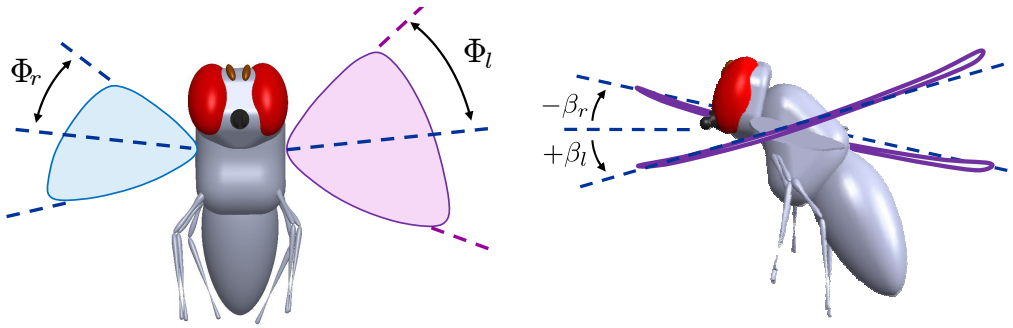

(a) Right and left flap amplitude Φ_r and Φ_l. (b) Right and left stroke plane amplitude β_r and β_l.

Figure 4.1: Control input definitions.

4.2.2 Aerodynamics

The aerodynamics used in this analysis is the insect aerodynamics model developed using experimental fits to *Drosophila* and Robofly data (Dickinson et al., 1999). While this model proposes lift and drag purely as functions of the instantaneous wing motion without inflow effects, the aerodynamic forces are also functions of the body motion throughout the surrounding fluid. Chapter 3 extended the quasi-steady formulation via a revised definition of the wing tip speed to be $\boldsymbol{v} = \boldsymbol{v}_\phi + \boldsymbol{v}^G + \boldsymbol{v}_\omega$, where $\boldsymbol{v}_\phi$, $\boldsymbol{v}^G$, and $\boldsymbol{v}_\omega$ are the velocity components due to flapping, body translation, and body rotation, respectively. The wing angle of attack must also be modified as $\alpha = \alpha_g + \arctan\left(\frac{v_z}{v_x}\right)$, where $\boldsymbol{v} = v_x\hat{r}_x + v_y\hat{r}_y + v_z\hat{r}_z$ is the total velocity expressed in the right wing frame.

4.3 System Identification

To facilitate the identification of an equivalent linear system, the simulator developed in Chapter 3 was used in conjunction with Comprehensive Identification

from FrEquency Responses (CIFER). The goal of this process was to identify a linear system that would allow predictions of the flapping wing flight control properties. Frequency sweeps ("chirp" signals) were applied to the inputs β_d and Φ_d to excite the lateral/directional dynamics of the insect. Based on the spectral response of the input $G_{xx}(\omega)$ and output $G_{yy}(\omega)$ (calculated by the chirp z transform), the transfer function G may be found via

$$G(\omega) = \frac{G_{yy}(\omega)}{G_{xx}(\omega)}. \tag{4.1}$$

As a linearity measurement, coherence $\gamma \in [0, 1]$ was introduced in Section 3.4.2(defined in eqn (3.28)) to quantify the degree to which the magnitude and phase of an input/output pair may be described by linear system dynamics.

Our desired result is a model of the form $\dot{\boldsymbol{x}} = A\boldsymbol{x} + B\boldsymbol{u}$ (Franklin, 2002), where A is most generally taken to be

$$A = \begin{bmatrix} Y_v & 0 & g & 0 \\ L'_v & L'_p & 0 & L'_r \\ 0 & 1 & 0 & 0 \\ N'_v & N'_p & 0 & N'_r \end{bmatrix} \tag{4.2}$$

and

$$B = \begin{bmatrix} Y_{\Phi_d} & 0 \\ L_{\Phi_d} & 0 \\ 0 & 0 \\ 0 & N_{\beta_d} \end{bmatrix}. \tag{4.3}$$

4.4 Wingstroke Averaged Forces and Moments

In this section, the process of wingstroke averaging developed in Chapter 3 is applied to demonstrate how linearization of rigid body equations of motion forced by experimentally-derived insect aerodynamics can provide estimates of the control input terms and also indicate physical mechanisms providing aerodynamic damping. The linear systems representing rigid body motion were derived with the understanding that we are concerned only with the low frequency rigid body modes describing the flight path of the vehicle, i.e., that the averaged forces and moments (over a wingstroke) were the essential part of the external forcing function. Application of this principle provides insight into what physical mechanisms provide passive aerodynamic damping.

4.4.1 Control Sensitivity

A system identification requires an initial estimate of the relevant parameters. The control sensitivity terms, or the entries of the B matrix (eqn (4.3)), were estimated via the wingstroke averaging procedure. The roll sensitivity to the inputs Φ_d, $\phi_{\text{off,d}}$, and β_d is derived here; other terms may be found in like manner.

4.4.1.1 Roll Moment due to Differential Stroke Amplitude Φ_d

For the case of zero stroke plane angle $\beta = 0$, the roll moment can be written in terms of the left and right wing lifts as $L_{\text{roll}} = (L_l - L_r)r_a$, where L_l and L_r are defined as $L_x = \pi^2(\hat{r}_2^2\, S\, R^2)(f_x^2\, \Phi_x^2)C_l$ with $x = l, r$. Though the angle of attack on each wing is different in general, they share the same lift coefficient during a perturbation of Φ_d while hovering. Using Φ_d as defined in eqn (3.2), the roll moment is

$$\begin{aligned} L_{\text{roll}} = \pi^2\rho(\hat{r}_2^2 SR^2)r_a\, [(f_c - f_d)^2(\Phi_c - \Phi_d)^2 \cos(\phi_{\text{off,c}} - \phi_{\text{off,d}}) \\ -(f_c + f_d)^2(\Phi_c + \Phi_d)^2 \cos(\phi_{\text{off,c}} + \phi_{\text{off,d}})]\, C_L \end{aligned} \tag{4.4}$$

Linearizing with respect to Φ_d and substituting in the nominal conditions $\Phi_d = f_d = \phi_{\text{off,d}} = 0$ to obtain

$$\frac{\partial L_{\text{roll}}}{\partial \Phi_d} = -4\pi^2\rho(\hat{r}_2^2 SR^2)C_L\, r_a \cos(\phi_{off,c}) f_c^2 \Phi_c. \tag{4.5}$$

Using the nominal conditions for *Drosophila* in Table 4.1, $\frac{\partial L_{\text{roll}}}{\partial \Phi_d} = -8.84 \times 10^{-9} C_L$ N m/rad. For $\alpha_g = 45$, $C_L = 1.8$, and a roll inertia of $5.9 \times 10^{-13}\text{Nms}^2$, $L_{\Phi_d} = -26,969$ rad/s^2.

control input	value
f_0	200 Hz
Φ_0	77.08°
β_0	0°
ξ	90°
r_a	1.6mm

Table 4.1: Nominal input parameters used in evaluating B for the hover linearization.

4.4.1.2 Roll Moment due to Differential Stroke Bias $\phi_{\text{off,d}}$

Similarly, computation of the derivative with respect to $\phi_{\text{off,d}}$ and substitution of the nominal conditions yields

$$\frac{\partial L_{\text{roll}}}{\partial \phi_{\text{off,d}}} = 2\pi^2 \rho (\hat{r}_2^2 S R^2) r_a f_c^2 \Phi_c^2 \sin(\phi_{\text{off,c}}), \tag{4.6}$$

indicating that for a nominal collective stroke offset of 0, a differential stroke offset does not lead to a roll moment via changing lift.

4.4.1.3 Roll Moment due to Differential Stroke Plane Inclination β_d

The body frame Z force due to right wing lift is $Z_r = L_r \cos(\beta)$ (and similarly for the left side). Thus, the roll moment may be found after replacing L_r with $L_r \cos(\beta)$ to get $L_{\text{roll}} = (L_l \cos(\beta_l) - L_r \cos(\beta_r)) r_a$. Defining β_d and β_c as in eqn (3.2) such that $\beta_r = \beta_c + \beta_d$ and $\beta_l = \beta_c - \beta_d$, one may rewrite the roll moment as

$$L_{\text{roll}} = [L_l \cos(\beta_c - \beta_d) - L_r \cos(\beta_c + \beta_d)] r_a. \tag{4.7}$$

By recognition that L_l and L_r are invariant under β perturbations, eqn (4.7) may be differentiated with respect to β_d directly to get

$$\frac{\partial L_{\text{roll}}}{\partial \beta_d} = r_a L_r \sin(\beta_d + \beta_c) + r_a L_l \sin(\beta_d - \beta_c), \tag{4.8}$$

and evaluated at $\beta_c = 0$,

$$\left.\frac{\partial L_{\text{roll}}}{\partial \beta_d}\right|_{\beta_c=0} = r_a \sin(\beta_d)(L_r - L_l). \tag{4.9}$$

Equation (4.9) is zero at the reference $\beta_d = 0$, revealing that differential stroke plane inclination about $\beta_c = \beta_d = 0$ does not create a roll moment.

4.4.2 Physical Basis for Passive Aerodynamic Mechanisms

Wingstroke averaging applied to rigid body equations of motion and the insect aerodynamics model including perturbations indicates several physical mechanisms that provide aerodynamic damping. Sideslip damping is used as an example, and the other terms can be found via a similar process.

4.4.2.1 Sideslip Damping

Consideration of imposed velocities has led to the prediction of a flap damping term (Hedrick et al., 2009). In this section, an imposed sideslip velocity is expressed via the velocity and angle of attack perturbations to predict sideslip damping, or static stability in this degree of freedom.

Consider the case of positive sideslip along $\hat{s}_y$ (a relative wind from the right). The total motion of the wing is now the sum of flapping and vehicle translation motions. Figure 4.2 shows that sideslip velocity increases the airflow over some portions of the wingstroke (darker) and decreases it over other portions (lighter), where the inboard region of reverse flow has been neglected. For the nominal case

of a level stroke plane with no heave velocity, a sideslip component of velocity does not change the angle of attack.

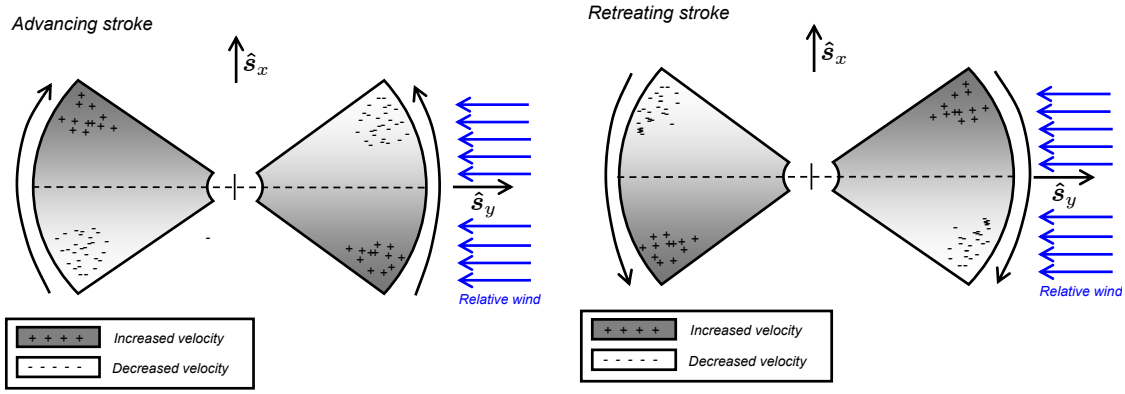

(a) Advancing (b) Retreating

Figure 4.2: An imposed sideslip increases and decreases relative airflow over regions of the wingstroke.

The translational model of drag accounts for velocity via a quadratic dependence on the local velocity. The drag is increased in those regions of increased flow and reduced in those regions of reduced flow as seen in Fig. (4.3), which shows that in both the advancing and retreating strokes, the perturbation in drag leads to a net force in the $\hat{s}_y$ direction, acting to oppose the motion.

Analytically, instantaneous right wing drag force under a sideslip motion ex-

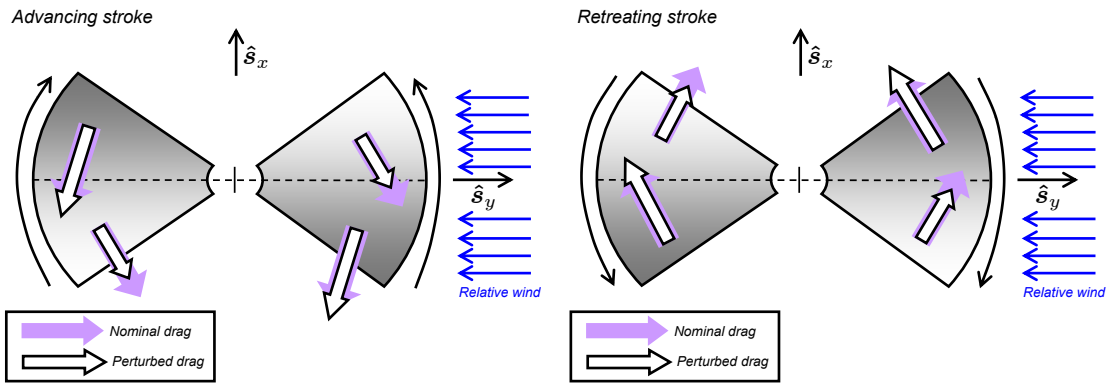

(a) Advancing (b) Retreating

Figure 4.3: An imposed sideslip increases and decreases drag forces during the advancing and retreating strokes in a manner leading to damping in sideslip v about hover.

pressed in stability frame, with $\beta_r = 0$ and $\phi_{\text{off,r}} = 0$, is

$$[F_{D,r}]_S = \begin{bmatrix} -1/2\,\rho\,S\,\hat{r}_2^2\,C_D\ (2\,\Phi_r\ \sin(2\,\pi\,f_r\,t)\,\pi\,f_r\,R \\ \qquad\qquad + \sin(\Phi_r\ \cos(2\,\pi\,f_r\,t))\,v)^2\,\cos(\Phi_r\ \cos(2\,\pi\,f_r\,t)) \\ -1/2\,\rho\,S\,\hat{r}_2^2\,C_D\ (2\,\Phi_r\ \sin(2\,\pi\,f_r\,t)\,\pi\,f_r\,R \\ \qquad\qquad + \sin(\Phi_r\ \cos(2\,\pi\,f_r\,t))\,v)^2\,\sin(\Phi_r\ \cos(2\,\pi\,f_r\,t)) \\ 0 \end{bmatrix}_S \tag{4.10}$$

for the advancing stroke and the negative of eqn (4.10) for the retreating stroke. The left wing has a similar expression. The wingstroke averaged side force is

$$\frac{d}{dv}[Y_{avg}]_S = \frac{d}{dv}\int_0^T [F_{D,r}]_S + [F_{D,l}]_S\,dt. \tag{4.11}$$

Interchanging the order of integration and differentiation, the right and left wing terms contribute equally. Define sideslip damping $Y_v = \frac{1}{m}\frac{\partial Y_{avg}}{\partial v}$ to write

$$Y_v = \frac{4\rho\, S\, \hat{r}_2^2\, R\, C_D}{m} \left[\cos\left(\Phi_c\right) \sin\left(\Phi_c\right) - \Phi_c\right] \tag{4.12}$$

The values given by eqn (4.12) directly compare against other air vehicles as in Fig. (4.4).

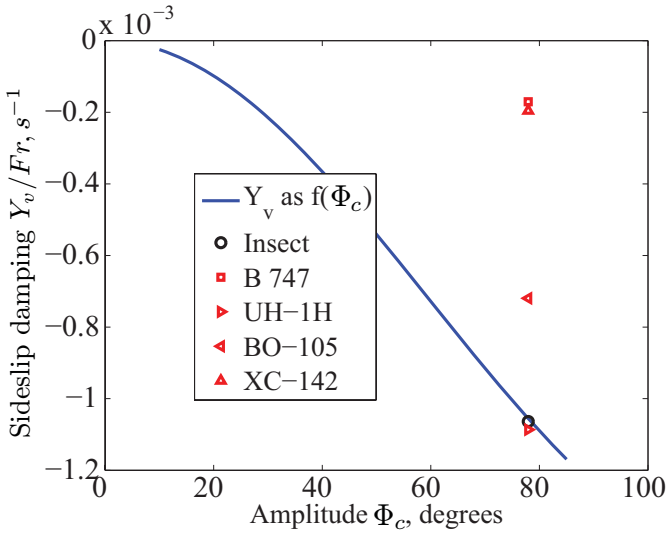

Figure 4.4: Comparison of calculated Y_v with Boeing 747, UH-1 Huey, BO-105 helicopter, and XC-142 tactical transport. All values normalized by Froude number.

4.4.3 Active Feedback Mechanisms

The flight stabilization systems of many dipteran insects include halteres, aerodynamically-ineffective hind wings that are used as angular feedback sensors (Nalbach, 1994). The kinematic response Φ_d due to mechanosensory feedback has been characterized for tethered *Drosophila* (Sherman and Dickinson, 2003). The measurements were used to model the mechanosensory feedback as a bandpass filter on linear roll rate feedback to Φ_d, in a similar manner to the pitch rate feedback used in Chapter 3, The yaw rate feedback to β_d output has not been characterized exper-

imentally and was not included in the simulated insect. In general, rate feedback acting on a system may be written as $\boldsymbol{u} = K\boldsymbol{x}$, where the gain matrix K has only terms dependent on angular rates. While rate feedback alone will not stabilize an unstable system, rate feedback has the effect of additional damping in the system. Application of yaw rate feedback would further reduce the bandwidth demands for the flight stabilization and control task via the increase in the yaw damping term N'_r due to the additional damping.

4.5 Results and Discussion

4.5.1 Yaw Dynamics

In this section, the yaw dynamics results are compared to previous modeling work. Consider the yaw dynamics case previously discussed in Hedrick et al. (2009), where a linear yaw dynamics model of the form

$$\dot{r} = -a\, r$$

was calculated, where a is formed from the wing's geometric and kinematic parameters as

$$a = \frac{\rho\, R^4\, \bar{c}\, \hat{r}_3^3\, 2\Phi\, f\, \overline{C_F \sin(\alpha)(d\hat{\phi}/d\hat{t})}}{I'_{zz}}.$$

Here, the term formed by the force coefficient C_F, geometric wing angle α_g, and nondimensional flap speed $d\hat{\phi}/d\hat{t}$ has the mean value $\overline{C_F \sin(\alpha_g)(d\hat{\phi}/d\hat{t})} \approx 6.0$. Using parameters from the simulated insect, the FCT model predicts an aerodynamic

damping coefficient of $N'_r = -167$ /s, somewhat higher than both the analytic and the system identification results. When the simulated insect was tethered with only a yaw degree of freedom, an equivalent linear system was identified as

$$\dot{r} = -73.0\, r - 28,100\, \beta_d. \tag{4.13}$$

Despite the differences in the stability derivative, the associated transfer functions from β_d to r as calculated from the simulation, FCT (Hedrick et al., 2009), and identified models may be seen to have very good spectral agreement in Fig. 4.5.

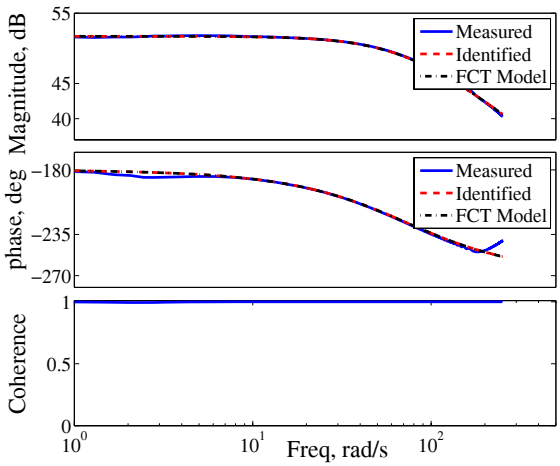

Figure 4.5: Yaw input β_d is well correlated linearly to yaw rate r and the 3 available models show excellent spectral agreement.

4.5.2 Roll Dynamics

4.5.2.1 Linear System

Application of Φ_d sweeps confirms that Φ_d is the roll input control as seen in Fig. 4.6,[1] with no linear component to the yaw output (as indicated by the low coherence). The degradation in coherence seen in the other plots at approximately 4-5 Hz is related to a resonant phenomenon in the roll axis that yielded motion outside a linear region. This motion appears in the identified system as a lightly damped oscillatory pair.

A linear roll dynamics system may be identified as

$$\begin{bmatrix} \dot{v} \\ \dot{p} \\ \dot{\phi} \end{bmatrix} = \begin{bmatrix} -9.86 & 0 & 9.81 \\ -9830 & -177 & 0 \\ 0 & 1 & 0 \end{bmatrix} \begin{bmatrix} v \\ p \\ \phi \end{bmatrix} + \begin{bmatrix} 16.5 & 0 \\ -12200 & 0 \\ 0 & 0 \end{bmatrix} \begin{bmatrix} \Phi_d \\ \beta_d \end{bmatrix}. \quad (4.14)$$

4.5.2.2 Physical Mechanism Predicting Roll Damping

The quasi steady model with perturbations predicts roll damping via differential angle of attack consideration. The angle of attack modification is similar to the heave damping case discussed in the longitudinal analysis, and is seen in Fig. 4.7.

[1] Identified system shown in transfer function plots is the final full lateral/directional coupled system in section 4.5.3.

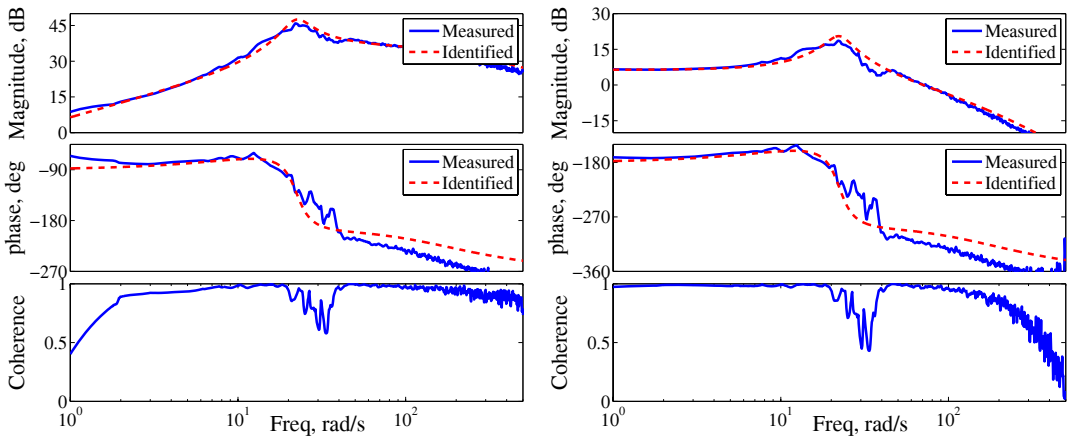

(a) Φ_d to p

(b) Φ_d to ϕ

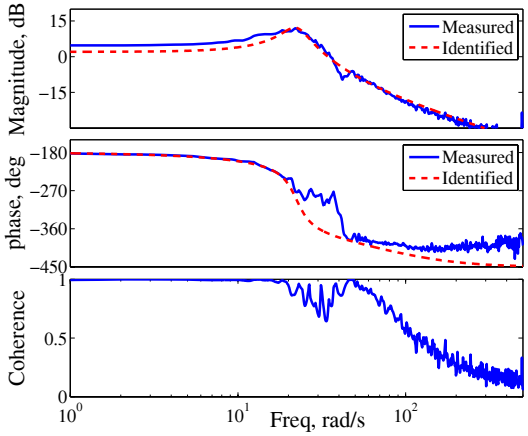

(c) Φ_d to v

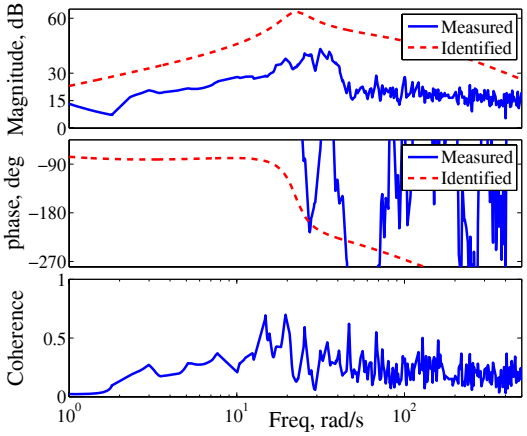

(d) Φ_d to r

Figure 4.6: Roll input Φ_d drives the roll/sideslip dynamics, but not yaw.

4.5.3 Full Lateral Dynamics

The two identified systems in eqn (4.13) and (4.14) describe the behavior of the isolated systems, but the general system included in eqn (4.2) and (4.3) includes numerous cross coupling terms that may be important. The inclusion of the cross

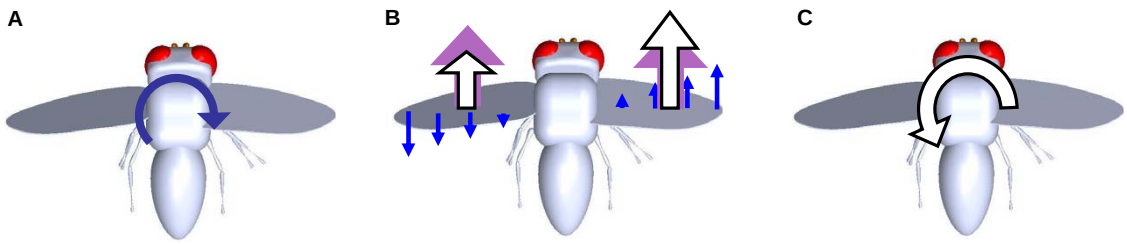

Figure 4.7: The applied roll motion in (a) creates a counter-moment in (c) via the difference in angle of attacks imposed by the velocity distribution in (b).

coupled terms does change the state space representation of the system to be

$$\begin{bmatrix} \dot{v} \\ \dot{p} \\ \dot{\phi} \\ \dot{r} \end{bmatrix} = \begin{bmatrix} -9.69 & 0 & 9.81 & 0 \\ -9720.0 & -177.0 & 0 & -2.07 \\ 0 & 1 & 0 & 0 \\ -167.0 & 462.0 & 0 & -71.0 \end{bmatrix} \begin{bmatrix} v \\ p \\ \phi \\ r \end{bmatrix} + \begin{bmatrix} 8.24 & 0.0 \\ -12300.0 & 0 \\ 0 & 0 \\ 0 & -28100.0 \end{bmatrix} \begin{bmatrix} \Phi_d \\ \beta_d \end{bmatrix}. \tag{4.15}$$

During this identification, the earlier terms were allowed to vary freely as well, which results in slight changes in the numerical values. As an example, N'_r shifts from -73 in the yaw-only model to -71 in the full lateral model. One may compare these changes to the error bounds calculated later in Table 4.2 to determine if the changes are significant. Despite the change in state space appearance, model structure determination applied to the system indicates that the additional cross terms are poorly identified and should not be included in this model. The system pole structure (which determines the qualitative nature of the body motion) is also remarkably consistent between the decoupled (eqn (4.13) and (4.14)) and coupled (eqn (4.15)) system, as indicated by Fig. 4.8, which represents the first formal inves-

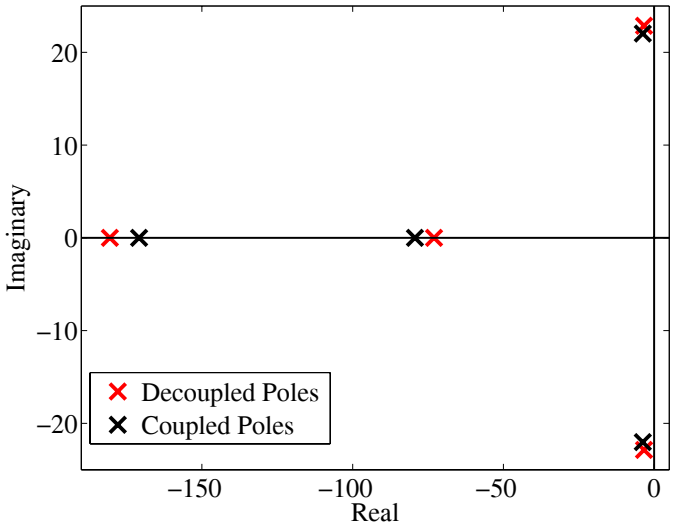

Figure 4.8: Comparison of the poles identified for the coupled and uncoupled system.

tigation of the lateral dynamics poles of a *Drosophila*-like insect. Both cases show a fast and slow subsidence mode, and an oscillatory mode close to instability, which suggests significantly reduced insect neural dependence for flight control. The pole structure observed in Fig. 4.8 is also consistent with other manned flight vehicles, such as the UH1 Huey helicopter (Franklin, 2002). The fact that qualitatively similar stability behavior (pole structure) is observed between two vehicles where both the scale and the lift production mechanisms are quite different is remarkable: there is no dynamic reason to expect such similarity, and the term that would normally be matched for dynamic similitude (Froude number) is not matched in this case (Wolowicz et al., 1979).

While the eigenvalues (system poles) of a linear system determine the qualitative nature of the body response, the eigenvectors indicate the direction of this response. For the union of the roll/sideslip and yaw system (eqn (4.13) and (4.14)),

Parameter	Value	Standard Dev. σ	Insensitivity
Y_v	-9.69	5.1%	1.8%
L'_v	-9720	6.3%	1.2%
L'_p	-177	7.1%	1.3%
N'_r	-73	9.0%	2.1%
L_{Φ_d}	-12,300	5.9%	1.2%
N_{β_d}	-28,100	7.8%	1.8%

Table 4.2: Uncertainty estimates for parameters in the identified dynamics model.

the poles $(\lambda_1, \lambda_{2,3}, \lambda_4) = (-73, -3.4 \pm 22.9i, -180.5)$ have the eigenvectors

$$\nu_1 = \begin{bmatrix} 0 \\ 0 \\ 0 \\ 1 \end{bmatrix} \nu_{2,3} = \begin{bmatrix} 0.018, \mp 173^\circ \\ 0.999 \\ 0.043, \mp 98^\circ \\ 0 \end{bmatrix} \nu_4 = \begin{bmatrix} 0.000 \\ 1.000 \\ 0.006 \end{bmatrix}, \tag{4.16}$$

indicating roll and yaw subsidence modes ν_1 and ν_4 along with an oscillatory roll-dominated roll/sideslip mode ν_2, ν_3.

An estimate of the uncertainty in the identified stability derivatives may be derived from the Cramer-Rao bounds using the methods in Tischler and Remple (2006). The resulting uncertainties, shown in Table 4.2, do not quantitatively change the identified system pole structure, as indicated in Fig. 4.9, which shows the nominal poles and the poles perturbed by normally-distributed noise corresponding to the uncertainty predictions.

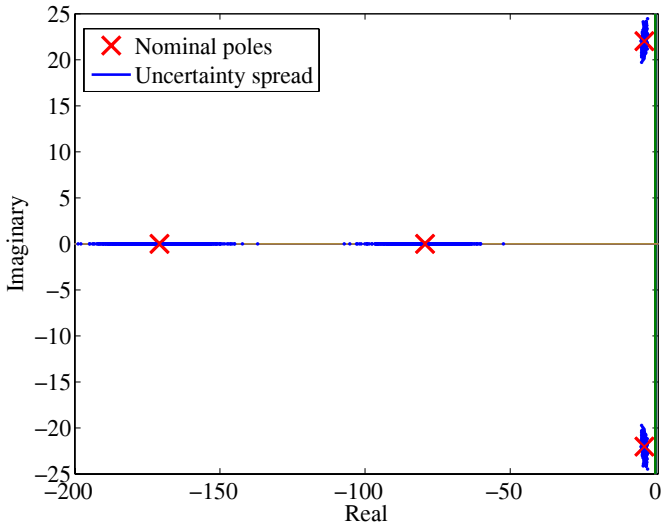

Figure 4.9: The identified system pole structure is preserved under uncertainty perturbations.

4.6 Summary

In this chapter, the insect aerodynamics model including perturbations was analyzed to determine reduced order control models that may be used to estimate the control properties associated with lateral-directional flight. The models were derived with the goal of describing the low order rigid body motion of an insect, (not high frequency structural dynamics), so frequency-based system identification tools and wingstroke-based averaging were both used in deriving them. In each case, a curve fitted aerodynamics was used in the context of untethered dynamic motion of the insect body, rather than a detailed 3D flow solution found during a prescribed body motion, such as three-dimensional flowfields computed in (Ramamurti and Sandberg, 2007) or in the Model Validation of Chapter 5.

For the example insect considered (*Drosophila*-like insect), the analysis indicates two stable real poles, and two very lightly-damped and nearly unstable complex

poles. One of the real poles is found to correspond to the yaw dynamics of the insect, showing a decoupling of motion about this axis near hover, allowing comparison to Hedrick et al. (2009). The other three poles describe a coupled roll/sideslip motion that may be excited by a roll input, defined in this study as a differential modulation of the wingstroke amplitude. The yaw dynamics input was found to be a differential stroke plane angle (inclination). The models were also used to estimate the effect of pole additional off-axis dynamic cross-coupling and uncertainties, which show that the dynamic structure is preserved in these cases. Haltere-based roll rate feedback was integral to restraining the modeled insect near equilibrium and was included in these models, which allows the models to be driven directly via the control components that have significantly higher latencies (and thus lower bandwidth), such as the visual feedback system Humbert and Hyslop (2010).

The dynamic analysis suggests that mechanosensory rate feedback is an integral part of the animal's control strategy. The study's analysis also suggests that inherent passive aerodynamic mechanisms due to differences in angle of attack and dynamic pressure, can act to stabilize the vehicle and thus reduce the flight stabilization/control requirements. From the perspective of developing robotic flapping wing micro air vehicles, the ability to leverage passive aerodynamic mechanisms to assist in flight stabilization is attractive to reduce the size, weight, and power requirements of the control system that must be carried onboard.

Chapter 5

Model Validation

5.1 Introduction

An important problem in flapping micro air vehicle (MAV) design is a method of rejecting wind gusts and maneuvering through unknown wind gradients in a rapidly changing environment. Fundamental to solving this problem is the level of sensing and feedback requirements inherent in flapping wing flight. This dissertation has derived reduced order models of flapping wing flight using simplified aerodynamics, and this chapter compares reduced order modeling results against more traditional modeling, using computational fluid dynamics (CFD) modeling in collaboration with Mac MacFarlane and Brandon Bush (Bush, B. et al., 2010). The high fidelity CFD solutions incorporate more complex aerodynamics such as unsteady flow, wing/wake interaction, and wake capture effects.

The reduced order longitudinal dynamics model for a hovering *Drosophila* (fruit fly) presented in Chapter 3 had bare airframe instabilities but could be stabilized with the addition of a biological pitch rate feedback. The model was developed using a comparatively simple aerodynamics model. Euler rigid body dynamics were then used to simulate a hovering insect and a system identification performed to model the inputs and outputs. A CFD-derived solution could significantly improve the fidelity of the aerodynamics model, at the expense of dramatically increased

complexity. The goal of this chapter is to directly compare stability derivatives as well as pole locations derived using each method.

The longitudinal dynamics of the insect are described in the standard state space form $\dot{\mathbf{x}} = A\mathbf{x} + B\mathbf{u}$, where $\mathbf{x} = [\Delta u\ \Delta w\ \Delta q\ \Delta\theta]^T$ is the vector of longitudinal perturbation states and $\mathbf{u}$ is the vector of inputs to the system. The stability matrix, A, is comprised of stability derivatives: linear changes in a stroke-averaged force or moment due to perturbations from hover.

$$A = \begin{bmatrix} X_u & 0 & 0 & -g \\ Z_u & Z_w & 0 & 0 \\ M_u & M_w & M_q & 0 \\ 0 & 0 & 1 & 0 \end{bmatrix} \tag{5.1}$$

To calculate the stability derivatives, the stroke-averaged body forces, X and Z, and pitching moment, M, were measured for various perturbations from hover. As before, only the forces and moments averaged over the course of a wingstroke are considered important to the rigid body dynamics, due to the high frequency of the wingstroke with respect to the frequency of the body dynamics.(Deng et al., 2006b; Kevorkian, 1966) The stroke-averaged forces and moments can be calculated using both the curve-fitted aerodynamics model of aerodynamics and CFD, providing a stability matrix derived from each method. This allows a direct comparison of the linearized system generated by curve-fitted aerodynamics to the linear system produced by fully unsteady aerodynamics, as given by CFD.

5.2 Unmodeled Aerodynamics and Velocity Perturbations

5.2.0.1 Rotational Lift and Other Aerodynamic Models

There are aerodynamic effects not adequately represented in the translational model in Section 3.1.3. In particular, force peaks appear at the start and end of the wing strokes where the translational representation shows only small forces due to the small velocities while the wing is reversing direction. Wing incidence rapidly reverses at these instants, so a convenient representation is to write this additional lift peak as a function of the wing incidence derivative $\dot{\alpha}_g$. While rotational effects can account for up to 35% of the lift generated(Dickinson et al., 1999), modeling lift in this manner requires a theoretical or experimental determination of the wing axis of rotation that has not been demonstrated with the precision necessary for accurate predictive capability in the general case of dipteran insect flight (Bennett, 1970). Other force production models involve a variety of unsteady effects such as added mass effects (approximately 5% of lift forces). This study addressed the effects of translational lift, which applies to dipteran insect flight in general.

5.2.0.2 Reverse Flow

In contrast to the curve-fitted model's u_t, the total flow incident on the wing $\boldsymbol{v}$ is no longer necessarily opposite to the flap direction. An example is in forward flight during the retreating stroke where inboard sections of the wing generate negative lift. A region of reverse flow is a common problem encountered on helicopter rotors where the magnitude of its effects are quantified using a nondimensional speed known as the

advance ratio $\mu = u/u_t = \frac{u}{\dot{\phi}R}$. For a *Drosophila*-like insect flapping at $f = 200$Hz, the peak angular rate is $\max(\dot{\phi}) = \Phi(2\pi f) \approx 1755$rad/s, leading to a peak wing velocity at the tip of $\max(u_t) = 3.7$m/s, and hence a minimal advance ratio at the insect's preferred forward speed of 2m/s (Vogel, 1967), the corresponding advance ratio of 0.54 for a level stroke plane angle is the lowest advance ratio in "cruise." For comparison, a typical helicopter can fly no faster than approximately $\mu_{\max} = 0.35$ to 0.40 (Johnson, 1994) and reverse flow effects are likely a significant factor in forward flight. In this analysis, the insect is restricted to motions less than ~10 cm/s or $\mu < 0.03$ at peak angular velocity. Helicopter analysis routinely discards reverse flow below $\mu = 0.1$, so reverse flow effects are expected to be secondary and this effect was assumed negligible in the reduced order aerodynamic model presented in Chapter 3.

5.2.0.3 Spanwise Flow

Where the traditional quasi-steady aerodynamics formulation assumed $v_y = 0$, v_y is now a periodic function of ϕ. Spanwise flow is a term that is often neglected in the wing frame airfoil lift and drag calculations, even in extensive detailed numerical simulations of traditional helicopters via blade element theory, because published airfoil data is commonly in 2D and one may invoke the "independence principle" (Jones and Cohen, 1957). In performance calculations, an estimate of the rotor's profile drag along this axis is usually included (Leishman, 2006). As a consequence of the 2D nature of the airfoil lift and drag representation, spanwise flow was neglected

in the reduced order aerodynamic model presented in Chapter 3..

5.3 Methodology

5.3.1 Kinematics

Wing kinematics are defined about each hinge as in Section 3.1.1, flapping in a plane inclined from body axes by β. Motion of the wing within the plane is termed stroke angle ϕ, and rotation relative to the plane is the geometric angle of attack α_g.

$$\phi(t) = \Phi \cos(2\pi f t) + \phi_{\text{off}} \tag{5.2}$$

$$\alpha_g(t) = \alpha_{\max} \tanh[2.7 \sin(2\pi f t + \psi \frac{\pi}{180})] \tag{5.3}$$

where Φ and $\alpha_{\max}$ are stroke and wing pitch amplitudes, f the flapping frequency, ϕ_{off} a stroke bias term, and ψ is a relative phase difference between ϕ and α_g. In the nominal stereotyped *Drosophila* hovering kinematics, β and ϕ_{off} are both zero, $\Phi = 74.9°$, $f = 200$ Hz, $\alpha_{max} = 45°$, and $\psi = 66°$ (Dickinson et al., 1999).

5.3.2 Reduced-Order Aerodynamic Model

While flapping wing aerodynamics are both complex and unsteady, the reduced order aerodynamic model presented in Section 3.1.3 and used to develop the models presented approximates wing forces as functions of the wing tip speed and angle of

attack. Lift L is defined by

$$L = \frac{1}{2}\rho \mathbf{U}_{tip}^2 S \hat{r}_2^2 C_L(\alpha) \tag{5.4}$$

where ρ is air density, S is the surface area of the wing, and $\hat{r}_2$ is the non-dimensional second moment of wing area as defined in (Ellington, 1984c). Drag is defined similarly in Section 3.1.3, and the lift and drag coefficients are measured experimentally by Dickinson and Gotz (1999) for a *Drosophila* wing. Other terms suggested by Sane and Dickinson (2002), such as Kramer effect, added mass, or wake capture are not included in the present calculation. Perturbations from hover affect the tip speed and angle of attack.

5.3.3 Computational Methodology

Detailed flow computations around the hovering *Drosophila* are provided by an immersed boundary incompressible Navier-Stokes solver (IBINS) previously validated for flapping *Drosophila* wings via experimental comparison (Bush, B. and Baeder, J., 2008; Bush, B. et al., 2010). The insect is modeled as three bodies moving through a Cartesian mesh with hyperbolic grid spacing, as seen in Fig. 5.1.

During the computational solution, similtude requirements require both the Reynolds' number $Re = 120$ and reduced frequency $\hat{f} = 0.19$ to be maintained.(Shyy, W. et al., 2008) Reynolds number consistency is necessary for aerodynamic similtude and is determined by the mean wing chord $\bar{c}$, average wing tip speed U_{ref}, and

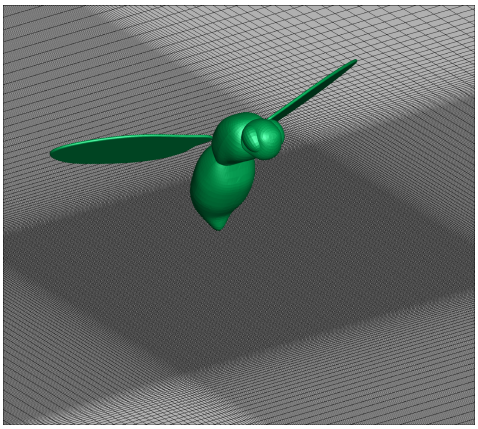

Figure 5.1: The model drosophila in the computational domain used for IBINS calculations.

viscosity μ.

$$Re = \frac{\bar{c}U_{ref}}{\nu} = 120 \tag{5.5}$$

Reduced frequency (related to Strouhal number) is introduced if the Navier-Stokes equations are nondimensionalized via flapping frequency. Reduced frequency describes vortex shedding (unsteadiness) and can be shown to be a geometric ratio involving stroke amplitude and aspect ratio, as in eqn (5.6).

$$k = \frac{\pi f \bar{c}}{U_{ref}} = \frac{\pi \bar{c}}{4R\Phi} = 0.19 \tag{5.6}$$

5.4 Computational Results

State perturbations were applied to the model for the longitudinal states, and stroke-averaged forces and moments were calculated. The trim force along the body frame $\hat{s}_x$ (fore-aft) axis is similar, while discrepancies exist along the body-frame $\hat{s}_z$ axis, most likely a function of the previously unmodeled unsteady aerodynamics.

For example, wake capture effects shown in Fig 5.5 have a significant effect on the flow structure surrounding the wing while maneuvering. For each force or moment, the derivatives with respect to states u, w, and q are estimated via a linear regression (shown as a slope) and scaled by mass or inertia to calculate the stability derivatives populating the A matrix.

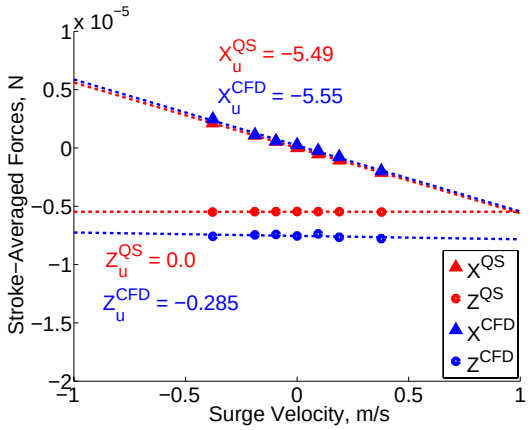

(a)

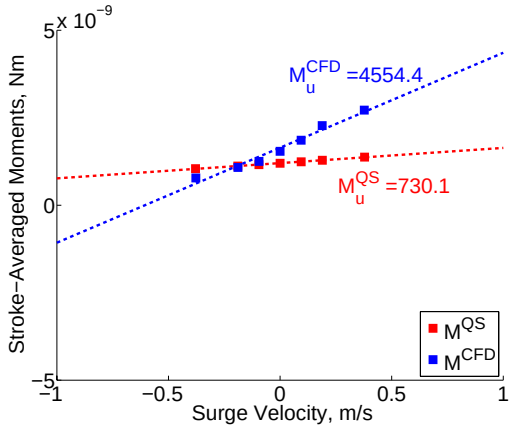

(b)

Figure 5.2: Stroke-averaged forces (a) and moments (b) as given by the curve-fitted experimental model (red) and IBINS (blue) for various perturbations in u.

Table 5.1 summarizes the stability derivatives for the curve-fitted insect aerodynamics model and the IBINS aerodynamic calculation. Comparison of the derivatives all shows the same sign. The magnitudes of the translational derivatives agree

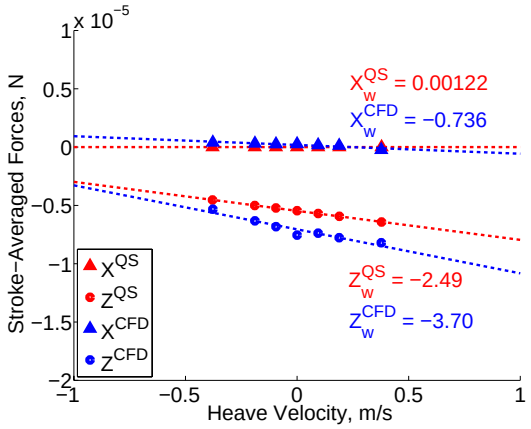

(a)

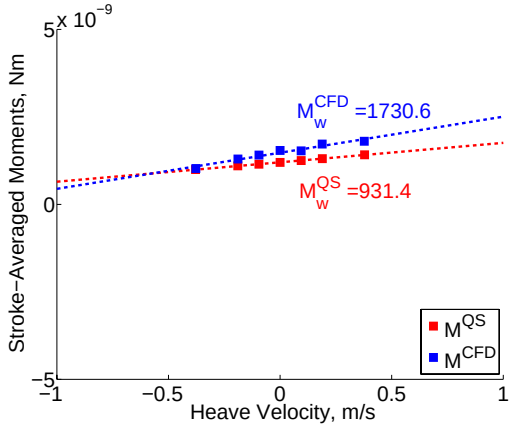

(b)

Figure 5.3: Stroke-averaged forces (a) and moments (b) as given by the curve-fitted experimental model (red) and IBINS (blue) for various perturbations in w.

well, as seen in Figs 5.2–5.4. X_u in particular shows only a 6% difference.

However, the moment derivatives show significant deviations, suggesting that the unmodeled aerodynamic effects influence the rotational dynamics more than the translational dynamics. Rotational lift, in particular, is known to be a significant component of flight forces and causes force peaks that occur at stroke reversal where the wing has the largest moment arm and is most able to effect pitch motions (Dickinson et al., 1999). M_u is most poorly estimated (a factor of 6) by the experimentally-fitted model.

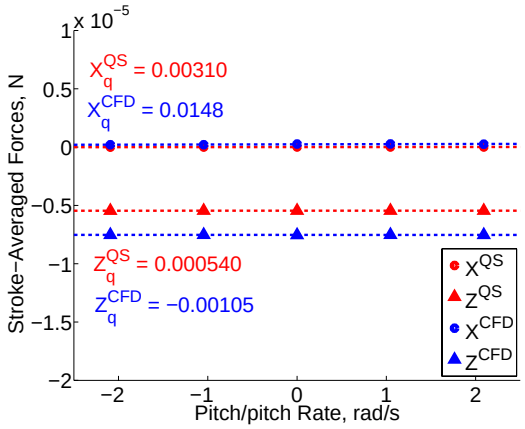

(a)

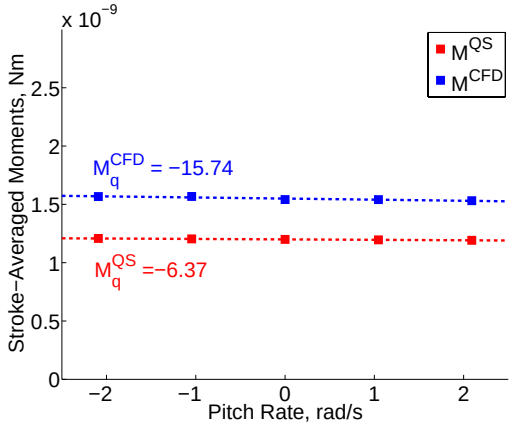

(b)

Figure 5.4: Stroke-averaged forces (a) and moments (b) as given by the curve-fitted experimental model (red) and IBINS (blue) for various perturbations in q.

A comparison of each of system pole locations may be found by reference to Fig 5.6, showing again fast and slow subsidence modes with an unstable oscillatory pair. The decoupled pole Z_w shows excellent agreement. However, the deviations in the moment derivatives have doubled both the rate of convergence in the fast subsidence mode and the rate of instability in the unstable oscillatory pair. The change in rate is due to the deviation in M_u, and is particularly significant because the speed of the unstable pair dictates the level of feedback required to stabilize the system.

Stability Derivative	Curve-Fitted	CFD
X_u	-5.49	-5.55
Z_u	0.0	-0.285
M_u	730.1	4554.4
X_w	0.00122	-0.736
Z_w	-2.49	-3.70
M_w	931.4	1730.6
X_q	0.00310	0.0148
Z_q	5.40e-4	-0.00105
M_q	-6.37	-15.74

Table 5.1: Stability derivatives as calculated by the curve-fitted model and IBINS.

5.5 Summary

In this chapter, the curve-fitted insect aerodynamics model used to derive reduced order flight dynamics models was compared to a numerical solution of the Navier-Stokes equations for incompressible flow, which includes unsteady and other unmodeled aerodynamic effects. Finite differencing through 5 points was used to estimate the derivatives with respect to the states u, w, and q and thus obtain stability derivatives for the derivatives. Translational stability derivatives agree well, while there are significant deviations in the moment derivatives. The system pole locations again show both a fast and slow subsidence mode and an unstable pair. However, the un-modeled aerodynamics increase the rate of both convergence and divergence in the system. In particular, the increased rate of divergence increases the feedback requirements for flight stabilization, the implications of which will be addressed in the next chapter.

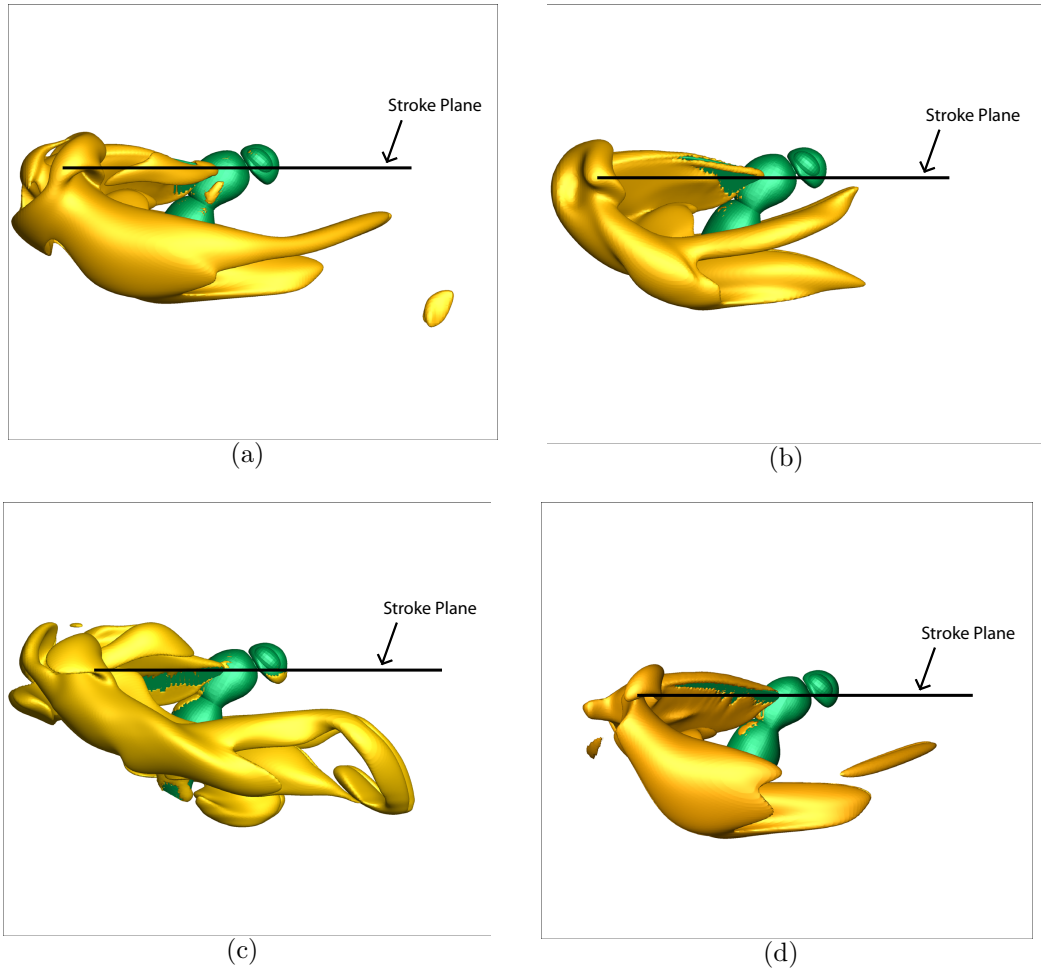

Figure 5.5: Isosurfaces of Q-criterion of the model *Drosophila* in hover (a), surge $\Delta u = 0.38\ m/s$ (b), heave $\Delta w = 0.38\ m/s$ (c), and pitch $\Delta q = 2.1\ rad/s$ (d) just after pronation. The disturbed flow due to the previous wingstroke remains only a single chord length away from the returning stroke in all cases, and influences the loads on the wing.

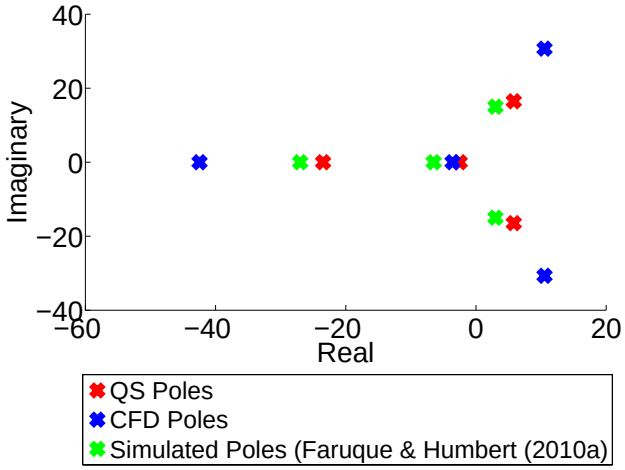

Figure 5.6: Longitudinal poles of the model *Drosophila* in hover as calculated using the curve-fitted experimental aerodynamics model (red) and CFD (blue). Poles found via system identification with the experimentally-derived model in Faruque and Humbert (2010) are plotted alongside for reference (green).

Chapter 6

Feedback Effects and Parameter Variation

The longitudinal and lateral models developed in Chapters 3 and 4 are derived for a nominal *Drosophila* and for both bare airframe and haltere mediated dynamics. Section 6.1 explores the dynamic properties of a model with varying levels of feedback between these two extreme cases. Chapter 5 showed that differences in the reduced-order model are primarily in rate of divergence, which increases the feedback requirements. Section 6.2 applies mechanosensory feedback to the haltere model to determine the magnitude of additional feedback required.

While the model's dynamic properties were shown to be preserved under the estimated uncertainty within the stability and control derivatives, morphological differences between individuals of a species also affect the dynamic properties of the model. Section 6.3 quantifies this variation by exploiting *Drosophila*'s sexual dimorphism to allow comparison of models derived for the nominal male insect and a dramatically larger female.

6.1 Mechanosensory Feedback Variation

6.1.1 Feedback Variation Study

The desired outcome of this chapter is an understanding of how mechanosensory feedback can affect reduced order insect flight dynamics models. First, analytic

functions were written for the stereotyped wing kinematics of a dipteran insect. The kinematic functions were used along with an insect aerodynamics model in quasi-steady form in order to predict the instantaneous forces and moments applied to an insect body (Dickinson et al., 1999). The quasi-steady aerodynamics form, normally taken to be operating at a point, was extended to apply in the presence of egomotion. The equations of motion were posed as classical rigid body equations of motion, and linearized solutions determined.

To investigate the effect of mechanosensory feedback and the resulting control requirements, the insect models were derived both with and without control feedback provided by aerodynamically ineffective "hind wings" known as halteres, which are thought to encode rate information (Thompson et al., 2008). The haltere model used was the angular rate feedback with bandpass filtering used in Chapters 3 and 4.

6.1.2 Gain Variation Results

The results of Chapters 3 and 4 include reduced order models of the insect flight dynamics. The longitudinal motion of the example *Drosophila*-like insect was written as $\dot{\boldsymbol{x}} = A\boldsymbol{x} + B\boldsymbol{u}$, where $\boldsymbol{x}$ is the vector of longitudinal states composed of forward flight velocity u, heave motion w, pitch rate q, and pitch angle θ; and $\boldsymbol{u}$ is the vector of kinematic inputs composed of stroke amplitude Φ, stroke plane inclination β, and stroke bias ϕ_{off} as defined in Figure (6.1) The system dynamics

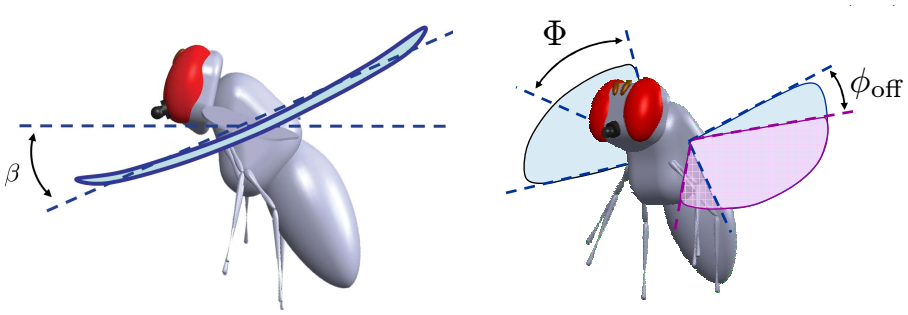

(a) Stroke plane angle (b) Stroke angle amplitude, offset.

Figure 6.1: Kinematic inputs definitions.

and control input matrices A and B may be written for the haltere-on case as

$$A = \begin{bmatrix} -12.33 & 0 & 0 & -9.81 \\ 0.0 & -4.651 & 0 & 0 \\ 547.0 & 0.0 & -33.26 & 0 \\ 0 & 0 & 1 & 0 \end{bmatrix} \tag{6.1}$$

$$B = \begin{bmatrix} 0 & 20.67 & 12.69 \\ -17.36 & 0 & 0 \\ 0 & -2826.0 & 6020.0 \\ 0 & 0 & 0 \end{bmatrix}. \tag{6.2}$$

The same procedure applied to the haltere-off dynamics also reduces the longitudinal motion to a linear time invariant system.

The ease with which a dynamic system (in this case an insect) naturally returns or diverges to a reference flight condition is described mathematically via the rigid body modes (characteristic motions) of the system and the associated modal poles.

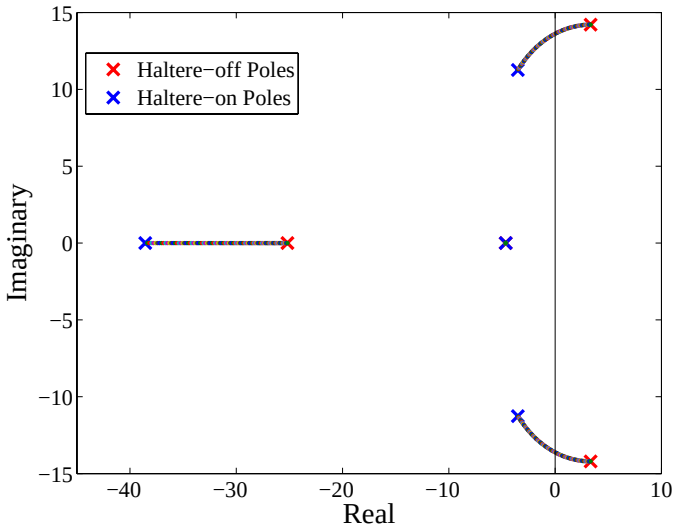

Figure 6.2: The stability properties of the insect dynamics are improved by haltere feedback, and a root locus plot over haltere gain shows pole movement to connect the systems.

In a pole-zero diagram, pole locations along the x-axis (real axis) represent the speed with which the particular motion either returns to the reference trajectory or diverges from it, and the y-axis (imaginary axis) locations quantify the amount of oscillation in the motion. The pole locations of the longitudinal system, seen in Fig 6.2, show that the insect with no haltere feedback (seen in red) has an unstable mode, but the pole locations of the haltere-on system (seen in blue) are stable.

The nonlinear haltere model used in simulation was a band pass filter fitted to data by Sherman and Dickinson (2004), but a simplified model of the haltere pitch rate feedback is $u = -kq$, where k is the gain of the haltere. Given the haltere off system dynamics A_{off}, the system dynamics matrix under increasing gain on the

halteres may be written as $A_{\text{on}} = A_{\text{off}} - BK$, where

$$K = \begin{bmatrix} 0 & 0 & 0 & 0 \\ 0 & 0 & 0 & 0 \\ 0 & 0 & k & 0 \end{bmatrix} \tag{6.3}$$

and the haltere-on matrix A is recovered at full haltere gain. In Fig 6.2, the simplified model for pole locations for under varying haltere gains indicates the progression from the unstable haltere-off system to the stable haltere-on system, and that the oscillation in the pitch and fore/aft degrees of freedom is reduced, while the decoupled pole (corresponding to heave damping) is unaffected by rate feedback.

Given that unstable systems are inherently more difficult to control than stable systems, linear systems analysis indicates that the addition of mechanosensory feedback in the form of haltere rate feedback can significantly reduce the insect's sensing and feedback requirements by providing a stabilizing effect on the motion in the pitch and fore/aft degrees of freedom.

6.2 Mechanosensory Feedback on CFD model

Section 6.1 investigated the effect of gain reduction on a linear system, showing a progression from stabilized (haltere-on) to the bare airframe instability. Dipteran insects possess mechanosensory feedback beyond the haltere feedback that has been measured experimentally and was modeled in the nonlinear simulation of Section 3.3. Since the computational fluid dynamics investigation in Chapter 5 suggests

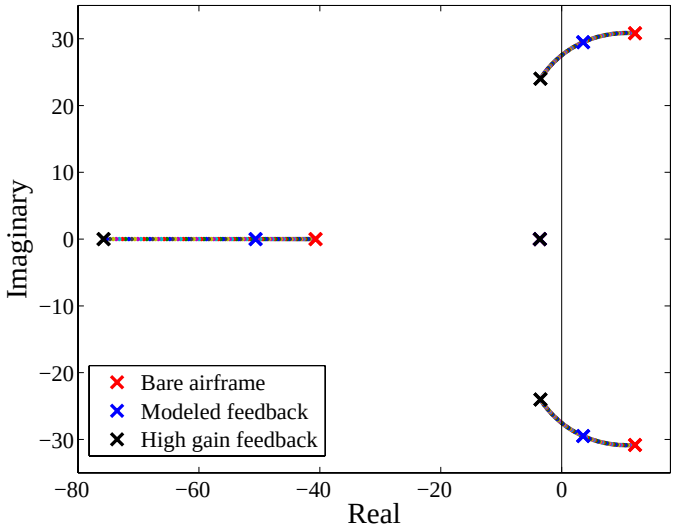

Figure 6.3: Stabilization of the CFD-derived system (in red) requires a higher pitch rate gain than than originally modeled (in blue). Equivalent convergence rate requires a gain 2.45 times larger (in black).

that reduced-order modeling underestimates the instability, the feedback required to stabilize the CFD-derived system could significantly exceed the feedback investigated for reduced order modeling. More recent work has suggested that other forms of sensing are thought to provide rate feedback as well, in particular ocelli (Rowell and Pearson, 1983). Ocelli are rudimentary eyes (illumination level detectors) that are well-suited for high angular rate measurement.

In order to quantify the additional mechansensory feedback required to stabilize the CFD system, a similar approach to section 6.1 was taken, using the longitidunal dynamics model with the haltere gain modeled as a linear feedback law $u = -Kq$ such that $A_{\text{cfd,on}} = A_{\text{cfd}} - BK$. Eigenvalue computation then shows that the modeled haltere pitch rate gain is insufficient to stabilize the CFD-derived system, and is only sufficient to move the unstable pole locations from $\texttt{Re}(\lambda) = +12.1$ to $+3.5$, as seen in Figure 6.3.

In particular, achieving marginal stability ($\texttt{Re}(\lambda) = 0$) requires a gain 1.57 times greater, but marginal stability is rarely implemented in practice. To achieve an equivalent convergence rate as the reduced order model ($\texttt{Re}(\lambda) = -3.5$), the CFD-derived system requires a pitch rate gain 2.45 times the originally modeled gain. This additional feedback suggests that the experimental measurements of haltere-mediated feedback have only quantified 41% of the mechanosensory feedback that is active on the insect, and that further experimentation to isolate other forms of feedback is necessary.

6.3 Parameter (Phenotypic) Variation

The genotypic limits on species such as *Drosophila* allow remarkable phenotypic plasticity. Environmental factors (e.g. ambient temperature) are relevant both during development and while mature, and morphology is highly dependent on both genetic limits and environmental factors. In animals kept at temperatures of 14 to 21°C, body mass varied from .9 mg to 1.8mg (Karan et al., 1998). The insect used for hover modeling, with its mass of $m = 1.02$ mg and wing length of $R = 2.12$ mm, uses parameters based on the males presented in the results of Karan et al. (1998); Crill et al. (1996). To compare how the results are affected by the larger (approximately 150%) morphology presented by a female insect, lateral-directional hover dynamics for a female *Drosophila*-like insect having a mass $m_f = 1.70$ mg and $R_f = 2.355$ mm was also system identified, and the results, shown in Table 6.1, indicate that the parameter variation generated by this relatively large morphological change is

Parameter	Value	Standard Dev σ	Insensitivity
Y_v	-13.44	6.63%	2.95%
L'_v	-9658	.07%	.03%
L'_p	-178	0.2053%	.09%
N'_r	-70.55	0.1648%	0.08%
L_{Φ_d}	-340.73	2.9%	1.3%
N_{β_d}	-28,080	3.9%	1.9%

Table 6.1: Control and stability derivative results for female *Drosophila*.

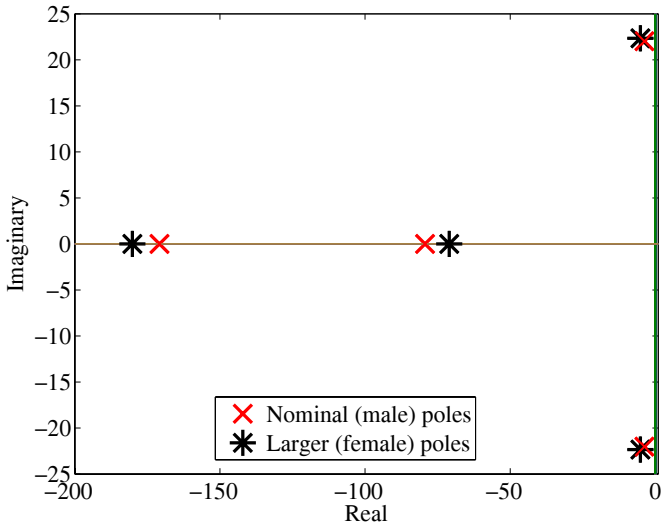

Figure 6.4: Comparison of the lateral-directional poles identified for the nominal (male) and larger (female) insect.

contained primarily in the control derivatives. Accordingly, the modal behavior of the system shows a relatively minor variation, as exhibited by the pole shift from $(\lambda_1, \lambda_{2,3}, \lambda_4) = (-73, -3.4 \pm 22.9i, -180.5)$ to $(-70.6, -5.2 \pm 22.2i, -181.1)$, seen graphically in Fig. 6.4.

6.4 Summary

In this chapter, the effect of a gradual reduction in mechanosensory feedback was considered, showing a progression from the stable haltere on system to the

unstable bare aiframe system. The feedback requirements of a system including detailed aerodynamic models were shown to be greater, requiring an increase in feedback gain by 2.45 times to achieve an equivalent convergence rate specification. Finally, the degree to which individual morphological differences within a species affect the dynamic properties of flapping flight were addressed by using the species' sexual dimorphism to consider insects at either end of the commonly observed size range for *Drosophila*. Differences were found primarily in the size of the control derivatives, but the modal structure was retained.

Chapter 7

Reachability Analysis

This dissertation has developed a set of kinematic programs suitable for maneuvering an insect or flapping wing micro air vehicle (MAV), and flight dynamics models to relate those inputs to the rigid body motion of the vehicle. In several cases, multiple inputs exist to effect the same desired trajectory. MAV design presents size, weight, and power limitations that reduce actuation capability. Given more inputs than necessary to control a dynamic model, one may consider the question of which inputs are "optimal" in some sense, either from the perspective of minimizing actuation effort for a given motion, or maximizing the set of all reachable states under a restricted input.

This chapter introduces a control theoretic framework to quantify the reachable states for a given set of inputs, and applies it to the hovering fruit fly model developed in Chapter 3. Controllability as an application of operator theory is the basis for determining the reachable configurations under a class of inputs. The expressions for reachable states may then be used to solve a least-squares optimization problem over all possible function inputs.

Previous analysis of insect-inspired flapping wing locomotion has examined wing kinematic trajectories from the perspective of maximizing lift(Avadhanula et al., 2003; Ansari et al., 2008) or minimizing required power (Berman and Wang,

2007). With the introduction of new tools to extract the detailed wingstroke to wingstroke kinematics of insects from high speed videography (Fontaine et al., 2009; Ristroph et al., 2009), a number of species-specific control strategies for maneuvering have been identified. In addition, with the development of micro-scale vehicles that can potentially generate lift forces greater than their weight (Wood, 2008), *stability and control* aspects of the problem have become an important research need.

Despite the critical need, the inherent complexity of small-scale flapping flight aerodynamics has obscured a control-theoretic analysis of both biologically relevant and engineered wing kinematic perturbation strategies. While the detailed aerodynamic mechanisms involved in small-scale flight are still an area of active research (Ramamurti and Sandberg, 2007), recent efforts have in fact yielded several approaches for extraction of reduced-order linear time-invariant flight dynamics, either for single degree of freedom experimental cases (Hesselberg and Lehmann, 2007), direct analytic methods (Doman et al., 2010a), or more general computationally (Sun et al., 2010) and spectrally derived models as presented in Chapters 3 and 4. Such formulations are amenable to application of linear control analysis tools, and should provide the next level of insight.

Reachability (or more traditionally, controllability) characterizes the amount of control one has over the state of a system through the choice of the input. This is an important topic for small-scale flapping wing MAV designers for several reasons. Size, Weight, and Power (SWaP) constraints are very stringent at this scale, and reductions in complexity that promote weight reduction or robustness are encouraged. In addition, these vehicles are intended to operate in gusty and possibly

cluttered environments, and a high level of platform maneuverability and actuation authority will be crucial to achieving robust flight path control in the face of these uncertainties.

This chapter explores the reachable state space associated with biologically-inspired kinematic control strategies seen in fruit fly longitudinal motion about hover (see Chapter 3 for development of the model). In Section 7.1 a frequency-based system identification methodology for identifying the stability derivatives of a small-scale flapping microsystem about hover is outlined, along with the control derivatives for biologically relevant wing kinematic perturbations for maneuvering. Section 7.2 applies controllability analysis tools to interpret these biologically-relevant control strategies for micro-air vehicle design, using the example of an MAV with *Drosophila*-like parameters.

7.1 Longitudinal Flight Dynamics Model

Previous chapters have outlined a method to formulate linear time invariant (LTI) flight dynamics models of the form

$$\dot{x} = Ax + Bu. \tag{7.1}$$

In this case $A \in \mathbb{R}^{n\times n}$ and $B \in \mathbb{R}^{n\times p}$ represent the state and input matrices, $u(t) \in \mathcal{U} \subset \mathcal{L}_2^p[0,\infty)$ the input time history and $x(t) \in \mathcal{X} \subset \mathcal{L}_2^n[0,\infty)$ the state history of the model.

The nominal (trim) kinematics are assumed to be a periodic oscillation $\phi(t)$

contained in a stroke plane inclined an angle β from horizontal, with the wing intersecting the stroke plane at an angle $\alpha_g(t)$. Biologically relevant control inputs considered in this study are shown in Fig 7.1 and defined as (a) *Stroke plane inclination* (Fry et al., 2003) β_c: a tilting of the stroke plane generating pitch moment and forward force, (b) *Stroke plane offset* (Fry et al., 2003; Oppenheimer et al., 2010; Doman et al., 2010b) ϕ_{off}: a fore/aft shift of the wing sweep used primarily to generate pitch moment, and (c) *Asymmetric wing angle* (Ristroph et al., 2009) α_{ud}: an upstroke/downstroke asymmetry in the angle of the wing relative to the stroke plane used primarily to generate forward force.

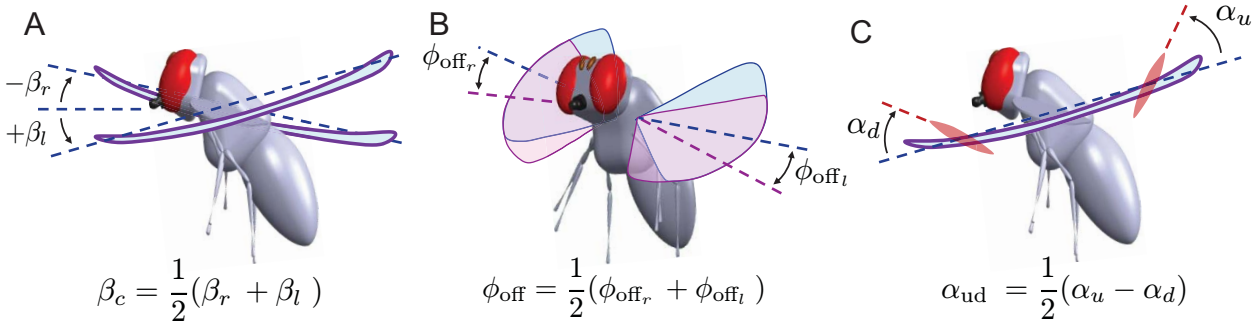

Figure 7.1: Longitudinal control inputs used in reachability analysis. (A) Stroke plane inclination β_c, (B) Stroke plane offset ϕ_{off}, and (C) Differential wing angle α_{ud}.

The stability and control derivatives in the flight dynamics model from Chapter 3 were selected to maximize coherence in the low frequency regions (up to 20 Hz), while discarding the small periodic high frequency motion. Note that with the haltere feedback about the pitch axis, the longitudinal system is stable and the matrix A is Hurwitz.

The general state space model structure for the longitudinal dynamics includ-

ing the control inputs listed above is given by

$$\begin{bmatrix} \Delta\dot{u} \\ \Delta\dot{w} \\ \Delta\dot{q} \\ \Delta\dot{\theta} \end{bmatrix} = \begin{bmatrix} X_u & 0 & 0 & -g \\ 0 & Z_w & 0 & 0 \\ M_u & 0 & M_q & 0 \\ 0 & 0 & 1 & 0 \end{bmatrix} \begin{bmatrix} \Delta u \\ \Delta w \\ \Delta q \\ \Delta\theta \end{bmatrix} + \begin{bmatrix} 0 & X_\beta & X_{\phi_{\text{off}}} & X_{\alpha_{\text{ud}}} \\ Z_\Phi & 0 & 0 & 0 \\ 0 & M_\beta & M_{\phi_{\text{off}}} & M_{\alpha_{\text{ud}}} \\ 0 & 0 & 0 & 0 \end{bmatrix} \begin{bmatrix} \Phi_c \\ \beta_c \\ \phi_{\text{off}} \\ \alpha_{\text{ud}} \end{bmatrix} \tag{7.2}$$

The general state space model includes an additional input, stroke amplitude Φ_c. Stroke amplitude affects only heave (Δw) dynamics and is decoupled from the other states and inputs.

7.2 Reachability Analysis

For the longitudinal flight dynamics (7.2), the goal is to have a rigorous framework in which to quantify the effectiveness of the biologically relevant control strategies (Fry et al., 2003; Ristroph et al., 2009) that have been described in the previous section. As the heave (Δw) dynamics and the collective stroke amplitude control input (Φ_c) are decoupled from the remaining states in the linearized model, the pitch/fore/aft dynamics ($\Delta u, \Delta q, \Delta\theta$) and control inputs ($\beta_c, \phi_{\text{off}}, \alpha_{\text{ud}}$) are considered without loss of generality.

Application of the controllability rank test for all possible combinations of control inputs reveals that the pitch/fore/aft system is fully controllable with any pair of the remaining control inputs, which motivates the examination of three input

pairs:

$$u_1 = \begin{bmatrix} \beta_c \\ \phi_{\text{off}} \end{bmatrix}, \quad u_2 = \begin{bmatrix} \beta_c \\ \alpha_{\text{ud}} \end{bmatrix}, \quad u_3 = \begin{bmatrix} \phi_{\text{off}} \\ \alpha_{\text{ud}} \end{bmatrix}. \tag{7.3}$$

In order to minimize actuator effort and maintain a small number of controls, we desire the pair of inputs that maximize the span of reachable states x_0 resulting from any arbitrary input $u(t) \in \mathcal{L}_2^p(-\infty, 0]$ of unit norm.

7.2.0.1 Controllability operator

Consider the linear system

$$\dot{x} = Ax + Bu, \tag{7.4}$$

with $A \in \mathbb{R}^{3x3}$ and $B \in \mathbb{R}^{3x3}$.

Definition 7.2.1 (Reachability) *The system* $\{A, B\}$ *is defined as* reachable *over the interval* $[t_0, t_1]$, $t_1 > t_0$ *if for every pair of states* $x_0, x_1 \in \mathcal{X}$, *there exists a control* $u(t) \in \mathcal{L}_2^p[0, \infty)$ *such that the solution of*

$$\dot{x} = Ax + Bu, \qquad\qquad x(t_0) = x_0$$

satisfies $x(t_1) = x_1$.

Following Corless and Frazho (2003); Dullerud and Paganini (2000) for a time invariant system, t_0 may be chosen arbitrarily. Choosing $t_0 = -\infty$, $t_1 = 0$, the solution

to eqn (7.4) is

$$x(0) = e^{-A\infty}x_0 + \int_{-\infty}^{0} e^{-A\tau}Bu(\tau)\,d\tau. \tag{7.5}$$

Define the operator Ψ from $\mathcal{U} = \mathcal{L}_2^p[0,\infty)$ to $\mathcal{X}$ as

$$\Psi u = \int_{t_0}^{t_1} e^{A(t_1-\tau)}Bu(\tau)\,d\tau$$

and for our choice of integration limits, Ψ operates from $\mathcal{L}_2^p[0,\infty)$ to $\mathcal{X}$ as

$$\Psi u = \int_{-\infty}^{0} e^{-A\tau}Bu(\tau)\,d\tau \tag{7.6}$$

Operator Ψ takes as an input a time history $u(t)$ and outputs a state x_0. More specifically, it returns the final state $x(0)$ corresponding to eqn (7.4) with initial condition $x(-\infty) = 0$ and forced by $u(t)$.

This view motivates a consideration of what input $u(t)$ returns a particular desired state $x(0) = x_1$. If the system is controllable, then $u(t)$ exists by direct application of the definition. However, Ψ maps an infinite dimensional space $\mathcal{L}_2^p[0,\infty)$ onto a finite dimensional space $\mathcal{X}$, thus its kernel has infinite dimension and $u(t)$ is not unique.

Given the non-uniqueness, one may consider the case of what $u(t)$ is "optimal." Consider the following least squares optimization problem for a (not necessarily controllable) system: Given the initial condition $x(-\infty) = 0$ and a desired final state x_1, find an input $\hat{u}(t)$ that satisfies

$$||\hat{u}(t)||^2 = \inf\left\{\int_{-\infty}^{0} ||u(t)||^2 dt \ : \ \hat{x}(0) = \int_{-\infty}^{t_1} e^{-A\tau} B u \, d\tau\right\}$$

where $\hat{x}(0)$ is the unique vector in $\mathcal{X}$ satisfying (7.7)

$$||x_1 - \hat{x}(0)|| = \inf\left\{||x_1 - x(t_1)|| : \dot{x} = Ax + Bu \text{ and } x(-\infty) = 0\right\}.$$

In the general case, the minimization problem is to find the input of least norm that drives the system as close as possible to the final state. The terminal condition in eqn (7.7) is always satisfied for a controllable system, where a $u(t)$ is known to exist and thus $\hat{x}(0) = x_1$.

For the controllable pair $\{A, B\}$, then

(i) the matrix $\Psi\Psi^* =: X_c$ is nonsingular, and

(ii) for any $x_1 \in \mathcal{X}$, the input $\hat{u}(t) = \Psi_c^* X_c^{-1} x_1$ is the element of minimum norm in the set

$$\{u \in \mathcal{L}_2^p[0, \infty), \Psi u = x_1\}.$$

For a detailed proof of (i) and (ii), see Dullerud and Paganini (2000).

7.2.1 Reachable space under unit norm input

In the process of MAV control design, a measure of how "far" inputs may drive the system in the configuration space can assist the choice of a control strategy. Mathematically, the configuration space that is reachable under unit norm input,

expressed as

$$\{\Psi u : u \in \mathcal{L}_2^p[0,\infty) \text{ and } ||u(t)|| \leq 1\}$$

is equivalent to

$$\mathcal{E}_c = \left\{ X_c^{\frac{1}{2}} x_c : x_c \in \mathcal{X} \text{ and } ||x_c|| \leq 1 \right\}.$$

To verify the equivalence, one may show that each set is contained in the other. $\mathcal{E}_c$ defines an ellipse in $\mathbb{C}^n$ whose geometric properties are determined by the infinite-time controllability gramian X_c for the system (7.2),

$$X_c \;=\; \Psi_c \Psi_c^* \;=\; \int_0^\infty e^{A\tau} B B^* e^{A^*\tau}\, d\tau \;\geq 0, \tag{7.8}$$

which can be computed given the matrix pair (A, B) via the Lyapunov equation,

$$AX_c + X_c A^* + BB^* = 0. \tag{7.9}$$

The principle axes and lengths of $\mathcal{E}_c$ are given by the eigenvectors and eigenvalues of $X_c^{\frac{1}{2}}$, respectively, which motivates two control input ranking criteria. The first is the Frobenius norm of $X_c^{\frac{1}{2}}$,

$$||X_c^{\frac{1}{2}}||_F = \sqrt{\text{trace}\left[(X_c^{\frac{1}{2}})^* X_c^{\frac{1}{2}}\right]}, \tag{7.10}$$

whose geometric interpretation is the square root of the summed squares of the axes lengths of $\mathcal{E}_c$. Second, since $X_c \geq 0$, one can also consider the volume $\det(X_c^{\frac{1}{2}})$ of $\mathcal{E}_c$ as a non-negative measure of its size. Choosing control degrees of freedom

that maximize either of these measures then corresponds to maximizing the set of reachable states over the choice of control degrees of freedom.

The controllability ellipsoids of the input pairs are shown in Fig. 7.2A-C, indicating that the reachable space for a unit norm input increases significantly from input pair u_1 through u_3. For comparison, the reachable configuration space for a unit norm input on all three control terms $(\beta_c, \phi_{\text{off}}, \alpha_{\text{ud}})$ is shown as u_4 in Fig. 7.2D. The results of applying the two ranking criteria to the control input selections u_1 through u_4 are shown in Table 7.1 and plotted in Fig. 7.3. Out of the three pairs, clearly $u_3 = (\phi_{\text{off}}, \alpha_{\text{ud}})$ provides the most authority over the longitudinal dynamics. In terms of the reachable volume measure, u_3 provides a 672% increase over u_1 and a 38% increase over u_2. In addition, utilizing all three control inputs u_4 only provides for a modest 6% increase in reachable volume over u_3. Similar conclusions follow from the Frobenius norm ranking criteria; u_3 provides 94% and 11% increases over u_1 and u_2 respectively, whereas u_4 adds a 2% improvement over u_3.

The ellipsoidal interpretation also yields important information regarding the resulting system's controllability along particular directions in state space. In the case of Fig. 7.2, the rotational dominance of the control inputs (and modes) is evident in the larger reachable configuration space along the pitch rate/angle axes, while the range of forward speed is more limited.

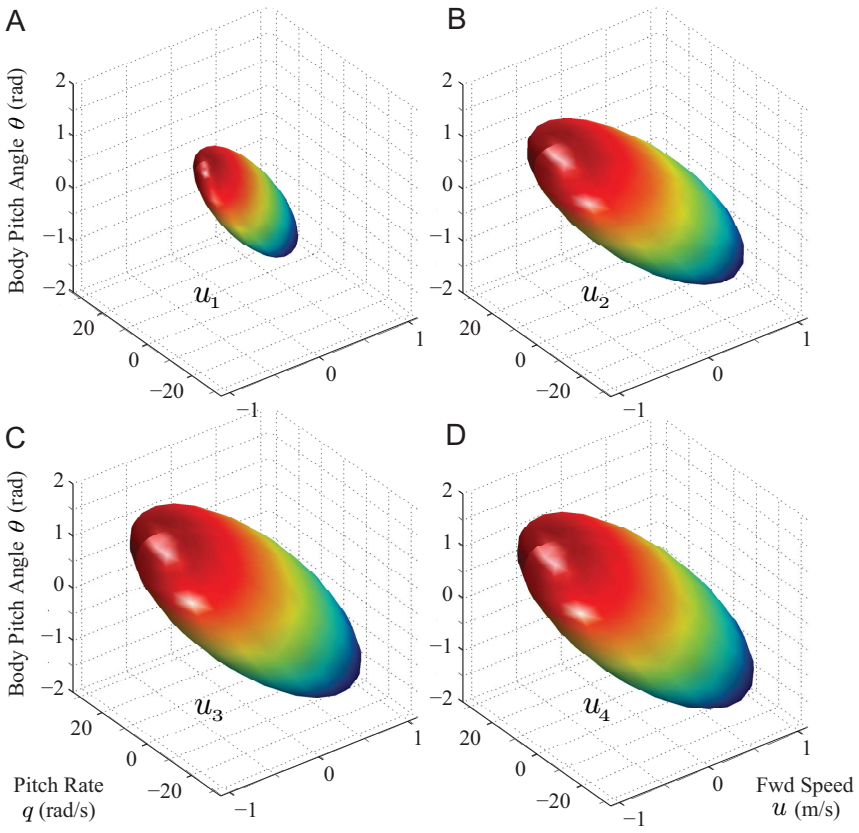

Figure 7.2: Controllability ellipsoids for the input combinations illustrate the reachable configurations under the restriction $||u_i|| \leq 1$. Input combinations u_1 through u_3 are pairs of control terms, while u_4 considers all 3 control terms $(\beta_c, \phi_{\text{off}}, \alpha_{\text{ud}})$.

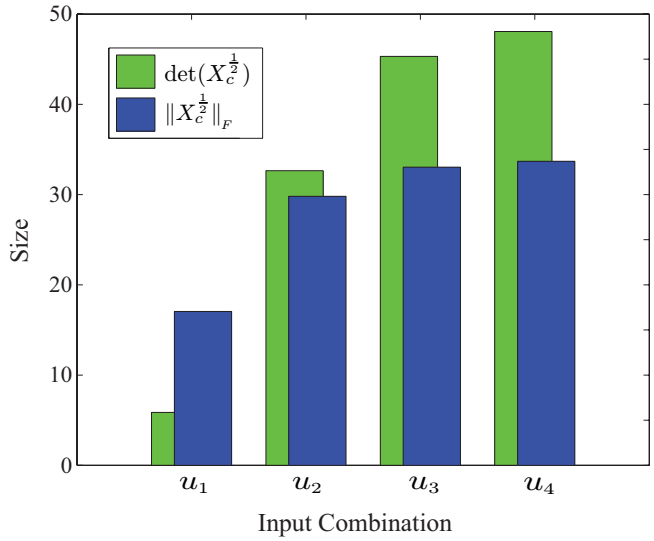

Figure 7.3: Controllability of input combinations u_1 through u_4, as ranked by the determinant or Frobenius norm of the square root of the controllability gramian.

Input	u_1	u_2	u_3	u_4
$\det(X_c^{\frac{1}{2}})$	5.87	32.65	45.31	48.06
$\|\|X_c^{\frac{1}{2}}\|\|_F$	17.04	29.80	33.03	33.69

Table 7.1: Control input performance ranking criteria for u_1 though u_4.

7.3 Summary

This chapter introduces a control-theoretic framework and two performance measures to quantify the state reachability for a given choice of biologically inspired wing kinematic control parameters, allowing for a set of candidate control strategies to be ranked. The work presented here leverages the *Drosophila melanogaster* linear time-invariant (LTI) flight dynamics models previously developed in this dissertation.

For the example insect-size micro air vehicle (MAV) considered, all four of the input combinations provided full controllability, but the reachable space is dramatically improved through proper selection of the input combinations. The kinematic set that provided the most controllability involved a stroke bias term (ϕ_{off}) and an angle of attack difference in the upstroke and downstroke (α_{ud}), which improved the reachable volume of state space 672% over the least controllable set. Moreover, while the reachable space is dramatically improved over each of the input pairs, only a slight advantage is found by combining all three inputs; adding a stroke plane angle degree of freedom (β_c) to the most effective pair resulted in only a modest increase (6%) in the volume of reachable state space.

The framework and performance measures introduced in this note provide a means to appropriately choose kinematic inputs that minimize the required control

energy and maximize the achievable state space of the system. These tools can be applied to reduce actuator complexity to promote robustness and weight reduction, resulting in improved size, weight, and power (SWaP) requirements for micro-air vehicle flight stability and control. For MAV design, factors other than control energy (such as actuator geometry) may be the limitation on kinematic actuation, and a system-level approach must be used to determine the limiting factor. The framework introduced in this chapter is directly applicable for a systems level model to be used in MAV design studies.

Chapter 8

Forward Flight Dynamics

This chapter uses the *Calliphorid* kinematic measurements of Chapter 2 and the approach developed in Chapter 3 and 4 to determine forward flight dynamics models for dipteran flight, as opposed to the hover-oriented fruit fly models presented previously.

8.1 Background

This dissertation has investigated hovering flight dynamics for dipteran flapping flight. An example *Drosophila melanogaster* was built up using nominal kinematics for hover, an experimentally-derived aerodynamic model, and frequency-based system identification on a rigid body dynamics simulation. Analysis of the models led to conclusions about sensing and feedback requirements in hover. However, considerable research has been conducted on insect visuomotor responses in an effort to understand insect navigation and guidance algorithms. A concise forward flight dynamics model would allow researchers to place the feedback measurements into the context of navigation and guidance, and to understand why insects measure non orthogonal quantities. With experimental models under development that include rigid body rotation and translation (Dickson et al., 2010), researchers are approaching the capability to compare forward flight data with modeling results.

Chapters 3 and 4 presented a method of deriving flight dynamics models about hover, and a natural extension of this work could be to look at the flight dynamics about another reference condition. This chapter uses the same approach to investigate the longitudinal and lateral-directional dynamics of blowflies in forward flight, and present an expectation for the results of high fidelity experimental and computational measurements.

Biological kinematics may also play a significant role in flight stabilization. Experimental evidence has indicated that dipteran insects in forward flight may have turn rate limitations that are theorized to be correlated to aerodynamic mechanisms (Buelthoff et al., 1980). While fixed-wing flight is governed by aerodynamic mechanisms such as wing, fuselage, and tail interaction (Nelson, 1989), a dipteran flapping vehicle's primary aerodynamic component is its wings and small changes in wing kinematics have a dramatic effect on the maneuvering of the vehicle. In forward flight, many insects employ differing wing pitch angles in the fore and aft strokes, typically reducing the morphological angle of attack in the forward stroke and increasing it in the retreating stroke (Zanker and Gotz, 1990; Taylor and Thomas, 2003a,b). This upstroke/downstroke asymmetry may be an attempt to preserve a constant angle of attack or a physiological limitation (Zanker, 1990), but it may also have ramifications on the control requirements of forward flight. This chapter will also examine the effect of the wingstroke perturbation in lateral-directional flight.

8.1.1 Previous Work

Previous work on forward flight dynamics modeling has been limited. Data were collected for tethered *Orthoptera* over which airflow was forced (Taylor and Thomas, 2003a,b), to simulate forward flight. Linear time invariant system theory was used to analyze the resulting behavior but the effect of the insect's control structures (which were active) were not addressed. Experimental apparatus capable of both flapping and egomotion are under current development, and this is expected to soon become a research focus. There is a need for reduced order models with which to interpret the data collected in this emerging research area.

8.2 Longitudinal Flight Dynamics Modeling

This section presents the longitudinal flight dynamics modeling, including the effect of the more complex α_g function defined in Chapter 2.

8.2.1 Kinematics

For this study, untethered *Calliphorid* flies in straight and level forward flight at a mean cruise of 2.17 m/s were used to determine stereotypical forward flight wing kinematics, as measured in Chapter 2. Note that the wingstroke has differing wing pitch on the fore and aft strokes. Mean α_g values in each stroke are 58.7° and 54.0°, shown in Fig 8.1. These kinematics are defined as trim inputs, and perturbations about those kinematics are used to maneuver a simulated insect in forward flight. Again, symmetry allows right and left wing motions to be parameterized by

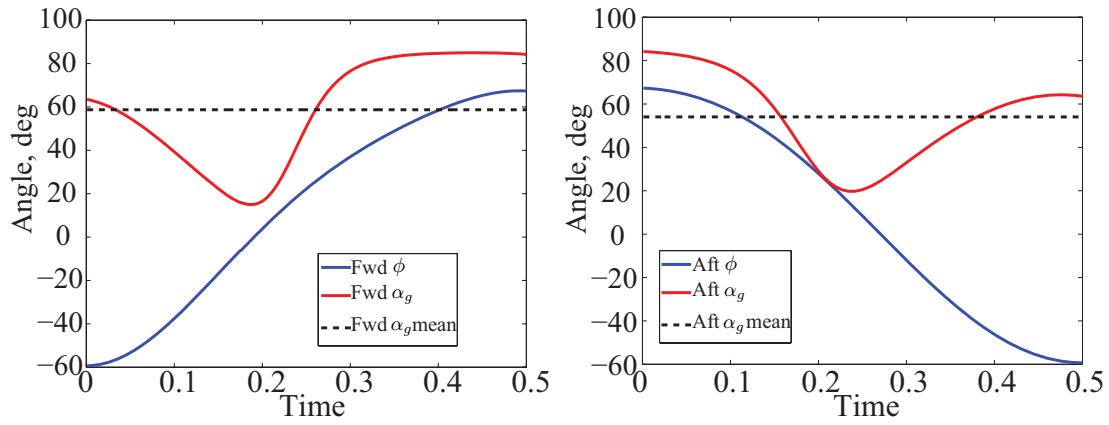

(a) Fwd (b) Aft

Figure 8.1: Kinematics in forward and aft strokes.

longitudinal (collective) motions.

8.2.2 Aerodynamics

There are indications that forward flight will require further modifications to the experimental aerodynamics model (Dickson and Dickinson, 2004). In this dissertation, the aerodynamics model has been placed in the context of insect body translation and rotation. Here we derive control-oriented models under the assumption that the aerodynamics model including egomotion is valid for cruise flight. When high fidelity data is available, either via computational solutions like those in Chapter 5 or experimental equipment, the validity of this assumption will be investigated and a similar aerodynamics model validated in forward flight may be applied.

8.2.3 Rigid Body Dynamics and System Identification

Rigid body dynamics and system identification is not affected by the linearization about a different reference flight condition, thus simulation and system identifications may be conducted as before.

The *Calliphorid* insect was first trimmed at $\phi_{\text{off,c}} = 14.375°$, $V_{\text{north}} = 2.18m/s, V_{up} = .06m/s, \gamma = 1.58°, u = 2.18m/s,$. Then, 60 second frequency sweeps were applied including frequency content up to 50 Hz. Longitudinal input sweeps were conducted for β_c,$\phi_{\text{off,c}}$, and Φ_c. However, system identification of the unstable system dynamics was complicated by the need to apply high gain feedback to stabilize the pitch dynamics, which reduces the signal to noise ratio of the identified transfer function by introducing correlated signals into the input.

The identified forward flight longitudinal dynamics model is

$$A = \begin{bmatrix} -1.32 & 0 & 0 & -9.81 \\ 25.2 & -24.7 & 0 & 0 \\ 1011.0 & -341.0 & -12.6 & 0 \\ 0 & 0 & 1.0 & 0 \end{bmatrix} \tag{8.1}$$

$$B = \begin{bmatrix} 71.9 & 13.7 & -2.86 \\ 320.0 & 60.9 & 0 \\ -0.0357 & -2211.0 & 5955.0 \\ 0 & 0 & 0 \end{bmatrix}. \tag{8.2}$$

This system has poles at $4.8072 \pm 17.0857i$, -32.6466, and -15.5768, mirroring

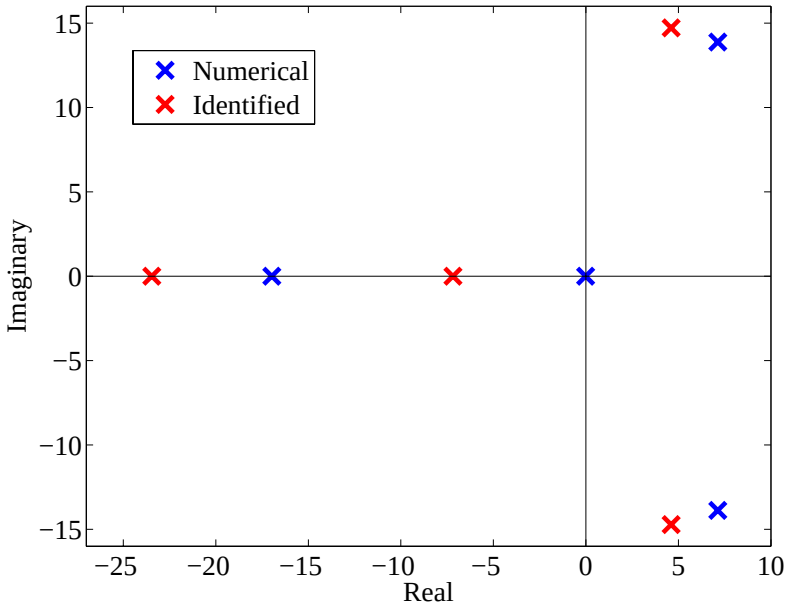

Figure 8.2: The pole structure of is similar to those in hover, with a real heave mode, and a coupled rotationally dominated triple that includes an unstable oscillatory pair.

the previous structure, with two real subsidence modes and unstable oscillatory pair, as seen in Fig. 8.2. The transfer function plots (see Fig 8.3 and 8.4) and fit convergence criteria indicate that the traditional model structure leads to error in the heave w dynamics. Table 8.1 presents state-space derivatives for the plots, uncertainties lower than 10% for all but the heave and Φ axes, indicating again that model structure refinements will be necessary.

8.3 Lateral-Directional Forward Flight Dynamics

In this section, lateral models are derived for forward flight. The models include differing wing pitch angles on the advancing and retreating wingstrokes, an input strategy observed in experimental studies (Zanker, 1990). This section introduces reduced order models for roll and yaw dynamics in forward flight and

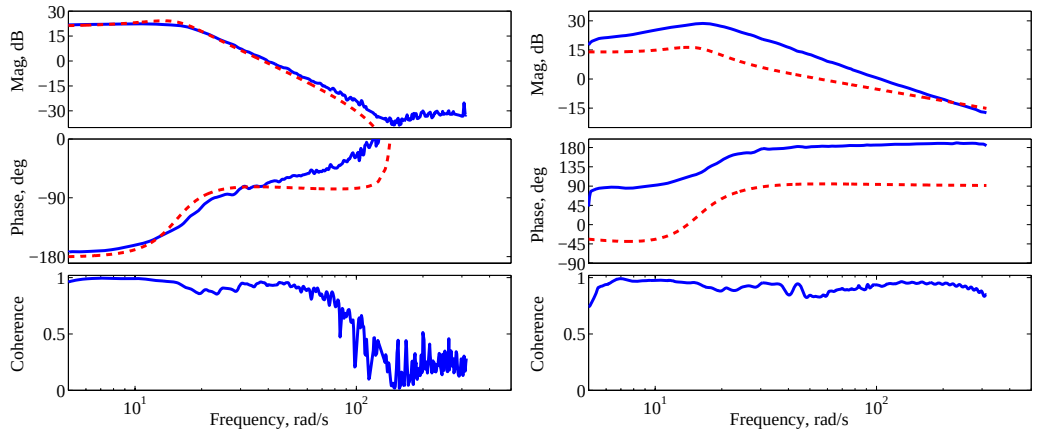

(a) ϕ_{off} to u (b) ϕ_{off} to w

(c) ϕ_{off} to q (d) ϕ_{off} to θ

Figure 8.3: A 4 state linear system ϕ_{off} transfer function shows good agreement for all but the heave direction, which shows model structure error.

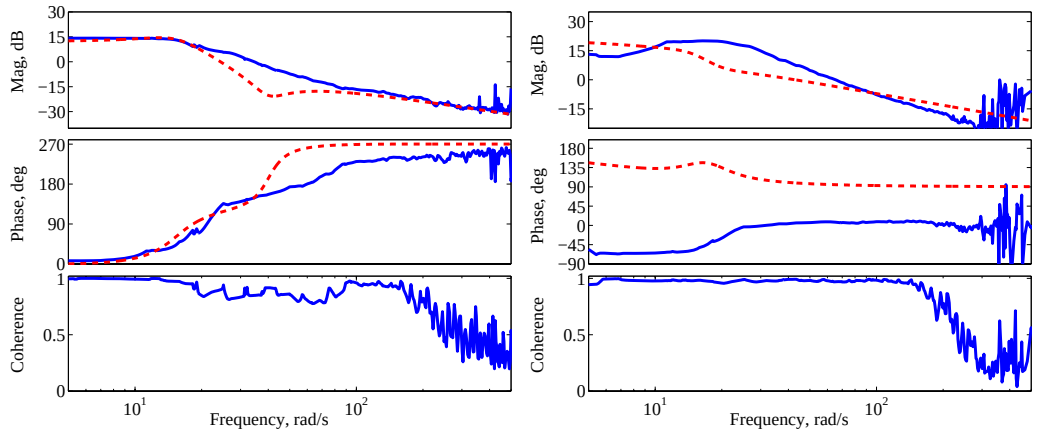

(a) β to u

(b) β to w

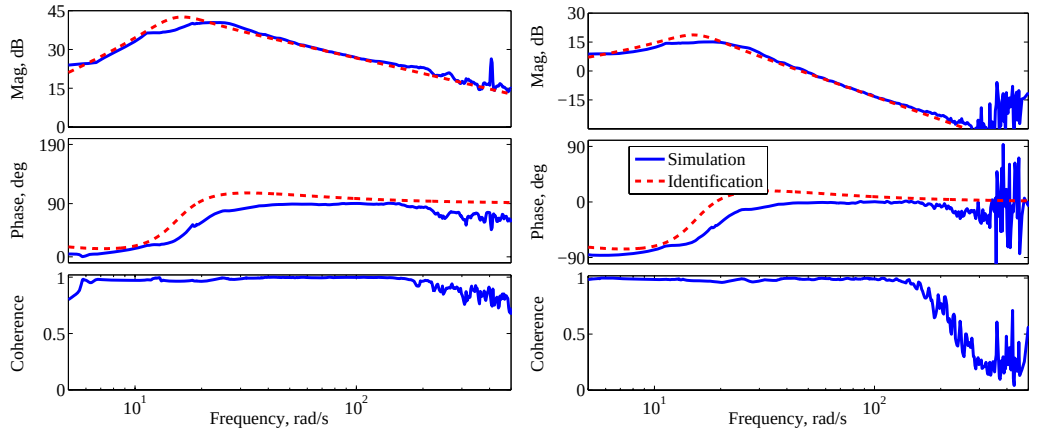

(c) β to q

(d) β to θ

Figure 8.4: A 4 state longitudinal linear system β transfer function shows good agreement for all but the heave direction, which shows model structure error.

Parameter	Value	Cramer Rao %
X_u	-1.605	5.638
Z_u	-8.590	5.756
Z_w	-7.433	7.300
M_u	569.1	1.749
M_w	17.29	87.98
M_q	-12.39	4.110
X_β	13.20	5.267
$X_{\phi_{\text{off}}}$	-2.945	4.469
X_Φ	33.04	11.46
Z_β	-44.06	5.315
$Z_{\phi_{\text{off}}}$	-55.00	2.763
Z_Φ	-4.661E+03	177.0
M_β	-2.175E+03	5.492
$M_{\phi_{\text{off}}}$	6.129E+03	1.462
M_Φ	2.816E+03	17.58

Table 8.1: Uncertainty values in the parameters are acceptable, with the exception of the w derivatives that poorly identified.

investigates how the upstroke/downstroke kinematic asymmetry can act to reduce the sensing and control requirements in forward flight by appropriately coupling lift and drag components in a turn. To derive the equations of motion, the insect body was modeled as rigid, allowing Euler rigid body dynamics to be applied. After a trim solution was determined that would provide a forward flight condition, the aerodynamic forces and moments as calculated by the experimental aerodynamics model were applied to the vehicle, which was constrained to motion at varying forward speeds from $u = 0$m/s to 2m/s but allowed to move about the axis of interest (roll or yaw) as dictated by aerodynamics to yield linear models. In contrast to earlier studies, no visual or mechanosensory feedback terms were included and the modeling represents bare airframe response.

8.3.1 Kinematics and System Identification

The nominal angle of attack pattern used to derive a lateral-directional flight modely is a modified square wave. Insects in forward flight commonly apply a decrease in wing pitch in the forward stroke and an increase in the aft stroke, which is modeled as a bias (or offset) term α_{ud} applied to the angle of attack pattern in forward flight. Experimental studies (Zanker, 1990; Zanker and Gotz, 1990) have indicated that diptera typically use negative values of α_{ud} in forward flight. The wing pronation/supination for this study is given by

$$\alpha_{g,r}(t) = 45^\circ \tanh\left[2.7 \sin\left(2\pi\ ft + \psi\right)\right] + \alpha_{\text{ud,r}} \tag{8.3a}$$

$$\alpha_{g,l}(t) = 45^\circ \tanh\left[2.7 \sin\left(2\pi\ ft + \psi\right)\right] + \alpha_{\text{ud,l}}, \tag{8.3b}$$

where r and l subscripts correspond to right and left wings.

With suitable parameterizations for stroke ϕ and wing pitch α angles, the control inputs may be considered the stroke amplitude Φ, offset ϕ_{off}, and pitch asymmetry α_{ud}. As before, right and left inputs are decomposed into collective and differential inputs using eqn (3.2).

To facilitate reduced order modeling, linear models were generated from time histories created by the simulation described in Chapter 3. The time histories used for analysis were generated by application of frequency sweeps from 0.1 Hz to 32 Hz to the Φ_d and β_d inputs to excite roll and yaw dynamics, respectively. The spectral content of the input $G_{xx}(\omega)$ and output $G_{yy}(\omega)$ (calculated by the chirp z

transform may be used to find the transfer function G describing the input/output relationship. The linear models generated represent the relationship between the signals in Fig 3.7 and are directly applicable to estimating the sensing and control feedback requirements of dipteran forward flight.

8.3.2 Results and Discussion

8.3.2.1 Roll dynamics

Passive aerodynamic mechanisms act to damp out roll rate via changes in angle of attack, as discussed in Section 4.5.2.2. Application of equation (4.1) to the chirp signals simulated for the example *Calliphora* insect allows computation of the transfer function seen in Fig 8.5, computed for the trimmed forward flight speed of 2m/s. Our desired result for roll dynamics is a model of the form $\dot{x} = Ax + Bu$:

$$\frac{d}{dt}\begin{bmatrix} p \\ \phi \end{bmatrix} = \begin{bmatrix} L_p & 0 \\ 1 & 0 \end{bmatrix}\begin{bmatrix} p \\ \phi \end{bmatrix} + \begin{bmatrix} \text{Ł}_{\Phi_d} \\ 0 \end{bmatrix}\begin{bmatrix} \Phi_d \end{bmatrix}. \tag{8.4}$$

The excellent coherence over a large portion of the frequency range of interest (0.1 to 32 Hz) indicates largely linear behavior, and a linear system has been fit to the transfer function in Fig 8.5. Time domain verification conducted using repeated doublets, typically a demanding input signal, shows excellent agreement, seen in Fig 8.6.

The roll dynamics terms are only slightly changed when the identification was repeated at differing forward velocities. Table 8.2 summarizes the small variations

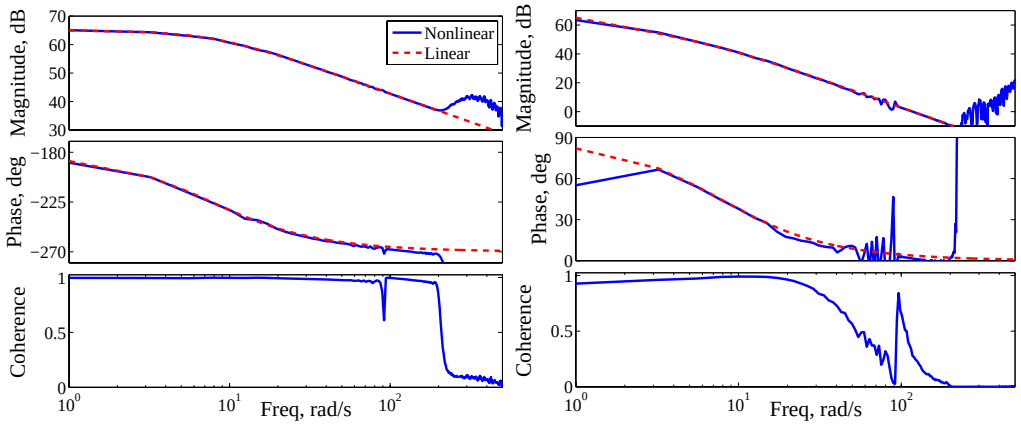

(a) Roll rate p (b) Roll angle ϕ

Figure 8.5: In forward flight $u = 2$ m/s, first order linear roll damping is an acceptable spectral description of the roll transfer function.

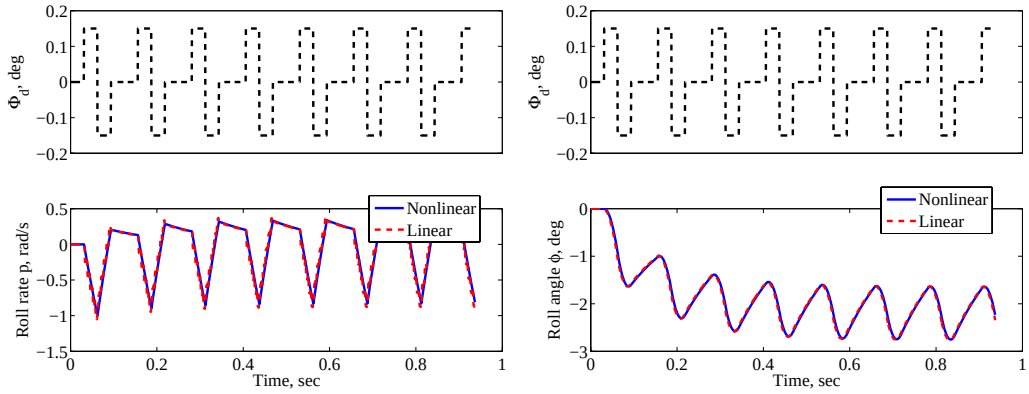

(a) Roll rate p (b) Roll angle ϕ

Figure 8.6: Time-domain agreement of the response to Φ_d input doublets in forward flight is excellent.

Speed u	Parameter	Value	Standard Dev. σ	Insensitivity
0m/s	L_p	-7.07	8.0%	3.0%
	L'_{Φ_d}	-13400	5.0%	1.9%
1m/s	L_p	-7.37	8.0%	3.0%
	L'_{Φ_d}	-13692	5.0%	1.9%
2m/s	L_p	-7.72	8.0%	3.0%
	L'_{Φ_d}	-13822	5.0%	1.9%

Table 8.2: Uncertainty estimates for parameters in the identified dynamics model show that roll damping and roll authority is only weakly affected by increasing u.

Speed u	Parameter	Value	Standard Dev. σ	Insensitivity
0m/s	L_r	-5.71	8.6%	3.5%
	L'_{β_d}	-2995	4.8%	1.9%
1m/s	L_r	-5.26	8.7%	3.6%
	L'_{β_d}	-3160	4.7%	1.9%
2m/s	L_r	-6.16	8.2%	3.2%
	L'_{β_d}	-4294	4.8%	1.9%

Table 8.3: Yaw control authority increases slightly with forward speed, while yaw damping is relatively unaffected.

in forward flight and uncertainty estimates.

8.3.2.2 Yaw dynamics

Experimental evidence has indicated that yaw damping is well modeled by a first order linear relationship (Dickson et al., 2010; Hedrick et al., 2009). A similar procedure to part 8.3.2.1 was applied to find transfer functions for yaw motions in forward flight, seen in Fig 8.7. Equivalent linear damping and control effectiveness terms were also found for the three reference flight speeds (Table 8.3). The results indicate that while yaw damping is relatively unaffected by forward flight speed, yaw control effectiveness increases with speed.

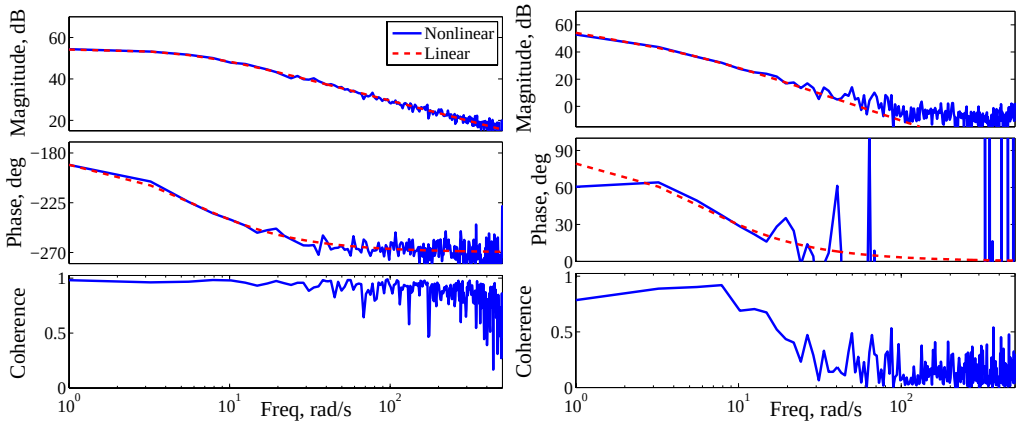

(a) Yaw rate r (b) Yaw angle ψ

Figure 8.7: Yaw dynamics transfer function fit at $u = 0$m/s.

8.3.2.3 Roll/Yaw Coupling (Proverse Yaw)

While single input single output models can yield significant insight into how roll and yaw damping change with forward speed, aerodynamic roll/yaw coupling may exist in forward flight. As an example, the adverse yaw tendencies of fixed-wing aircraft increase pilot workload, which has motivated the development of differential ailerons and mechanical or electrical interconnections to reduce adverse yaw tendencies. In particular, an insect that must support additional neurological structure to counter adverse yaw tendencies may be less able to survive robustly in the wild. If passive aerodynamics can assist in turn coordination, the sensing and control feedback necessary for dipteran flapping wing flight is reduced.

Roll/yaw coupling in forward flight shows that a roll motion in forward flight induces a yaw motion in the same direction, acting to coordinate the turn, as seen in Fig 8.8. Furthermore, the magnitude of the induced yaw motion varies from 1/500 of the roll rate at $\alpha_{\text{ud}} = 6°$ to 1/3 the roll rate as a function of the input $\alpha_{\text{ud}} = -6°$.

The physical mechanism of turn coordination can be understood by reference to the lift and drag polars of the quasi-steady aerodynamics form (Sane and Dickinson, 2002), where a differential change in angle of attack on each wing also affects the drag components of each wing to create a yaw moment in the same direction.

The finding that an insect with negative α_{ud} values (wing pitch reduced on the forward stroke) in forward flight receives turn coordination from passive aerodynamic behavior suggests that the kinematic perturbations seen in forward flight also act to reduce the control requirements during turning behavior.

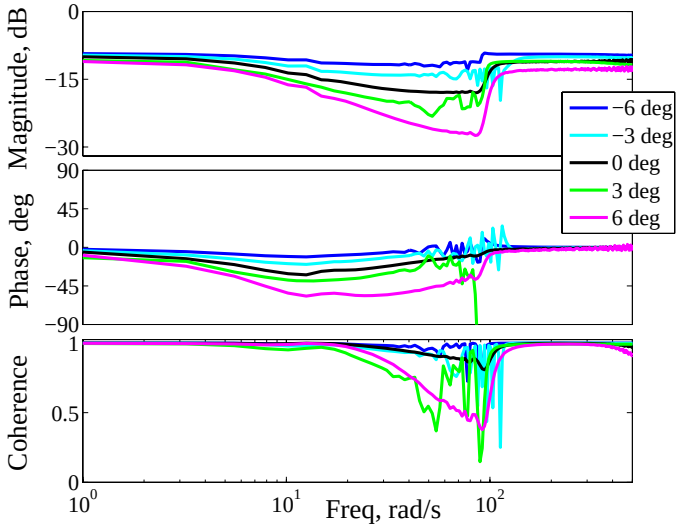

Figure 8.8: Roll rate to yaw rate coupling at 2m/s for differening wing pitch input α_{ud}. Roll motions in forward flight induce smaller yet potentially significant yaw rates. The magnitude of the induced yaw rate is a function of α_{ud}.

8.4 Summary

This chapter investigated the longitudinal and lateral-directional flight dynamics of dipteran forward flight. Due to instabilities, the identification was conducted

while a stabilizing controller was running. The longitudinal model showed good agreement for the rotational inputs, but the model structure that was appropriate for hover did not meet convergence criteria in forward flight, particularly in the heave dynamics. Nonetheless, the pole structure associated with the longitudinal dynamics was qualitatively similar to that in hovering flight, with two stable real poles and an unstable oscillatory pair.

Lateral-directional studies examined roll and yaw dynamics during constrained forward flight. In agreement with previous work, linear models were found to be sufficient to describe the roll and yaw dynamics for the example *Calliphora* insect (Dickson et al., 2010; Hedrick et al., 2009). Roll and yaw damping were similar for the three flight cases considered, $u = 0, 1, 2\text{m/s}$, while yaw control authority increased with forward speed. The study also examined the upstroke/downstroke asymmetry seen in the wing pitch angle during forward flight. The insect aerodynamics model predicts that the kinematic input provides a roll-to-yaw coupling through passive aerodynamic mechanisms. The roll-to-yaw coupling can assist in providing turn coordination, reducing the active control that an insect's neurological structure must support. The kinematic input α_{ud} may be similarly used in design to reduce the flight control demands of a dipteran flapping wing micro air vehicle (MAV) operating in forward flight, and thus reduce its size, weight, and power requirements.

Chapter 9

Conclusions and Future Work

9.1 Conclusions

In this dissertation, a path for developing reduced order flight dynamics models for dipteran flapping wing insects was presented. The analysis began with experimental measurement and characterization of wing kinematic motions through automated processing of high speed video. The wing kinematic motions were used with an empirically derived insect-scale aerodynamics model including state perturbations. Rigid body dynamics and system identification were applied to generate reduced order models for insects in hover and in forward flight, using as examples *Drosophila melanogaster* and *Calliphorid* flies. The effects of mechanosensory feedback on the flight dynamics were also determined, showing that biologically observed rate feedback paths are appropriate for flight stabilization. Results were compared to a numerical Navier-Stokes aerodynamic solution to determine the effect of the unmodeled aerodynamics, finding that the unmodeled aerodynamics increase the rate of response, and thus the required control. Within-species morphological differences were studied, finding very similar flight dynamics between large females and small males. A framework for determining the reachable configuration space associated with kinematic input programs, and methods for ranking the input programs in terms of highest maneuverability was presented.

The work presented is both relevant to understanding the sensing and feedback paths that are active in flying insects and to the design of micro air vehicles. Insects solve the flight stabilization and control problem in a manner that requires only small, specialized control structures that perform the essential feedback requirements by measuring composite quantities along non-orthogonal axes. An engineering means to replicate this on micro air vehicles will provide a dramatic increase in the mobility of small scale aerial robotics.

9.2 Dissertation Contributions

This dissertation examines insect flight dynamics modeling and contributes the following to the field:

- **Kinematics:** The first detailed measurement of both trim and maneuvering wing kinematics for *Calliphorid* flies were made. Curve fits to the nominal kinematics provide stereotyped kinematics, while perturbations to the kinematic parameters serve as control inputs for flight dynamics modeling. While previous research quantified only errors inherent in the digitization measurement, reference models were used to quantify the accuracy of the full measurement path. A kinematic perturbation α_{ud} was quantified in forward flight.

- **Aerodynamics:** This dissertation introduced a method of placing the contemporary insect aerodynamics models in the context of insect body translation and rotation. Previously, the aerodynamics models were posed in quasi-steady form and did not include any state dependence, which prevents dynamic

analysis. When placed in the context of insect egomotion, the aerodynamic model now allows estimation of dynamic behavior.

- **Flight Dynamics Models:** Transfer functions for longitudinal and lateral-directional hovering flight dynamics of *Drosophila* were generated by spectral transformation of input and output time histories of a nonlinear simulation. Linear time-invariant (LTI) state space models were fitted to the transfer functions as well, allowing convenient analysis and simulation, and directly identify the form and rate of feedback required for stabilization. The use of LTI modeling was supported by linearity measures (coherence). Models were fitted up to 500 rad/s (89 Hz) for both fruit and blow flies, though coherence was degraded in many transfer functions over 200 rad/s (30Hz).

- **Model Validation:** Collaborative work with the authors of Bush, B. et al. (2010) compares the results of the dynamics modeling with the numerical solutions to the Navier-Stokes equations of motion, finding excellent agreement in translational derivatives, while improvement is suggested in rotational modeling.

- **Feedback:** The dynamic properties of the flight dynamics models under biologically-modeled rate feedback was investigated, finding that haltere feedback is sufficient to stabilize the insect, but that unsteady aerodynamics introduce instabilities that require 2.45 times the gain originally modeled to achieve an equivalent level of stability.

- **Morphology:** Hovering flight dynamics are found to be similar for large and small *Drosophila*, suggesting that individual morphological changes, which are commonly observed, do not present significantly different control demands.

- **Forward Flight:** This dissertation presents transfer functions for longitudinal and lateral-directional *Calliphorid* flies maneuvering about forward (cruise) flight. The pole structure for *Calliphorid* longitudinal forward fright dynamics is qualitatively similar to hovering *Drosophila*, with two stable real poles (one of which is a decoupled heave pole) and an unstable oscillatory pair. The kinematic perturbation α_{ud} gives rise to proverse roll/yaw coupling in forward flight, which can reduce feedback requirements.

- **Reachability:** Results from control theory are applied to calculate the reachable states with a given choice of inputs. Quantifying the reachable space leads to a method of ranking inputs and allows for intelligent choice of inputs for an MAV to maximize the reachable space.

9.3 Future Work

This research has led to several additional paths. Several are obvious continuations of the current research, such as the continued work on the numerical Navier Stokes solver to compare the remainder of the longitudinal and lateral models, and more general forward flight dynamics models.

Many dipterans are rarely found hovering (Ellington, 1984b), and previous work has already demonstrated forward flight does affect the aerodynamics (Dickson

and Dickinson, 2004). Changes in the dynamic properties of flapping wing flight as an insect transitions to forward flight may be analogous to the changes observed as rotorcraft transition to forward flight. Kinematics have recently been collected for *Drosophila* in untethered forward flight and *Asilidae* and *Tabanidae* are also under investigation.

Several ongoing MAV designs incorporate the controllability measures developed to reduce the actuation requirements, including an at-scale robotic flapping wing platform incorporating all the required degrees of freedom for controlled flight. Perhaps the most significant impact on MAV design is the finding that a biological form of rate feedback is appropriate for flight stabilization, which has not only guided the development of a haltere-based sensor for flight stabilization, but has suggested control readily manufactured using micro-electro-mechanical machines (MEMS) technology in tandem with at-scale robotic flight platforms. Work is underway to implement a biologically inspired controller for flapping wing flight stabilization on an integrated circuit, an accomplishment that will unlock a level of aerial mobility that was previously not yet possible on such minimal processing hardware.

Analytic work on the ocelli and compound eye sensitivity functions are underway and will allow researchers to perform an analysis to uncover the configurations which best encode flight modes and actuation results. Biologically relevant time delays and phase characteristics for each of the sensor models will be included in this formulation, allowing the frequency range fractionation observed in sensing to be represented. Once a comprehensive model for the combined compound eye/ocelli

system has been built, an accurate control-theoretic observability analysis may be conducted, including the effects of the differing frequency properties of the sensing modalities. The hypothesis that insects measure quantities that take advantage of the airframe dynamic properties can then be evaluated via determining the pointing directions that minimize measures of the stat estimate quality, such as the norm of the estimate covariance.

Bibliography

D. L. Altshuler, W. B. Dickson, J. T. Vance, S. P. Roberts, and M. H. Dickinson. Short-amplitude high-frequency wing strokes determine the aerodynamics of honeybee flight. *PNAS*, 102(50):18213–18218, 2005.

S. A. Ansari, R. Zbikowski, and K. Knowles. Aerodynamic modelling of insect-like flapping flight for micro air vehicles. *Progress In Aerospace Sciences*, 42:129–172, 2006.

S. A. Ansari, K. Knowles, and R. Zbikowski. Insectlike Flapping Wings in the Hover Part 1: Effect of Wing Kinematics. *AIAA Journal of Aircraft*, 45(6), 2008.

H. Autrum. Electrophysiological Analysis of the Visual Systems in Insects. *Experimental Cell Research*, 14 Suppl. 5:426–439, 1958.

S. Avadhanula, R. J. Wood, E. Steltz, J. Yan, and R. S. Fearing. Lift Force Improvements for the Micromechanical Flying Insect. In *IEEE/RSJ Intl. Conference on Intelligent Robots and Systems*, pages 1350–1356, 2003.

Aviation Engineering Directorate. Aeronautical Design Standard Performance Specification Handling Qualities Requirements for Rotorcraft. Technical Report ADS-33E, United States Army Aviation and Missile Command, March 2000.

C. N. Balint and M. H. Dickinson. Neuromuscular control of aerodynamic forces and moments in the blowfly, *Calliphora vicinae* . *Journal of Experimental Biology*, 207:3813–3838, 2004.

J. A. Bender and M. H. Dickinson. A comparison of visual and haltere-mediated feedback the control of body saccades in *Drosophila melanogaster*. *Journal of Experimental Biology*, 209:4597–4606, 2006a.

J. A. Bender and M. H. Dickinson. Visual stimulation of saccades in magnetically tethered *Drosophila*. *Journal of Experimental Biology*, 209:3170–3182, 2006b.

L. Bennett. Insect Flight: Lift and Rate of Change of Incidence. *Science*, 167(3915): 177–179, 1970.

G. J. Berman and Z. J. Wang. Energy-minimizing kinematics in hovering insect flight. *Journal of Fluid Mechanics*, 582:153–168, 2007.

H. Buelthoff, T. Poggio, and C. Wehrhahn. 3-D Analysis of the Flight Trajectories of Flies (Drosophila melanogaster). *Zeitschrift for Naturforschung*, C 35(1122): 811–815, 1980.

Bush, B. and Baeder, J. Force production mechanisms of a flapping mav wing. In *AHS International Conference on Aeromechanics*, San Fransisco, CA, January 23–25 2008.

Bush, B., MacFarlane, K., Baeder, J., and Humbert, J.S. Development of immersed boundary code with application to mav stability analysis. In *27th Army Science Conference*, Orlando, FL, November 29 – December 2 2010.

J. Casas and S. J. Simpson. *Insect Mechanics and Control*. Academic Press, 2007.

B. Cheng, S. N. Fry, Q. Huang, and X. Deng. Aerodynamic damping during rapid flight maneuvers in the fruit fly drosophila. *The Journal of Experimental Biology*, 213:602–612, 2010.

J. D. Cole. *Perturbation Methods in Applied Mathematics*. Blaisdell Publishing Company, Waltham MA, 1968.

M. J. Corless and A. E. Frazho. *Linear Systems and Control: An Operator Perspective*. Marcel Dekker, Inc. New York, NY, 2003.

W. D. Crill, R. B. Huey, and G. W. Gilchrist. Within- and between-generation effects of temperature on the morphology and physiology of *Drosophila melanogaster*. *Evolution*, 50(3):1205–1218, 1996.

G. Dalpiaz, A. Rivola, and R. Rubini. Effectiveness and sensitivity of vibration processing techniques for local fault detection in gears. *Mechanical Systems and Signal Processing*, 14(3):387 – 412, 2000. ISSN 0888-3270. doi: DOI:10.1006/mssp.1999.1294.

X. Deng, L. Schenato, and S. S. Sastry. Flapping Flight for Biomimetic Robotic Insects: Part I-System Modeling. *Transactions on Robotics*, 22(4):789–803, 2006a.

X. Deng, L. Schenato, W. C. Wu, and S. S. Sastry. Flapping Flight for Biomimetic Robotic Insects: Part I-System Modeling. *Transactions on Robotics*, 22(4):776–788, 2006b.

W. Derham. Physico-theology. *Journal of Experimental Biology*, 1714.

M. H. Dickinson. Unsteady mechanisms of force generation in aquatic and aerial locomotion. *American Zoologist*, 36:537–554, 1996.

M. H. Dickinson and K. Gotz. Unsteady Aerodynamic Performance of Model Wings at Low Reynolds Numbers. *Journal of Experimental Biology*, 174:45–64, 1999.

M. H. Dickinson, F. O. Lehmann, and S. P. Sane. Wing Rotation and the Aerodynamic Basis of Insect Flight. *Science*, 284(1954), 1999.

W. Dickson, A. Straw, and M. H. Dickinson. Integrative Model of Drosophila Flight. *AIAA Journal*, 46(9), 2008.

W. B. Dickson and M. H. Dickinson. The effect of advance ratio on the aerodynamics of revolving wings. *Journal of Experimental Biology*, 207:4269–4281, 2004.

W. B. Dickson, P. Polidoro, M. M. Tanner, and M. H. Dickinson. A linear systems analysis of the yaw dynamics of a dynamically scaled insect model. *Journal of Experimental Biology*, 213(17):3047–3061, 2010. doi: 10.1242/jeb.042978.

D. B. Doman, M. W. Oppenheimer, and D. O. Sigthorsson. Wingbeat Shape Modulation for Flapping-Wing Micro-Air-Vehicle Control During Hover. *Journal of Guidance, Control, and Dynamics*, 33(3):724–739, 2010a.

D. B. Doman, M. W. Oppenheimer, and D. O. Sigthorsson. Dynamics and Control of a Biomimetic Vehicle Using Biased Wingbeat Forcing Functions: Part II - Controller. In *Proceedings of the 48th AIAA Aerospace Sciences Meeting Including the New Horizons Forum and Aerospace Exposition*, Jan 2010b. AIAA.

R. Dudley. Extraordinary Flight Performance of Orchid Bees (Apidae euglossoni) Hovering in Heliox . *Journal of Experimental Biology*, 198:1065–1070, 1995.

G. E. Dullerud and F. Paganini. *A Course in Robust Control Theory*. Springer, New York, NY, 2000.

C. P. Ellington. The Aerodynamics of Hovering Insect Flight IV: Aerodynamic Mechanisms. *Philosophical Transactions of the Royal Society of London. Series B, Biological Sciences (1934-1990)*, 305(1122):79–113, 1984a.

C. P. Ellington. The Aerodynamics of Hovering Insect Flight III: Kinematics. *Philosophical Transactions of the Royal Society of London. Series B, Biological Sciences (1934-1990)*, 305(1122), 1984b.

C. P. Ellington. The Aerodynamics of Hovering Insect Flight II: Morphological Parameters. *Philosophical Transactions of the Royal Society of London. Series B, Biological Sciences (1934-1990)*, 305(1122), 1984c.

R. A. Ennos. The Kinematics and Aerodynamics of the Free Flight of some Diptera. *Journal of Experimental Biology*, 142(1):49–85, 1989.

I. A. Faruque and J. S. Humbert. Dipteran Insect Flight Dynamics Part 1: Longitudinal Motion about Hover. *Journal of Theoretical Biology*, 264(2):538–552, 2010.

E. I. Fontaine, F. Zabala, M. H. Dickinson, and J. W. Burdick. Wing and body motion during flight initiation in Drosophila revealed by automated visual tracking. *Journal of Experimental Biology*, 212:1307–1323, 2009. doi: 10.1242/jeb.025379.

G. Fraenkel. The function of the halteres of flies (Diptera). In *Proceedings of the Zoological Society of London*, volume 109, pages 69–78, 1939.

J. A. Franklin. *Dynamics, control, and flying qualities of VSTOL aircraft*. American Institute of Aeronautics and Astronautics, 2002. Reston, VA.

S. Fry, R. Sayaman, and M. H. Dickinson. The Aerodynamics of Free-Flight Maneuvers in Drosophila. *Science*, 300(495), 2003.

R. J. Full and M. A. R. Koehl. Drag and Lift on Running Insects. *Journal of Expermental Biology*, 176:89–101, 1992.

R. H. G Nalbach. The halteres of the blowfly Calliphora I: Kinematics and dynamics. *Journal of Comparative Physiology*, 173:293–300, 1993.

N. Gao, H. Aono, and H. Liu. A Numerical Analysis of Dynamic Flight Stability of Hawkmoth Hovering. *Journal of Biomechanical Science and Engineering*, 4(1): 105–116, 2009.

K. G. Gotz. Course-Control, Metabolism and Wing Interference During Ultralong Tethered Flight in *Drosophila melanogaster*. *Journal of Experimental Biology*, 128:35–46, 1987.

T. L. Hedrick, B. Cheng, and X. Deng. Wingbeat Time and the Scaling of Passive Rotational Damping in Flapping Flight. *Science*, 324:252–255, 2009.

R. K. Heffley, W. F. Jewell, J. M. Lehman, and R. A. Van Winkle. A Compilation and Analysis of Helicopter Handling Qualities Data Volume One: Data Compilation. Technical Report CR-3144, volume 1, National Aeronautics and Space Administration, August 1979a.

R. K. Heffley, W. F. Jewell, J. M. Lehman, and R. A. Van Winkle. A Compilation and Analysis of Helicopter Handling Qualities Data Volume Two: Data Analysis. Technical Report CR-3144, volume 2, National Aeronautics and Space Administration, August 1979b.

T. Hesselberg and F. O. Lehmann. Corrigendum: Animal Flight Dynamics II. Longitudinal Stability in Flapping flight. *Journal of Experimental Biology*, 210: 4139–4334, 2007.

J. S. Humbert and A. M. Hyslop. Bio-Inspired Visuomotor Convergence. *Transactions on Robotics*, 26:121–130, 2010.

W. Johnson. *Helicopter Theory*. Dover Publications, 1994.

R. Jones and D. Cohen. Aerodynamics of Wings at High Speeds. In A. Donovan and H. Lawrence, editors, *High Speed Aerodynamics and Jet Propulsion*, volume 7, pages 36–48, 1957.

D. Karan, J. P. Morin, B. Moreteau, and J. R. David. Body size and developmental temperature in *Drosophila melanogaster*: analysis of body weight reaction norm. *Journal of Thermal Biology*, 23(5):301–309, 1998.

J. Kevorkian. The Two Variable Expansion Procedure for the Approximate Solution of Certain Nonlinear Differential Equations. In J. B. Rosser, editor, *Lectures in Applied Mathematics, Volume VII*, volume 7, pages 206–275, 1966.

J. G. Leishman. *Principles of Helicopter Aerodynamics*. Cambridge University Press, 2006.

G. Nalbach. The halteres of the blowfly Calliphora II. Three-dimensional organization of compensatory reactions to real and simulated rotations. *Journal of Comparitive Physiology*, 175:695–708, 1994.

R. C. Nelson. *Flight Stability and Automatic Control*. McGraw Hill, Inc, 1989.

K. Ogata. *Modern control engineering*. Prentice Hall, 2002. Upper Saddle River, NJ.

M. W. Oppenheimer, D. B. Doman, and D. O. Sigthorsson. Dynamics and Control of a Biomimetic Vehicle Using Biased Wingbeat Forcing Functions: Part I - Aerodynamic Model. In *Proceedings of the 48th AIAA Aerospace Sciences Meeting Including the New Horizons Forum and Aerospace Exposition*, Jan 2010. AIAA.

M. F. M. Osborne. Aerodynamics of Flapping Flight with Application to Insects. *Journal of Experimental Biology*, 28:221–245, 1951.

M. M. Parsons, H. G. Krapp, and S. B. Laughlin. Sensor fusion in identified visual neurons. *Current Biology*, (20):1–5, 2010.

R. Ramamurti and W. C. Sandberg. A three-dimensional computational study of the aerodynamic mechanisms of insect flight. *Journal of Experimental Biology*, 205:1507–1518, 2002.

R. Ramamurti and W. C. Sandberg. Computational Investigation of the three-dimensional unsteady aerodynamics of Drosophila hovering and maneuvering. *Journal of Experimental Biology*, 201:881–896, 2007.

L. Ristroph, G. J. Berman, A. J. Bergou, Z. J. Wang, and I. Cohen. Automated hull reconstruction motion tracking (HRMT) applied to sideways maneuvers of free-flying insects. *Journal of Experimental Biology*, 212(9):1324–1335, 2009. doi: 10.1242/jeb.025502.

L. Ristroph, A. J. Bergou, G. Ristroph, K. Coumes, G. J. Berman, J. Guckenheimer, Z. J. Wang, , and I. Cohen. Discovering the flight autostabilizer of fruit flies by inducing aerial stumbles. *PNAS*, 107:4820–4824, 2010.

C. H. Rowell and K. G. Pearson. Ocellar Input to the Flight Motor System of the Locust: Structure and Function. *Journal of Experimental Biology*, 103:265–288, 1983.

S. P. Sane. The aerodynamics of insect flight. *Journal of Experimental Biology*, 206: 4191–4208, 2003.

S. P. Sane and M. H. Dickinson. The aerodynamic effects of wing rotation and a revised quasi-steady model of flapping flight. *Journal of Experimental Biology*, 205:1087–1096, 2002.

L. Schenato. *Analysis and Control of Flapping Flight: From Biological to Robotic Insects*. PhD thesis, EECS Department, University of California, Berkeley, 2004.

A. Sherman and M. H. Dickinson. A comparison of visual and haltere-mediated equilibrium reflexes in the fruit fly *Drosophila melanogaster*. *Journal of Experimental Biology*, 206:295–302, 2003.

A. Sherman and M. H. Dickinson. Summation of visual and mechanosensory feedback in *Drosophila* flight control. *Journal of Experimental Biology*, 207:133–142, 2004.

Shyy, W., Lian, Y., Tang, J., Viieru, D., and Liu, H. *Aerodynamics of Low Reynolds Number Flyers*. Cambridge University Press, New York, 2008.

G. R. Spedding and T. Maxworthy. The generation of circulation and lift in a rigid two-dimensional fling. *Journal of Fluid Mechanics*, 165:247–272, 1986.

M. Sun and Y. Xiong. Dynamic Flight Stability of a hovering bumblebee. *Journal of Experimental Biology*, 208:447–459, 2005.

M. Sun, J. Wang, and Y. Xiong. Dynamic flight stability of hovering insects. *Acta Mech Sin*, 2010(26):175–190, 2010.

G. K. Taylor. Mechanics and aerodynamics of insect flight control. *Biological Review*, 76:449–471, 2001.

G. K. Taylor and H. G. Krapp. Sensory systems and flight stability: what do insects measure and why? *Advanced Insect Physiology*, (34):231–316, 2007.

G. K. Taylor and A. L. R. Thomas. Animal Flight Dynamics II. Longitudinal Stability in Flapping flight. *Journal of Experimental Biology*, 214:351–370, 2003a.

G. K. Taylor and A. L. R. Thomas. Corrigendum: Animal Flight Dynamics II. Longitudinal Stability in Flapping flight. *Journal of Experimental Biology*, 221: 671, 2003b.

G. K. Taylor and A. L. R. Thomas. Dynamic flight stability in the desert locust Schistocerca gregaria. *Journal of Experimental Biology*, 206:2803–2829, 2003c.

R. A. Thompson, M. F. Wehling, and J. Evers. Evaluation of the haltere as a biologically inspired inertial rate measurement sensor. In *Guidance, Navigation, and Control Conference*, 2008.

M. B. Tischler. Frequency-Response Method for Rotorcraft System Identification: Flight Applications to BO-105 Coupled Rotor/Fuselage Dynamics. *Journal of the American Helicopter Society*, 37:19–44, 1992.

M. B. Tischler and M. G. Cauffman. Comprehensive Identification from FrEquency Responses, Vol 3. Technical Report TR-94-A-018, US Army Aviation and Troop Command, September 1999.

M. B. Tischler and R. K. Remple. *Aircraft And Rotorcraft System Identification: Engineering Methods With Flight-test Examples*. American Institute of Aeronautics and Astronautics, 2006. Reston, VA.

J. T. Vance and J. S. Humbert. Mechanisms of gust rejection in the honey bee, Apis mellifera. Technical Report 55.6, Society for Integrative and Comparative Biology, Jan 5 2010.

J. T. Vance, J. B. Williams, M. M. Elekonich, and S. P. Roberts. The effects of age and behavioral development on honey bee (Apis mellifera) flight performance. *The Journal of Experimental Biology*, 212:2604–2611, 2005.

J. T. Vance, I. A. Faruque, and J. S. Humbert. The effects of differential wing stroke amplitude and stroke offset on insect body movements during perturbed flight conditions. In *34th Annual Meeting of the American Society of Biomechanics*, Providence, RI, August 18-August 21 2010.

S. Vogel. Flight in Drosophila: II. Variations in Stroke Parameters and Wing Contour. *Journal of Experimental Biology*, 46:383–392, 1967.

T. Weis-Fogh. Energetics of Hovering Flight in Hummingbirds and in Drosophila. *Journal of Experimental Biology*, 56:79–104, 1972.

C. H. Wolowicz, J. S. Bowman, Jr, and W. P. Gilbert. Similitude Requirements and Scaling Relationships as Applied to Model Testing. Technical Report TR-1435, National Aeronautics and Space Administration, August 1979.

R. J. Wood. The First Takeoff of a Biologically Inspired At-Scale Robotic Insect. *Transactions on Robotics*, 24(2), 2008.

J. M. Zanker. The wing beat of drosophila melanogaster. i. kinematics. *Philosophical Transactions of the Royal Society of London. Series B, Biological Sciences*, 327 (1238):pp. 1–18, 1990. ISSN 00804622.

J. M. Zanker and K. G. Gotz. The wing beat of *Drosophila melanogaster* II: dynamics. *Phil Trans R Soc Lond*, 327:247–272, 1990.